

ELECTROCHEMICAL AND MORPHOLOGICAL CHARACTERIZATION OF
ELECTROLESS Ni-P COATINGS ON DIAMOND PARTICLES

A Dissertation

by

LIAN MA

Submitted to the Office of Graduate and Professional Studies of
Texas A&M University
in partial fulfillment of the requirements for the degree of

DOCTOR OF PHILOSOPHY

Chair of Committee,	Hong Liang
Co-Chair of Committee,	Gwo-Ping Fang
Committee Members,	Ying Li
	Li-Jung Tai
Head of Department,	Andreas A. Polycarpou

August 2020

Major Subject: Mechanical Engineering

Copyright 2020 Lian Ma

ABSTRACT

The electroless deposition has been adopted as a simple and cost-effective method to synthesize Ni-P coatings on various substrates for corrosion and wear protection. Such coatings on diamond abrasives have been used to manufacture diamond tools. Those coatings, however, if not synthesized properly, are easy to be fractured and detached from the substrate during the deposition and manufacturing processes. This research investigates the corrosion resistance, deposition kinetics, and coating failure mechanisms of Ni-P coatings electrolessly deposited on diamond particles. The major activities are summarized in the following.

One of the challenges in this research is the lack of characterization methods for coatings on such small particles with irregular shapes. To overcome this, a novel electrode was developed so that the electrochemical characterization was successfully conducted on Ni-P coated particles. The micro-CT technique was used to characterize the coating on small irregular-shaped particles to get comprehensive morphological information.

Through electrochemical characterizations, an improved electrolyte with less corrosion power to the Ni-P coating was developed for the diamond tool manufacturing process. The crucial microstructure which causes coating failure is found to be the micropores generated in the coating due to hydrogen gas evolved during the deposition process. The coating failure was found to be caused by the corrosion assisted breakthrough of close pores in the coating.

Various morphological characterizations techniques demonstrate that the coating coverage rate on diamond particles is affected by the synergistic action of the deposition time, substrate morphology, and reducing agent concentration. The two major morphological features of the coating: nodular and smooth are influenced by the deposition parameters, coating integrity, and substrate morphology.

The deposition kinetics of coatings were studied through analyzing coating thickness as a function of plating time in the plating solutions of varied reducing agent concentrations. The dependence of deposition rate on reducing agent concentration and nickel ion concentration was found at different stages of the deposition process. The change of the dependence relationship was found to be affected by the free nickel ion concentration.

Morphological characterization revealed that the failure was due to tensile residual stress produced by the coalescing of crystallites during the deposition. This failure mechanism explains the tendency of coating fracture at three morphological features of the substrate.

This research is the first comprehensive study of the coating failure mechanisms on diamond particles. The new methodologies developed in this study will be beneficial for the investigation of other coatings on the particle systems.

DEDICATION

To all the medical and nursing personnel who are fighting against COVID-19 and saving peoples' lives during the time I am writing this dissertation.

ACKNOWLEDGMENTS

Towards to end of my Ph.D. life, I would like to thank many people, without whom my life will be very different.

I would like to thank my committee chair, Dr. Liang, my co-advisor Dr. Fang, and my committee members, Dr. Li, Dr. Tai, for their guidance and support throughout this research.

Many thanks to Dr. Liang for the opportunity to explore the world of material science and engineering. Since I joined Dr. Liang's group, I have learned so much about material science, surface science, tribology, and electrochemistry. Each discussion with Dr. Liang and other group members has brought me new terminology and freshness in the scientific world. Dr. Liang is a good advisor, who helps the students master the skills needed both in academia and in industry. Dr. Liang's emphasis on critical thinking reminds me to always keep an eye on the scientific nature of the research.

I would also like to thank Dr. Fang for providing my financial support as a teaching assistant and offered training opportunities for the material characterization facilities.

Lots of thanks for the assistance, discussion, and collaborations go to my labmates in the surface science research group, Dr. Hyunho Chio, Dr. Subrata Kundu, Dr. Wenhui Xu, and Yan Chen.

Great appreciation goes to my mentor Dr. Xihua He in Southwest Research Institute, who guide me in the electrochemical tests and my mentor for teaching Dr.

Shadi Balawi, who helps me improve my teaching skills constantly. I would also like to thank my students in the MEEN 360 and MEEN 361 classes, in which I had wonderful teaching and learning experience.

I deeply appreciate the department staff, especially Ms. Sandy Havens and Ms. Rebecca Simon, for their assistance in the Department of Mechanical Engineering at Texas A&M University.

Many thanks to my friends and roommates for all the holiday gatherings, for the company and comforting words when I had a hard time.

Finally, and most importantly, endless thank you to my parents for their encouragement, understanding love, and sacrifices.

CONTRIBUTORS AND FUNDING SOURCES

Contributors

This work was supervised by a dissertation committee consisting of Professor Hong Liang [advisor] and Professor Ying Li, and professor Bruce Tai of the Department of Mechanical Engineering and Professor Gwo-Ping Fang [co-advisor] of the Department of Engineering Technology and Industrial Distribution.

The X-ray tomography scanning was conducted by Yan Chen of the Department of Material Science and Engineering and Peter Renner of the Department of Mechanical Engineering. The AFM image of the catalytical clusters is taken with the help of Yan Chen.

All other work conducted for the dissertation was completed by the student independently.

Funding Sources

Graduate study was supported by teaching assistantships and graduate teaching fellowship from Texas A&M University, and a research assistantship provided by the research collaboration network program from NSF Foundation Expenses to conference was supported by a travel award from the department of mechanical engineering and organization of graduate and professional studies (OGAPS). Partial support from TAMU Turbomachine Research Consortium was appreciated.

NOMENCLATURE

Acronyms

AFM	Atomic force microscopy
CE	Counter electrode
CT	Computed tomography
CTE	Coefficient of thermal expansion
CVD	Chemical vapor deposition
EDS	Energy dispersive spectrum
EW	Equivalent weight
LPR	Linear polarization resistance
OCP	Open circuit potential
OER	Oxygen evolution reaction
PVD	Physical vapor deposition
RE	Reference electrode
SEM	Scanning electron microscopy
WE	Working electrode
XRD	X-ray diffraction

Symbols

M	Metal
η	Overpotential
α	Coefficient of thermal expansion
β	Tafel constant
ε	Strain
σ	Stress
ν	Poisson's ratio
κ	Curvature
ρ	Density
Ω	Cracking number
Γ	Toughness
a	Lattice parameter; Chemical activity
d	Height of the arc in a curved film
L	Length of a strip
E	Elastic modulus; Electrode potential
h	Film thickness
i	Current density
F	Faraday constant
R_p	Linear polarization resistance

R	Universal gas constant
r	Radius of a curvature
T	Temperature
z	Number of electrons transferred in the half-reaction, Position of the film in the thickness direction
ΔG	Gibbs free energy change

TABLE OF CONTENTS

	Page
ABSTRACT	ii
DEDICATION	iv
ACKNOWLEDGMENTS.....	v
CONTRIBUTORS AND FUNDING SOURCES.....	vii
NOMENCLATURE.....	viii
TABLE OF CONTENTS	xi
LIST OF FIGURES.....	xiv
LIST OF TABLES	xvii
CHAPTER I INTRODUCTION AND LITERATURE REVIEW	1
1.1 Comparison of selected metallic coating techniques	1
1.2 Vapor deposition	4
1.2.1 Deposition principle	4
1.2.2 Microstructure control.....	5
1.3 Electrodeposition.....	6
1.3.1 Deposition principle	6
1.3.2 Microstructure control.....	8
1.3.3 Similar wet deposition process.....	16
1.4 Electroless deposition.....	16
1.4.1 Discovery of the electroless deposition.....	17
1.4.2 Deposition principle and microstructure	17
1.4.3 Factors influencing the deposition process	21
1.4.4 Applications	27
1.5 Internal stress in electroless Ni-P coatings.....	32
1.5.1 Forms of coating failures.....	33
1.5.2 Origin of internal stress	34
1.5.3 Methods to measure internal stress	40
1.5.4 Factors influencing internal stress.....	42
1.6 Summary	43

CHAPTER II MOTIVATION AND OBJECTIVES	44
2.1 Motivation of this research.....	44
2.2 Objectives.....	46
2.3 Research approach.....	47
2.4 Dissertation structure.....	48
CHAPTER III MATERIALS AND METHODS	49
3.1 Electroless plating setup and process	49
3.1.1 Electroless plating process for electrochemical characterization.....	49
3.1.2 Electroless plating process for tomography characterization.....	51
3.1.3 Nomenclature of samples	53
3.2 Chemical composition and surface morphology characterization	53
3.3 Tomography of coatings on diamond particles	54
3.3.1 X-ray tomography	54
3.3.2 Samples fixture for X-ray tomography	55
3.3.3 X-ray tomography image processing	56
3.4 Electrochemical characterization of coatings on diamond particles	57
3.4.1 Preparation of Ni-P coated abrasive electrodes.....	57
3.4.2 Corrosion potential, corrosion rate.....	58
3.4.3 Durability test.....	60
3.4.4 Electrochemical test data processing.....	61
CHAPTER IV CORROSION RESISTANCE OF ELECTROLESS Ni-P COATING ON DIAMOND PARTICLES	63
4.1 Morphology and composition of the coating	63
4.2 Corrosion resistance of the coatings.....	66
4.3 Durability of coatings in an electroplating environment.....	73
4.4 Chapter summary of findings.....	77
CHAPTER V INFLUENCE OF PROCESSING PARAMETERS ON ELECTROLESS Ni-P COATINGS ON DIAMOND PARTICLES	79
5.1 Coating coverage rate.....	79
5.1.1 Factors influencing coating coverage rate.....	82
5.1.2 Process optimization	87
5.2 Coating morphology.....	88
5.2.1 Factors influencing coating morphology.....	89
5.2.2 Process suggestions	97
5.3 Deposition kinetics	97
5.3.1 Influence of crystallographic orientation	97
5.3.2 Influence of reactants concentration	101
5.4 Chapter summary of findings.....	109

CHAPTER VI FAILURE MECHANISMS OF ELECTROLESS Ni-P ON DIAMOND PARTICLES	111
6.1 Observation of coating failure	111
6.2 Physical model for coating failure	114
6.2.1 Origins of intrinsic stresses	114
6.2.2 Estimation of the intrinsic stress	116
6.2.3 Coating failure mechanism.....	119
6.3 Coating failure modes	121
6.4 Chapter summary of findings.....	124
 CHAPTER VII CONCLUSIONS AND FUTURE RECOMMENDATIONS	 125
7.1 Conclusions	125
7.2 Future recommendations	127
7.2.1 Plating bath modification	127
7.2.2 Optimization of electrochemical performance.....	127
7.2.3 Mechanical properties modeling	128
 REFERENCES	 129
 APPENDIX	 149

LIST OF FIGURES

	Page
Figure I.1. Mechanism of non-uniform deposition. Adapted from reference [47]	12
Figure I.2. Schematic of the electroless plating process: ① Diffusion to active sites, ② Adsorption ③ Reaction, ④ Desorption, ⑤ Diffusion away from the surface.	18
Figure I.3. Microstructure features which cause intrinsic stress in the electroless Ni-P coatings.....	19
Figure I.4. Schematic showing a mechanism of electroless film formation. Adapted from reference [47].....	21
Figure I.5. Complexing of a nickel ion with (a) six water molecules and (b) citric acid. Adapted from reference [69].	23
Figure I.6. The molecular formulas of four commonly used reducing agents for electroless plating (a) sodium hypophosphite, (b) sodium borohydride, (c) dimethylamine borane (DMAB), (d) hydrazine (e) formaldehyde.	24
Figure I.7. The manufacturing process of electroplated diamond wire saw.	31
Figure I.8. The difference in lattice constants leads to misfit stress in the film. Adapted from refernce [136].	37
Figure I.9. The sketch illustrates the tensile stress developed due to crystallites coalescence. Adapted from refernce [137].	38
Figure I.10. Strip deflection caused by the stress in the deposited film. Adapted from refernce [141].	41
Figure II.1. Research flow chart.	47
Figure III.1. Pretreatment process of diamond abrasives for electroless plating.	50
Figure III.2. Electroless plating setup.	51
Figure III.3. The configuration to examine the morphology of Ni-P coatings deposited on diamond abrasives.	55
Figure III.4. Preparation of sample holder for coated diamond abrasives.	56

Figure III.5. (a) (b) Schematics and (c) (d) pictures of electrode preparation.	57
Figure III.6. Schematic of the three-electrode cell.....	59
Figure IV.1. SEM image and EDS of (a) as-plated diamond grits and (b) coated diamond grits after immersion test.....	64
Figure IV.2. XRD patterns of as-plated coatings on diamond grits.....	66
Figure IV.3. Polarization curves of Ni-P on the diamond in low and high concentration electroplating solutions.....	67
Figure IV.4. SEM image of Ni-P coating on diamond (a) as plated, after polarization examination in (b) low concentration electrolyte (c) high concentration electrolyte.....	70
Figure IV.5. SEM image of Ni-P coating on the diamond after polarization examination in low concentration electroplating solutions from a ruptured coating location.	72
Figure IV.6. The current-assisted breakthrough of covered pinholes.....	72
Figure IV.7. Open circuit potentials monitoring.....	74
Figure IV.8. Corrosion rates monitoring.....	76
Figure V.1. Optical images of coatings on diamond particles.....	81
Figure V.2. AFM (a) height image and (b) 3D image of palladium clusters on the diamond surface.....	85
Figure V.3. Catalyst cluster size distribution on shallower and higher substrate surfaces. The blue boxes are drawn in Figure V.2 (a) to demonstrate the shallower substrate surface.....	86
Figure V.4. Volume rendered images of coated diamond particles showing nodules on the surface.....	91
Figure V.5. The SEM images of (a) a coated diamond showing the nodules at different locations. (b) high magnification image of the red box area in (a).	92
Figure V.6. Sketches illustrate the formation process of coating with (a) uniformly and densely distributed nucleation sites, (b) uniformly but loosely distributed nucleation sites.....	93
Figure V.7. Labels of different faces and edges of the Ni:P=1:2-10min diamond grit....	99

Figure V.8. Coating thickness distribution on different diamond faces.....	100
Figure V.9. Coating thickness on different faces and edges of the Ni:P=1:2-10min diamond grit.	101
Figure V.10. Coating thickness with different deposition time and reducing agent concentrations. The position of time is shifted a little to show the error bar.....	102
Figure V.11. Deposition rate change with different deposition time and reducing agent concentrations.....	103
Figure V.12. The concentration of nickel species in the plating bath.	104
Figure V.13. Relationship of deposition rate with nickel species concentration.	106
Figure V.14. Relation of free nickel ion concentration with total nickel species concentration in the plating solution.	109
Figure VI.1 Optical images showing the coating failure locations: green color indicate corners, red indicates flat surface, and blue indicates rough surfaces.....	112
Figure VI.2 Substrate morphologies with different coating failure tendencies. (a) the coating on the corner promotes failure, (b) the coating on flat surface promotes failure, (c) the coating on rough surface inhibits failure.	113
Figure VI.3. Average stress between two coalesced hemispheric crystallites and the number of coalescences to cause coating failure.....	118
Figure VI.4. Ni-P crystallites coalescence on different morphologies of the substrate.	120
Figure VI.5. (a) The optical image, (b) 3D view of the volume-rendered image, and (c) tomography of Ni:P=1:2-10 min sample shows the brittle fracture.	122
Figure VI.6. (a) The optical image, (b) 3D view of the volume-rendered image, and (c) tomography of Ni:P=1:2-20 min sample shows the ductile fracture.	123

LIST OF TABLES

	Page
Table I-1. Comparison of several common coating techniques.	3
Table II-1. Research areas on electroless Ni-P coatings	46
Table III-1 Pretreatment details.....	50
Table III-2 Electroless plating solution components and concentration	51
Table III-3 The Electroless plating bath components and concentrations	52
Table III-4 The pH values of the plating solution before and after adjusting	53
Table III-5 Composition and pH value of the electrolyte	60
Table IV-1 Parameters obtained from the Tafel plot	68
Table V-1 Equilibrium constants of the nickel ion determining reversible reactions....	107

CHAPTER I

INTRODUCTION AND LITERATURE REVIEW¹

This research investigates the electroless deposition process to synthesize coatings on diamond particles. The precise control of the electroless deposition process and the characterization of such coatings on the tiny particle system has been a challenging issue. The microstructure and properties of the coatings directly related to the processing methods. In this chapter, coating techniques that can provide coatings of similar applications are introduced, and the processing-microstructure relationships are reviewed to provide the bases for further investigations. The emphasis is put on the mechanisms of different factors in influencing microstructures.

1.1 Comparison of selected metallic coating techniques

Metallic coatings on various substrates have lots of functions. They can protect the substrates from oxidation, corrosion, wear, and electromagnetic radiation. The coatings can improve the thermal and electrical conductivity, solderability, and magnetic properties of the underlining layers. Moreover, coatings can produce some special chemical functions, reduce friction, render an aesthetic appearance.

Various techniques can be used to apply a metallic coating on a substrate. The coating techniques can be divided into various categories depending on classification

¹Part of this chapter is reprinted with permission from “Electrochemical Characterization of a Nickel-Phosphorus Coating on Diamond Grits” by Lian Ma, Xihua He, Alex Fang, and Hong Liang, *Materials Performance and Characterization* **2018**, 7(3), 266-280, Copyright [2018] by ASTM International.

criteria, such as the function of coatings and the medium in which the coating is deposited. In this context, later criterium is used, and two distinct categories are identified: wet and dry coating techniques. The dry coating techniques include vapor deposition, thermal spay, and weld overlay, which are carried out in a low-pressure vapor, air, or inert gas environment. On the other hand, wet coating techniques include electrodeposition and electroless deposition, which are performed in a solution¹.

Several widely used wet and dry techniques are described, and different aspects of these techniques are compared, the purpose of which is to identify the situations in which electroless plating technique is favorable. This review also provides more information on the processing-microstructure-properties relationship. Table I-1 lists the commonly used materials, application, advantages, and disadvantages of coating synthesized with vapor deposition, electroplating, and electroless plating methods.

Table I-1. Comparison of several common coating techniques.

Coating techniques	Vapor deposition	Electroplating	Electroless plating
Coating materials	Metals, ceramics, polymers, and composites	Metals and alloys	Metals and alloys
Applications	Semiconductor industry Synthesis for catalysts Protective coatings	Protective coatings Decorative coatings Magnetic coatings Metal extraction	Protective coatings Decorative coatings Metallization Magnetic coatings
Advantages	Atomic control Accurate composition and microstructure control	Fast speed	Uniform thickness Simple setup
Disadvantages	Slow speed High cost	Irregular morphology Complex bath Composition	Slow speed Solution aging
Ref.	2-7	8-20	21-37

1.2 Vapor deposition

1.2.1 Deposition principle

Vapor deposition describes a process in which coating material is generated in vapor and deposited onto the surface of a solid substrate. The difference between physical vapor deposition (PVD) and chemical vapor deposition (CVD) is whether a chemical reaction is involved in producing the deposited material. The state of stress in a film can be strongly influenced by its deposition history.

For physical vapor deposition, evaporation and sputtering are the most widely used methods to generate the vapors of the coating material⁷. The evaporation methods, as the name indicate, sublime or evaporate the material to be deposited from a solid or molten liquid by heating. Commonly used heating methods include resistant heating, high-frequency induction heating, electron beam evaporation. The evaporated atoms travel through the low-pressure chamber and condense on the substrate. For sputtering, ionized sputtering gas or plasma, usually argon ions created by collisions with high energy electrons, are accelerated toward the target by an electric or magnetic field. When the argon ions hit the target, the momentum transfer causes the atoms from the target to be dislodged with a high velocity. These atoms will travel through the discharge zone and condense onto the substrate in the deposition chamber. Different sputtering methods that are widely used include direct current (dc) sputtering, radio frequency (rf) sputtering, magnetron sputtering, and bias sputtering^{38, 39}.

Compared to evaporation methods, sputtering needs to have a higher pressure in the deposition chamber to generate self-sustaining plasma, and therefore, the sputter-

deposited coatings consist of contaminations from sputtering gas. Besides, since the sputtered atoms arrive at the substrate with high kinetic energy, it creates more defects in the deposited film. Also, sputtering results in a film with smaller grain size, better thickness uniformity, has better control of film stoichiometry. Furthermore, it has the flexibility to deposited essentially any crystalline or amorphous materials⁷.

Chemical vapor deposition is the process in which a volatile precursor decomposes or reacted with other gases on the substrate to produce a non-volatile solid that atomically deposited on a suitably placed substrate⁴⁰. It can be used to grow thin films of elemental and compound semiconductors, metal alloys, and amorphous or crystalline compounds of different stoichiometry. Different types of CVD are seen and classified by operation conditions, types of substrate heating, characteristics of vapor, etc. The commonly seen variants include atmospheric pressure CVD (APCVD), Low-pressure CVD (LPCVD), plasma-enhanced CVD (PECVD), laser-enhanced CVD (LECVD), Atomic layer CVD (ALCVD), and metal-organic CVD (MOCVD) which are used to achieve particular objectives^{7, 40, 41}.

1.2.2 Microstructure control

The microstructures of vapor-deposited films range from single crystalline, polycrystalline, to amorphous films. The principles of thermodynamics determine whether the deposition process can happen and a and kinetics determine the final film microstructure. The physical processes of film growth are discussed in depth by Tsao⁴², Pimpinelli and Villain⁴³, and Venables⁴⁴.

The first step of vapor deposition would be the attachment of the atoms from the vapor phase to the substrate surface and then followed by the film growth from the attached atoms which are called adatoms. When the temperature of the vapor is low enough, the vapor phase becomes supersaturated. Then the atoms in the vapor in contact with atoms in the substrate surface will form chemical bonds. The driving force of the process is the free energy difference, which depends on both vapor and substrate temperatures and the vapor pressure of the deposited material near the substrate.

The crystallinity of the film depends on the kinetics of the vapor deposition process. For depositing a single crystal film, atoms of the film material in the vapor must arrive at the substrate surface, adhere to it, and settle into possible equilibrium positions before structural defects occupy the position in the growth front. For an amorphous film, on the other hand, atoms must be prevented from seeking stable equilibrium positions when they arrive at the growth surface. In both CVD and PVD, vapor supersaturation affects the nucleation rate of the film, whereas substrate temperature influences the rate of film growth⁷. Low gas supersaturation and high substrate temperature promote the growth of single-crystal film on substrates. High gas supersaturation and low substrate temperatures result in the growth of less coherent and possibly amorphous films.

1.3 Electrodeposition

1.3.1 Deposition principle

Electroplating belongs to wet deposition techniques in which an aqueous solution is the involved⁸. In electroplating, a conductive substrate and an anode made of the plating material are immersed in a solution consists of the metal ion to be plated. When a

voltage larger than a critical value is applied between the substrate and the anode, the metal ions in the solution are reduced to the solid metal on the substrate surface. At the same time, the anode is oxidized and dissolves in the solution to make up the lost metal ions. The electroplating was discovered by Italian chemist and inventor Luigi Valentino Brugnatelli in 1805, making use of a voltaic pile invented by Alessandro Volta five years earlier⁴⁵. The voltaic pile can provide a stable current supply to the electroplating process.

Whether the metal deposition can occur and how fast the deposition depends on the applied voltage. When a substrate made from metal M is immersed in an aqueous solution containing ions of that metal M^{Z+} , there will be a reversible conversion of metal ions M^{Z+} and metal atoms M at the interface. At equilibrium condition, the rate of metal atoms leaving the electrode and the rate of ions attach to the electrode are the same. Since gaining and losing electrons require to overcome different energy barriers, the surface is always charged to facilitate electron transfer of the slower process to maintain the equilibrium. Because of the extra charge, there is a voltage difference between this immersed metal and a standard hydrogen electrode if they are both immersed in the electrolyte. This voltage difference is defined as the reversible potential at a standard condition. A standard hydrogen electrode is made of an inert electrode such as platinum or graphite immersed in the solution containing 1 mole of H^+ and with one atom H_2 gas bubbled to the solution. The standard condition is when the metal is immersed in a solution composed of 1 mole of the metal ion at 25 °C⁴⁶. If a potential more negative than the reversible potential is applied to the substrate, there will be extra electrons on it,

which will promote the reduction of the ions so that the deposition is possible. The lower the potential, the higher the deposition rate will be.

The potential of an electrode in an electrolyte also depends on the concentration of ions in the electrolyte and the temperature, which is described by the Nernst equation:

$$E = E^0 - \frac{RT}{zF} \ln \frac{a_{Red}}{a_{Ox}} \quad \text{I-1}$$

The rate of deposition can be quantified by the Tafel equation:

$$\eta = a + b \log |i| \quad \text{I-2}$$

Where i is the deposition current, η is the overpotential, a is a constant, and b is the Tafel slope⁴⁶.

1.3.2 Microstructure control

When evaluating the plated films for different applications, different aspects of microstructure are taken into considerations. When the coatings are used for corrosion and wear protection, the electrochemical or chemical properties and mechanical properties are important, so the microstructures such as phases distribution, grain size, grain orientations, porosity, residual stresses, etc. become more critical. When the coatings are used to provide metallic appearance, then the surface morphology such as roughness, waviness need to be characterized.

According to Watanabe⁴⁷, there are seven categories of microstructures in plated films. Each of these microstructures is created by different mechanisms and is affected by a combination of many factors such as substrate material, pre-treatment of the substrate, type of metals, solution concentration, type of metallic salts, types and amounts of complexing agents, solution pH, additives, current density, overpotential,

etc. ⁴⁸⁻⁵⁰. These variables are not fixed but change all the time during the plating process, which makes the control of the microstructure even harder.

The following part will discuss the key factors which influence those microstructures.

1.3.2.1 Metallurgical structure

In metallurgy, for a given composition of an alloy and temperature, the phase diagram tells whether a liquid phase, solid solutions, or an intermetallic compound is the stable phase. But in real processes, these stable phases may not form due to non-equilibrium cooling. Therefore, meta-stable phases, amorphous phases, and supersaturated solid solutions may form⁵¹.

The metallurgical structure influences the coatings' mechanical strength in the following ways. The films of smaller grain sizes are stronger within a grain size range due to the Hall-Petch strengthening mechanism. The single-phase solid solution and the multiphase alloys also can strengthen the film by solid solution strengthening and dispersion strengthening mechanisms^{10, 11, 52}. The meta-stable phase and amorphous phase may exhibit distinct properties compared to the equilibrium phases, such as hardness and chemical reactivity. The defect state also influences the chemical or electrochemical properties of the coating.

The metallurgical structure is mainly determined by the heating and cooling process associated with the electrodeposition. Considering a plating process with a plating current density of $1\text{A}/\text{dm}^2$, it means there will be around 3×10^{18} divalent metal cations reduced and become neutral atoms deposited onto the substrate with a size of 1

dm². Each discharge can release a large amount of energy and create a high-temperature adatom. Furthermore, joule heating at the interface adds more thermal energy to the substances nearby since there is a big electric field in the electrical double layer⁵³. Therefore, during the plating process, the discharges create lots of high-temperature adatoms that can migrate over the substrate surface. The heat generated subsequently dissipates to the surrounding solution as well as the electrode. Since the temperature of the solution is less than 100°C, and the solution is water-based, which has a large heat capacity, the cooling rate is relatively high. Just like the traditional solidification processes, fast cooling in the deposition doesn't provide the atoms enough time to move to equilibrium positions, as a consequence, the film tends to form a polycrystalline microstructure with small grain size or amorphous microstructure.

The heating temperature and cooling rates depend on the types of elements to be deposited, the composition of the film, deposition overpotential, plating solution temperature, and the solution agitation. If pure metal or two metals having unlimited mutual solubility are deposited, the single-phase crystal will be formed in the plated film⁵⁴. If the phase diagram of the metals to be plated indicated they could have eutectic, peritectic, or monotectic reactions, it is possible to form more than one phase in the plated films. If an alloy is deposited with the composition near that of an intermetallic compound, the formation of intermetallic compound crystals is possible if the crystallization energy is supplied and the diffusion of atoms is fast enough to reach equilibrium. Otherwise, either a meta-stable phase or amorphous phase will be

generated⁵⁵. The hydrogen-induced amorphization of intermetallic compounds is another mechanism to generate amorphous phases instead of crystalline phases⁵⁶⁻⁵⁸.

1.3.2.2 Surface morphology

The surface morphology is important to the appearance and surface area of the coating. According to Watanabe, the surface morphology changes with plating time, current density, types of anions, solution temperature, solution agitation. Other factors, such as the addition of brightener, will also influence surface morphology⁴⁷.Dr.

Watanabe claimed that the deposition at the beginning is flat and uniform, but due to different extent of discharges at different locations at the interface, there will be a non-uniform metal-ion depleted layer formed. And the thickness of this metal-ion depleted layer will further affect the diffusion distance of metal ions and hence the deposition rate. Therefore, the continued deposition preferentially takes place at peaks at the surface, shown in Figure I.1, which is adapted from Figure 1.13 in Watanabe's book: Nano Plating⁴⁷. At the valley locations, the metal ion cannot arrive, and the film growth at these locations is by the surface migration of the metal atoms from the peak position, which is determined by the diffusion distance of the surface diffusion. The peak and valley will be enhanced with deposition time creating high surface roughness.

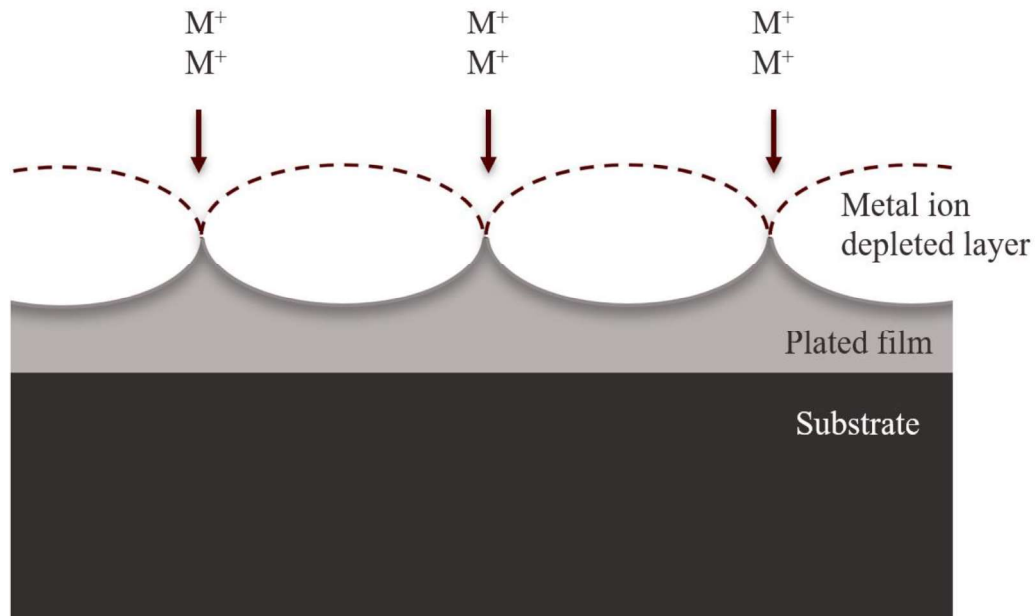


Figure I.1. Mechanism of non-uniform deposition. Adapted from reference [47].

The increase in current density will make the surface smoother. Because the density of the sites where the initial discharges occur will be higher with the increase of current density. In other words, the oval-shaped metal ion depletion layer will be smaller. The change will lead to easier diffusion of metal ions to the valley positions and the easier surface diffusion of metal atoms to the valley position.

The metal ion is provided by a metal salt dissolved in the solution, which also brings in anions to the solution. The type of anions also affects the surface roughness of the deposited film. For example, in the electrodeposition of nickel and cobalt, the surface is smoother with a sulfate solution than a chloride solution because the sulfate ions have a larger size and lead to the higher viscosity of the solution than the chloride solution, which makes the diffusion harder.

Temperature is an important factor that influences surface morphology. With increased temperature, the diffusion of ions in the solution is faster, giving rise to a fast growth rate, which has a similar effect as the deposition time. The surface diffusion of adatoms is also increased, but it is not as strong as the ion diffusion enhancement. In other words, the surface diffusion is not fast enough to smooth the roughness created by the enhanced deposition at the peaks at high temperatures.

Solution agitation provides a faster supply of metal ions and decreases the thickness of the metal ion depleted layer, and therefore, generates a rough surface. It was observed that solution agitation could develop secondary peaks at the side face of primary deposition pyramids⁴⁷.

The grain size is another important factor that influences the film's surface morphology. For the deposition of low melting temperature metal, the surface roughness is proportional to the grain size—the smaller the grains, the smoother the surface. It is easy to form fine-grained crystal or amorphous deposits by depositing alloys, so most alloy films are usually smooth and bright when the deposition current is high enough.

Brightener is some additives in the plating solution to improve the smoothness of the film. They mainly act in two mechanisms: organic brighteners adhere to the peaks or change the viscosity of the solution; inorganic brighteners provide small atoms co-deposited to the film and refine the grains by alloying.

1.3.2.3 Crystal grain size and shape

If a high melting temperature metal is deposited, during the cooling, the undercooling is large, and it is easy to form lots of nucleation sites and results in fine-

grained crystals. On the contrary, if a low melting temperature metal is deposited, the same cooling rate does not provide enough undercooling. Therefore, the nucleation sites are less, and the films contain large grains⁵⁹. The contaminations in the solution may also affect the grain size by introducing more nucleation sites. From experiments by Girin¹¹, the relation of grain size to melting temperature is also explained by the exchange current density.

If alloying elements such as B, C, P, and S are co-deposited, the grain size can also be refined.

1.3.2.4 Contact with the substrate

The electroplated films on a metal substrate generally grow by lattice matching to reduce the interfacial energy. With different crystal systems from the substrate and the deposit, the misfit dislocations and misfit twins can form¹³. And then, grain boundaries forms and the film continue to grow into columnar grains. This lattice matching the growth of the deposits can maintain up to a thickness when the stress accumulates to an extent.

1.3.2.5 Residual stress

Residual stress can develop when there are mismatches of lattice in the film or when the materials with different thermal expansion coefficient cool down quickly. The residual stress may cause the film to bend or crack, and therefore, it is important to the film integrity and mechanical properties of the film. The stress-free film can be produced by introducing stress-reducing additives in the plating bath.

The incorporation of impurities will lead to the distortion of the lattice structure, but usually, grain boundaries will form to mitigate this distortion, and therefore residual stress is not created. But when hydrogen atoms are incorporated in the film, residual stress can develop. Since hydrogen atoms are small, it can diffuse fast in the deposits to form hydrogen gases and diffuse out of the film. The out-diffusion of the hydrogen gas causes the film to shrink, and tensile stress will be exerted on the film by the substrate to maintain the interfacial connection. If the tensile stress is too big, the film may crack at the weakest point, usually at grain boundaries. Another typical failure mode is the peeling of the film from the substrate resulting in a curled-up film. During the electroplating of Ni-P film, the high P content is accompanied by a high hydrogen evolution (low current efficiency) and leaves high tensile residual stress in the film.

1.3.2.6 Unusual shape

Nodules are semi-spherical etching. It is inferred that for electroless plating, at these protrusions, the morphology formed on the surface of the deposited film. They are formed in both electrodeposition and electroless deposition, and the formation mechanism is complex. The nodules tend to form on fine protrusions on the surface of substrates, which may be caused because the flow rate of the plating solution is faster, and thus there is a faster deposition rate. But no solid proof has been provided.

Pits are small holes on the surface of the deposited film. They are formed due to two causes, contaminations and hydrogen formation. Contaminants blocked the surface from metal ions and shut down the plating at the sites. Hydrogen atoms formed in the film can diffuse and combine to form hydrogen gas bubbles that take the volume and

form pits. When the catalytic sites can convert atomic hydrogen into molecular hydrogen, the gas bubble is formed and grows bigger until it is beyond some critical size, then the gas bubble desorbs and leaves a pit on the surface.

1.3.3 Similar wet deposition process

There are two other forms of deposition through electrochemical reactions but without external current source, namely, electroless plating and displacement plating, in which the electrons are from the oxidation of a reducing agent and the metal substrate respectively. In displacement deposition, once the substrate is fully covered by the deposited metal, the process stops. Therefore, the thickness of the displacement deposited coating is thin, and the application is limited. We will introduce the electroless deposition process in detail in the next section. To note that electroless deposition shares a lot of common features with electroplating, therefore some of the microstructure control principles also apply to electroless deposition.

1.4 Electroless deposition

Electroless deposition is the process of metalizing a surface in the absence of an external electrical source. Its fundamental principle is very similar to electroplating, with the major difference being the reduction power is supplied by a reducing agent other than an external current. It has some obvious advantages over the metallic coating techniques in the preceding sections. It requires the simplest processing equipment and little external energy input. But the relatively low deposition rate and undesired porosity in the coating impose some disadvantages to this technique. In this section, the major aspects of the electroless plating are introduced.

1.4.1 Discovery of the electroless deposition

The discovery of electroless plating dates back to 1844 when French chemist Charles Wurtz accidentally produced black nickel powders from an aqueous solution consists of nickel salt and hypophosphite⁶⁰. At that time, electroplating was gaining popularity in Europe as decorative coatings, therefore the metal powder generated was not used in practical application. The research did not have a breakthrough until the twentieth century. In 1916, Roux was granted the patent to produce metallic layers or films on objects. But the plating bath Roux used was not stable and required to add the metallic salts or reducing agent little by little to avoid uncontrolled precipitation to form metal powders⁶¹. The first controllable electroless plating was reported in 1946 by Abner Brenner and Grace Riddell⁶², and the patent was granted in 1950⁶³.

1.4.2 Deposition principle and microstructure

To enable a controlled electroless deposition of metals, the composition of the plating bath is critical. Generally speaking, there are four components in the plating bath, i.e., a source of nickel ions, a reducing agent, suitable complexing agents, and stabilizers⁶⁴. The reducing agent and metal salt are the key components for the metal ions reduction, in which the metal ions obtain electrons from the oxidation of the reducing agent. The electroless plating of nickel is most widely applied. Therefore, the following contents are based on the electroless plating of nickel.

1.4.2.1 Deposition principle

The thermodynamic driving force is the same as the electroplating but the free energy difference of the reaction is big enough to support the reduction reaction without

applying the electric current. The driving force can be represented by the electromotive potentials in acidic and alkaline baths.

The electroless deposition is a heterogeneous catalytic process in liquid-solid interfaces, which is the core step in various industrial processes, such as electrocatalysis, oil refinery, and water treatment, etc⁶⁵.

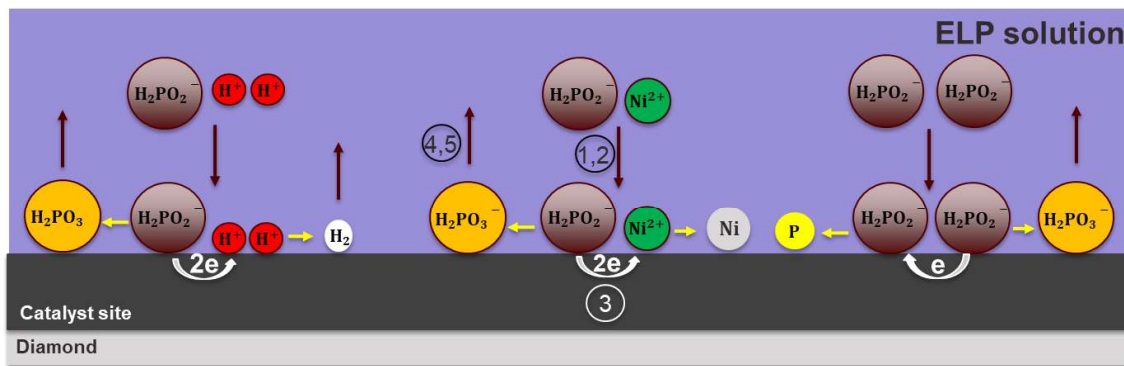


Figure I.2. Schematic of the electroless plating process: ① Diffusion to active sites, ② Adsorption ③ Reaction, ④ Desorption, ⑤ Diffusion away from the surface.

The process of nickel electroless deposition is illustrated in Figure I.2 with the hypophosphite as the reducing agent. The reactants first diffuse to the catalytic sites of the substrate and are adsorbed onto the surface of the catalytic sites. The adsorption in the deposition condition is an exothermic process, which lowers the energy of the adsorbate in the adsorbed state. When the reactants are in the adsorbed state, their electron structures will be modified, so dissociation of their components and a chemical reaction would be possible. This overall reaction is usually exothermic as well. The heat released by the adsorption and reaction provides the energy needed to overcome the

reaction barrier in the intermediate steps. The reaction products will either be adsorbed on the surface or desorb and diffuse to the solution depend on the form of the product.

The above heterogeneous catalytic process applies to both the solid-gas interface and the solid-liquid interface. The latter is more complex because there are multiple interactions between reactant ions and other ions and molecules in the solvent. Besides, when the substrate is immersed in the solution, the electrostatic layer near the solid-liquid interface affects the distribution and behaviors of ions in its vicinity. As noted by Lambert, the presence of solvent at the solid-liquid interface causes great complexity in both the acquisition and interpretation of the data in the liquid phase catalysis⁶⁵. Therefore, research in this regard is not fully developed.

1.4.2.2 Microstructure of electroless Ni-P deposits

The electroless deposited films are featured with polycrystalline or amorphous metallurgical structure and embedded porosity as sketched in Figure I.3.

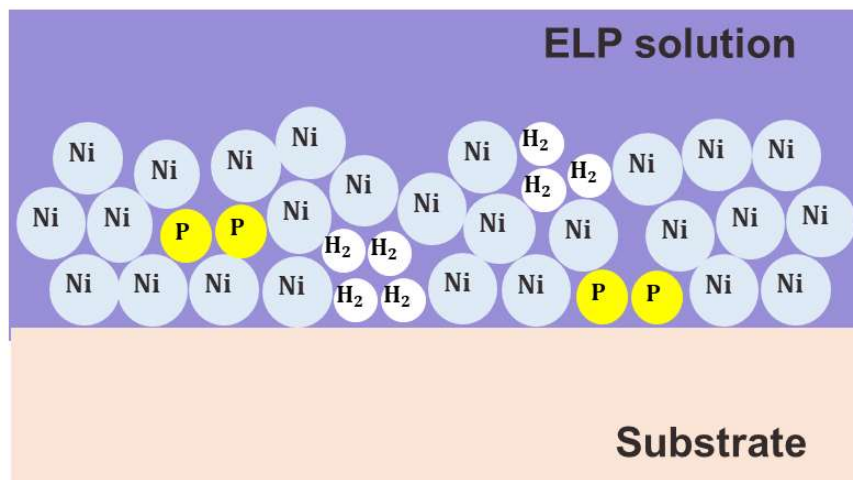


Figure I.3. Microstructure features which cause intrinsic stress in the electroless Ni-P coatings.

Due to the incorporation of P or B atoms in the deposits, the electroless plating films are polycrystalline materials with fine grain size or an amorphous structure. Similar to the metallurgical structure described in the electroplating process, the crystallinity depends on the percent of phosphorus in the coatings and other plating conditions.

The hydrogen atoms generated in the plating process can combine to form the gas bubbles and occupy the volume at some sites of the coating. This prevents the alloy from depositing at that site leave pores in the coating.

Sometimes, nodular surface morphology and layered structure also appear in the coating. According to Watanabe, the electrolessly deposited film grows laterally, and the layered structure is generated. This lateral and layered growth is due to the depletion of reactants in the solution layer above the plated film and thus won't support the growth in the thickness direction. A schematic of the lateral growth is sketched in Figure I.4, which is adapted from Figure 2.23 in Watanabe's book: *Nano Plating*⁴⁷. When the reactants are supplied to the interface again by diffusion or fluid flow, the next layer of film will be deposited again⁶⁶. Therefore, the growth rate of electroless plating depends on the solution concentration, plating solution temperature, and the condition of mixing. The thickness of each layer is a few tens of nanometers⁴⁷.

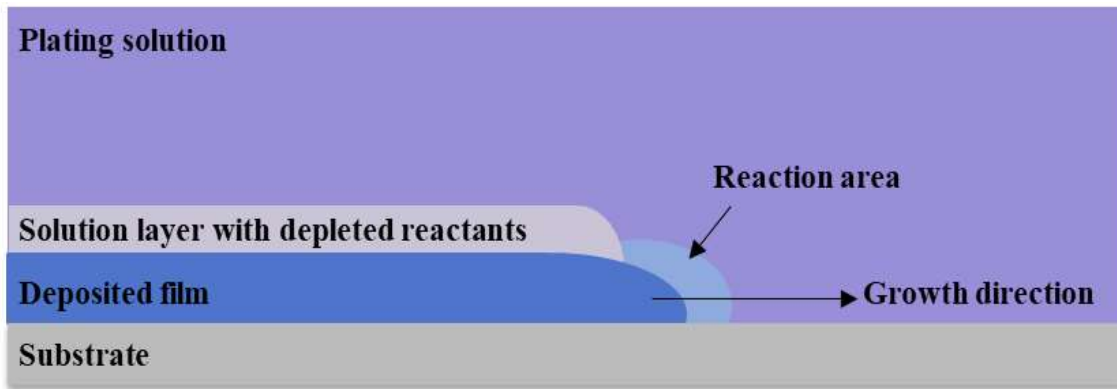


Figure I.4. Schematic showing a mechanism of electroless film formation. Adapted from reference [47].

1.4.3 Factors influencing the deposition process

The deposition process is influenced by many factors including the components and concentration of the plating bath, the pH, plating temperature, agitation conditions, pretreatment, and post-treatment. The variations in the deposition condition result in different microstructures and coating properties. For example, the phosphorus content which influences the hardness, wear resistance, corrosion resistance, and magnetic susceptibility is dependent on the reducing agent concentration, pH value, etc. The effects of some important factors on the deposition process and the resulting microstructure and coating properties are discussed below.

1.4.3.1 Nickel salts

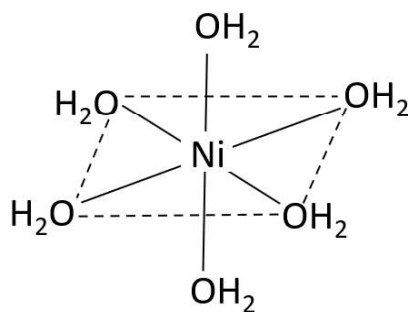
The commonly used nickel salts are nickel sulfate, nickel chloride, and nickel acetate. The different anions lead to different viscosity of the plating bath and influence the diffusion process differently. If nickel chloride salt is used in plating a corrosion

protection coating on steel, the chloride ions may attack the steel substrate and leave pittings, which will deleteriously degrade the quality of the protective coatings^{67, 68}.

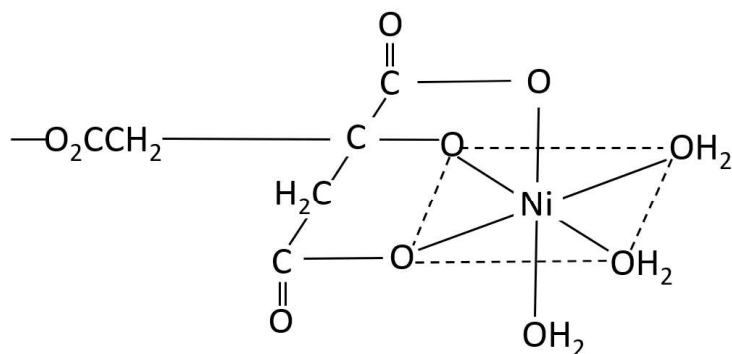
1.4.3.2 Complexing agents

The function of complexing agents is to control the free nickel ions concentration in the plating bath. They act like cages and trap the nickel ions in the center. So even the reducing power is high in the solution, the reaction rate won't be high if most of the nickel ions are complexed with the complexing agent. On the other hand, it increases the solubility of the metal ion in the plating bath, so the nickel salt of low solubility won't precipitate. Complexing agents usually have one or more electron donor atoms like oxygen or nitrogen atoms, which can form coordinate-covalent bonds with nickel ions. Examples of the complexing agents are chloride ions, ammonia, amines, and organic compound like citrate, EDTA, tartrate. Coordination complexes consist of a central metal atom or ion bond to the functional groups known as ligands. If a complex agent doesn't fully coordinate with all the coordination positions of the nickel ion, the water molecules will take the position. And in a reaction, these weakly coordinated nickel ions are easy to be hydrolyzed and participate in the reaction. In Figure I.5, a nickel ion coordinated with six water molecules and a citrate molecule is illustrated, adapted from Mallory's book⁶⁹.

The use of complexing agents is not environmentally friendly because the complexing of the heavy metal ion in the wastewater has been a hazard for the environment. Therefore, wastewater treatment after electroless plating is a necessary step in the industry⁷⁰.



(a)



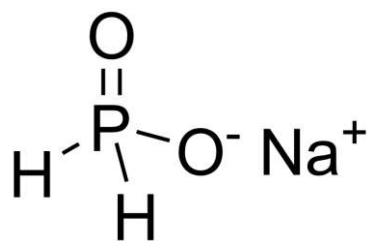
(b)

Figure I.5. Complexing of a nickel ion with (a) six water molecules and (b) citric acid. Adapted from reference [69].

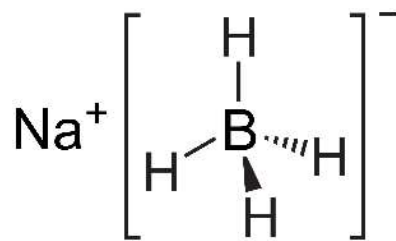
1.4.3.3 Reducing agents

There are also several choices for reducing agents. The most widely used one is sodium hypophosphite, while sodium borohydride, dimethylamine borane (DMAB), and hydrazine are also used for some specific situations where hypophosphite is not desired.

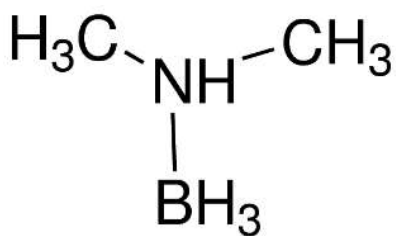
The molecular structure of these reducing agents is shown in Figure I.6.



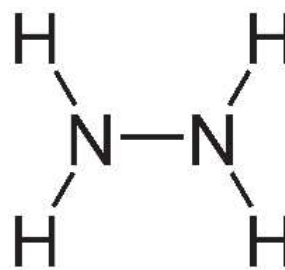
(a)



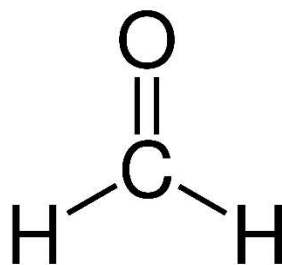
(b)



(c)



(d)



(e)

Figure I.6. The molecular formulas of four commonly used reducing agents for electroless plating (a) sodium hypophosphite, (b) sodium borohydride, (c) dimethylamine borane (DMAB), (d) hydrazine (e) formaldehyde.

From the molecular structure of these reducing agents, it is noticed that all center atoms are bonded with more than one hydrogen electrons. These phosphorus-hydrogen, boron-hydrogen, nitrogen-hydrogen, or carbon-hydrogen bonds are relatively unstable thus are easily broken to give off electrons.

The composition of the deposited material depends on the type and concentration of the reducing agent. The as-plated coatings generated from electroless plating contain either phosphorus, boron, or nitrogen if hypophosphite, boron hydride (or dimethylamine borane), or hydrazine is used as the reducing agent, respectively. If formaldehyde is used as the reducing agent, pure metal can be generated in the deposits.

For the electrolessly deposited Ni-P alloy, the weight percentage of phosphorus in the coating usually ranges from 4% to 15%. The phosphorus content in the Ni-P coating is due to the co-deposition of phosphorus from the sodium hypophosphite reducing agent⁷¹. The amount of phosphorus content in the alloy is affected by the ratio of reducing agent to nickel salt, pH values, etc. The crystallinity (or amorphousness) of the coating can also be tuned by those operation parameters.

1.4.3.4 pH value

The pH value is an important parameter to control the plating process. For a specific system, only when the pH falls into a certain range, the plating process is possible.

pH can be maintained by adding some reagents called pH buffer. Commonly used pH buffers are weak acids or weak alkalis such as acetic acid, ammonia. Some complexing agents act as pH buffers at the same time.

1.4.3.5 Stabilizers

Stabilizers are used to avoid solution decomposition during the plating process. Solution decomposition is also called solution plating out, which is used to describe the phenomenon that fine powder of the alloy instead of coatings on the substrate are formed. The mechanism of stabilizing the plating solution is by inhibiting the hydrogenation/dehydrogenation catalysis⁷². Therefore, the stabilizers are also called inhibitors.

1.4.3.6 Operation factors

In the electroless deposition process, the following operation factors also influence the plating process.

Temperature

Like most of the chemical reactions, the temperature is the most important factor to influence the deposition rate. Below the critical temperature, the reaction does not occur. The higher the temperature, the faster deposition occurs. However, high operation temperature also means high energy input which increases the cost of the process.

Agitation

The main purpose of agitation during the plating is to enhance the diffusion of reactants to the reaction sites. Another function of agitation is to help release the hydrogen bubbles attached to the reaction surface, which can also be facilitated by adding surfactants^{73, 74}.

Replenish of the plating bath

Due to the consumption of the reactants in the plating bath, from time to time, the fresh plating bath is added into the plating tank. The time interval of these replenishments affects the coating compositions at different depths of the coating. Some manufacturers developed a bath monitoring and replenish system to maintain consistent bath concentration and uniform film composition⁷⁵.

1.4.4 Applications

The electroless Ni-P coating has many advantages such as good mechanical, magnetic, tribological, electrochemical properties. Therefore, it is widely used for corrosion-resistant and wear-resistant coatings. It is also suitable to deposit films on complex geometric surfaces such as through-holes and blind recesses (vias) in the printed circuit board due to its uniform thickness, good solderability, and ability to deposit on non-conductive materials. The electroless deposition has also been implemented to metalize the interconnects for ultra-large-scale integration (ULSI) technology^{23, 26, 76, 77}. Electroless deposition of ternary and quaternary alloys⁷⁸⁻⁸² and metal-ceramic composite⁸³⁻⁸⁷ or metal-polymer composites⁸⁸⁻⁹⁰ are also under the spotlight of current research because of the unique and tunable properties of the deposited materials. Some of the applications of electroless deposition of Ni-P are introduced below.

1.4.4.1 Corrosion and wear-resisting coating

Electroless plating is known to produce uniform, hard, wear-resistant, and corrosion-resistant coatings⁹¹. Lots of experiments have been done to investigate the

corrosion and wear resistance of the electrolessly plated coating on different metal substrates as the protective layer. These coatings are usually used in oil and gas industries or other pipelines that are susceptible to corrosion and erosion^{22, 92, 93}. The electroless Ni-P coatings are also widely used to coat the metal with higher corrosion rates such as magnesium and aluminum alloys^{94, 95}.

The typical failure mode is through the corrosive electrolyte attacking the coating and poor adhesion of the coating to the substrate²¹. Most of the researchers used the electrochemical method to characterize the corrosion resistance of electroless Ni-P⁹⁶. Typically, the corrosion resistance of the coating depends on the phosphorus content, the alloy elements, the crystallinity, the porosity, and composite components in the coating⁹⁷⁻¹⁰⁴.

1.4.4.2 Catalyst for energy and environment applications

The gradual switch from fossil fuel to clean and renewable energy resources is the trend of global development, which alleviates the energy crisis and environmental issues. Hydrogen is a form of clean energy, which can be used to generate electricity either in a fuel cell or through combustion. The generation of hydrogen gases using electricity generated from renewable energy such as solar cells and the wind turbine is a sustainable way.

The typical catalysts for the water-splitting reactions in which water is converted into oxygen and hydrogen¹⁰⁵ are precious metals such as platinum, palladium, and rhodium. However, the vigorous generation of hydrogen gas at the Ni-P surface is an indication that the electroless plated Ni-P is a promising candidate for the hydrogen

evolution reaction. Furthermore, the abundance of nickel in the earth makes it promising to substitute for those precious metals.

Some other applications of the electroless Ni-P alloy are the catalyst for water treatment, fuel cells, rechargeable batteries, and supercapacitors¹⁰⁶⁻¹¹⁰. The electrocatalytic properties of nickel are from its multiple oxidation states and the layered structure of some of its oxide and hydroxyide^{111, 112}.

The catalytic performance of different metals is demonstrated by a volcano plot¹¹³ in which pure nickel has lower catalytic activity. There are several ways to improve the effectiveness of catalysts. The catalytic activity of the material is affected by the composition and microstructure, especially the defects distribution on the material¹¹⁴. Therefore, doping and alloying different elements to the base materials have been popular research directions^{115, 116}. Researchers have also been developing the atomic-sized catalysts and try to distribute them on a porous substrate to increase the contact area between the reactant and the catalysts¹¹⁷.

1.4.4.3 Coatings for abrasive tools

Coated abrasives such as coated diamond particles can effectively increase holding force between the abrasive particles and the matrix, reduce thermal shock, improve heat dissipation, protect the diamond from oxidation or graphitization in high-speed cutting. Therefore, coated abrasives are a better choice for electroplated and polyimide bonded or phenolic bonded tools¹¹⁸⁻¹²⁰.

Diamond-wire saw is an example of the abrasive tools, which has been widely used in semiconductor and construction industries to slice hard and brittle materials.

Compared with wire saws using loose abrasives, the fixed-abrasive saws were found to have higher productivity and generate less kerf loss and better surface finish^{121, 122}. Generally, the diamond abrasives are bonded to the wire in two ways, resin bonding or electroplating. Compared to the resin bonded diamond wire saw, the electroplated one has higher wear resistance^{123, 124}. However, the electroplated diamond wire tool is more expensive due to the low electroplating rate.

The electroplating method to make diamond wire saw is illustrated in Figure I.7. The steel wire is fed into the solution tank by the rotating reels, and a current is applied to the steel wire(cathode) and the nickel rod (anode). Then the nickel deposits will build upon the steel wire and bond the diamond abrasives suspended in the bath onto the wire surface. This electrodeposition of nickel is slow because the consumption of the ions near the steel wire lowers the current density¹⁸. The use of nickel-coated diamond abrasives can improve the plating rate and reduce the cost of manufacturing^{125, 126}. Besides the benefit of the electrical conductivity of the coating, the ferromagnetic properties from nickel can also increase the density of abrasives bonded to the steel wire. The electroless plating method is commonly used to coat the diamond abrasives^{32, 127}.

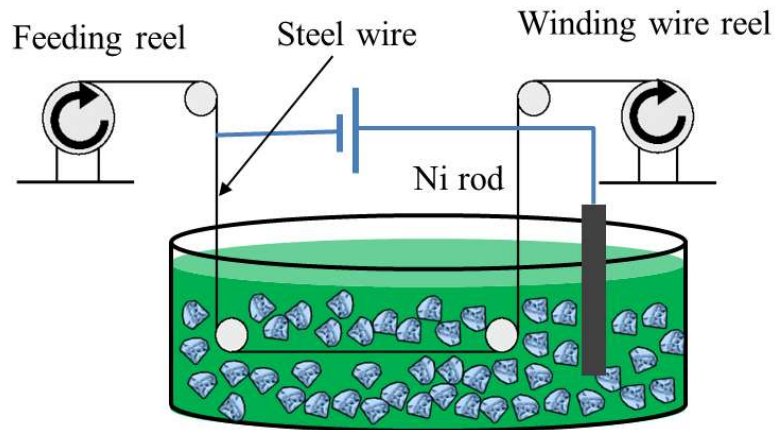


Figure I.7. The manufacturing process of electroplated diamond wire saw.

Failures of the electroless deposited coatings on the diamond particles were seen frequently in the electroplating process in Figure I.7. The failure is due to the harsh working environment of the coated particles. The electroplating solution is corrosion with a pH value in the range of 3.5 to 5.1 and the deposition temperature is from 40 to 60 °C. Besides, the solution is agitated to suspend the diamond particles, which will cause the particles to collide into each other and cavitation at the coating surfaces. Therefore, the coatings are subjected to corrosion and erosion.

The quality of electroless nickel coating is critical to the performance and service life of diamond wire saw. However, during the electroplating process, coating cracking and detachment from the surface of diamond abrasives were observed. The loss of coating will reduce the plating rate and the number of diamond particles on the wire, which will cause the inconsistency in product quality. Therefore, when the diamond grits with failed coating accumulated to a critical amount, the electroplating process must stop, and

removal of the diamond without coatings and the replenishment of the coated diamond is needed¹²⁸.

Non-stop manufacturing is important to financial success in the industry; hence the long-lasting coating is needed for the process. To develop a more durable coating, why and how does the coating fail need to be understood. The surface condition and electrochemical reactions in the solution can be accurately monitored by measuring the current through the coating. Other methods like weight change, nanoindentation, and microscale scratch method are commonly used for characterizing coatings¹²⁹⁻¹³¹. However, since the investigated system involves tiny diamond powder and aqueous solution, these methods either are tedious to obtain statistically sound information or cannot reflect the real condition. The electrochemical characterization of coatings on the abrasives hasn't been reported. Since the diamond is not conductive, and the powder is tiny, the design of the working electrode needs to be carefully considered.

1.5 Internal stress in electroless Ni-P coatings

The integrity of a coating is of great importance to its functionality. The rupture of coating and detaching of coating from the substrate may expose the substrate to the unfriendly environment and lose any protection or other benefit brought by the coating. The coatings usually suffer from failure due to the stresses, both external and internal stresses. External stress refers to the stress applied to the coating from an external source, usually in the form of indentation, peeling, and shearing. Internal stresses are the stresses that result from the microstructure. Sometimes, the internal stresses remain in the film when the causes of the stresses have already been removed, thus also called

residual stresses. Usually, a coating is easy to fail when the internal stress is high. Therefore, combining even with a small magnitude of external stress, the total stress will exceed the strength of the coating, and coating failure occurs.

The coating fails during the deposition process when the gained internal stresses during the deposition are too large. This kind of failure occurs frequently in sputtering, spraying, painting, spin coating, vapor deposition, electrodeposition, and electroless deposition if the coating processing parameters are not controlled well.

In this section, the forms of coating failures, the origins of internal stresses, methods to measure the internal stress, and the factors influencing the internal stresses in electroless Ni-P coatings are discussed.

1.5.1 Forms of coating failures

A thin film fails because the stresses are large enough to break either cohesive bonds within the film or adhesive bonds between the film and the substrate. In this context, we only consider the failure of the film itself or the interface, assuming the substrate is strong and tough and won't be damaged or yield. Only the elastic deformation of the substrate is included in the discussion.

There are two forms of coating failure: film crack, debonding, depending on the locations of the failure. Cracking of a film or layer is possible when tensile stress is developed and exceeds the cohesive strength of the coating. Debonding occurs either due to normal stress or lateral stress when the interfacial bonding is broken. Buckling-driven compressive stress is one of the causes of debonding at the interface. In a lot of situations, both forms of coating failure take place.

1.5.2 Origin of internal stress

The internal stresses in thin films have three contributions: extrinsic stresses, thermal stresses, and intrinsic stresses¹³². In this section, the origins of and the factors that influence these stresses are discussed.

1.5.2.1 Extrinsic stresses

Extrinsic stresses mainly refer to the stress produced by an external force applied to the film during the deposition process, which usually can be neglected in the vapor deposition process since almost no mechanic contact with the film occurs. However, in the liquid phase deposition process such as electrodeposition and electroless deposition, the deposited film is in close contact with the solution, the fluid flow caused by mechanical agitation may result in the extrinsic stress in the film. In some special electroplating and electroless plating processes, the solution is supplied with a brush, and the brushing movement also contributes to the extrinsic stresses¹²⁶. In an electroless plating process such as the research subject of this study, the plating involves massive particles in the solution. If mechanical agitation is used, the particle-particle collision and particle-container wall collision will cause the coatings are subjected to extrinsic stresses.

1.5.2.2 Thermal stresses

Thermal stresses arise due to changes in temperature when the film and substrate have different coefficients of thermal expansion (CTE). The coating failures caused by thermal stresses usually occur when the deposition process ends, and the temperature

drops from the deposition condition. For some systems, thermal stresses are huge (i.e., several GPa) and are the major causes of mechanical failure.

The thermal stress can be calculated using the following equation assuming purely elastic deformation

$$\sigma^T = \int_{T_0}^{T_f} \Delta\alpha \frac{E}{1-\nu} dT = \frac{E\overline{\Delta\alpha}\Delta T}{1-\nu} \quad \text{I-3}$$

where:

- σ^T is the thermal stress in the film,
- T_0 is the deposition temperature,
- T_f is the temperature of the environment where the film is transferred to after deposition,
- $\overline{\Delta\alpha} = \frac{1}{\Delta T} \int_{T_0}^{T_f} \Delta\alpha dT$, is the average of the difference in thermal expansion coefficient between temperatures of T_0 and T_f ,
- E is the elastic modulus of the film,
- ν is the Poisson's ratio of the film.

From the definition and the equation for calculating the thermal stress, it is obvious that the magnitude of temperature change and the difference in thermal expansion coefficients are the major factors that influence the thermal stress to deposit a certain coating. To mitigate the coating fracture due to thermal stress, slowly cooling down the coated system can be helpful since the strain rate is reduced¹³³.

1.5.2.3 Intrinsic stresses

Intrinsic stresses are also called growth stresses since they are mainly developed during the growth of the coating. Depending on the process, the deposition temperature can be “low” or “high” compared to room temperature, but intrinsic stresses are present at the deposition temperature even without temperature change. The intrinsic stress is due to the accumulating effect of the crystallographic flaws that are built into the coating during deposition¹³⁴. Typically, any cause leads to the volume change in the film that will produce intrinsic stresses, as long as the film is still constrained by the substrate. When the coating tends to reduce in volume and shrink but constrained by the substrate to do so, it is under tensile stress. When the coating tends to expand by increasing in volume but limited by the substrate to achieve the desired expansion, it is subject to compressive stress.

The common origins of the intrinsic stresses include lattice misfit, crystallite coalescence, defect annihilation, impurities inclusion, and phase transition¹³⁵.

There are only qualitative or semi-quantitative models to explain different origins' effects on the intrinsic stress, which are summarized below.

Lattice Misfit

When a single crystal thin film is deposited epitaxially on a single crystal substrate, there will usually be intrinsic stress caused by lattice misfit. The misfit stresses arise when films are coherent with the substrate materials, i.e., the lattices are matching at the interface. Due to the difference in lattice parameters of the two materials in their

free-standing form, the misfit strain results in misfit stress. An illustration of this stress origin is presented in Figure I.8, which is adapted from Figure 6 of Nix's paper¹³⁶.

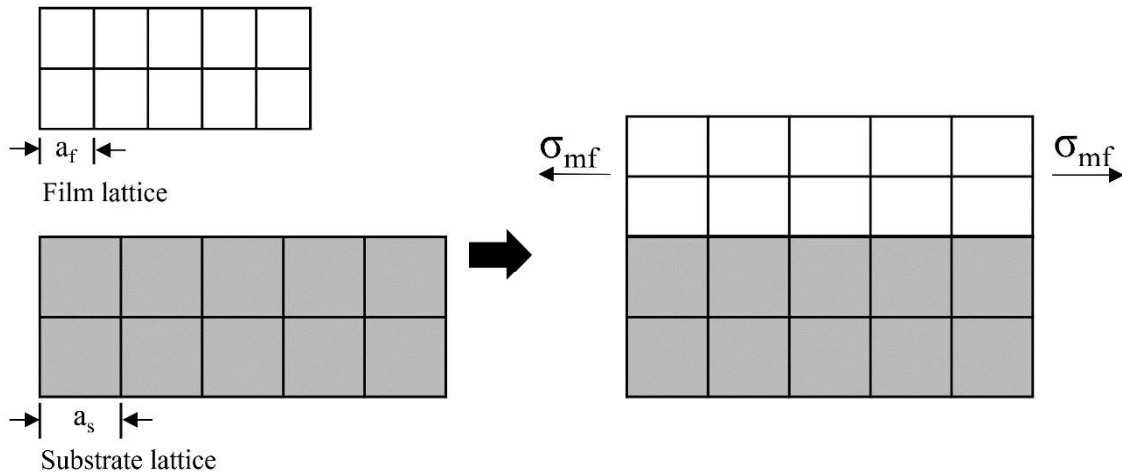


Figure I.8. The difference in lattice constants leads to misfit stress in the film.

Adapted from reference [136].

For a sufficiently thin film, the misfit strain can be calculated by the bulk material lattice parameters by

$$\epsilon_{mf} = (a_s - a_f)/a_f \quad \text{I-4}$$

where, ϵ_{mf} is the misfit strain; a_s and a_f are the lattice parameters of the substrate and film material, respectively.

For thicker films, there will be misfit dislocations at the interface to reduce the stress in the film. Therefore, the misfit strain and stress will be less than the thin film.

Crystallite coalescence

In the initial stage of film deposition, tiny isolated crystallites islands are formed. As the crystallites grow larger, the gap between the crystallizes decreases. When the

distance between two crystallites becomes small enough, the interactions (cohesion force) between crystallites can be strong enough to close the gap by elastic deformation. When the coalescence occurs, tensile stress will be created, which is illustrated in Figure I.9, which is adapted from Figure 2 in Nix and Clemens's paper¹³⁷. In this process, cohesion is developed within the driving force to reduce the surface energy by creating low energy grain boundaries¹³⁷⁻¹³⁹.

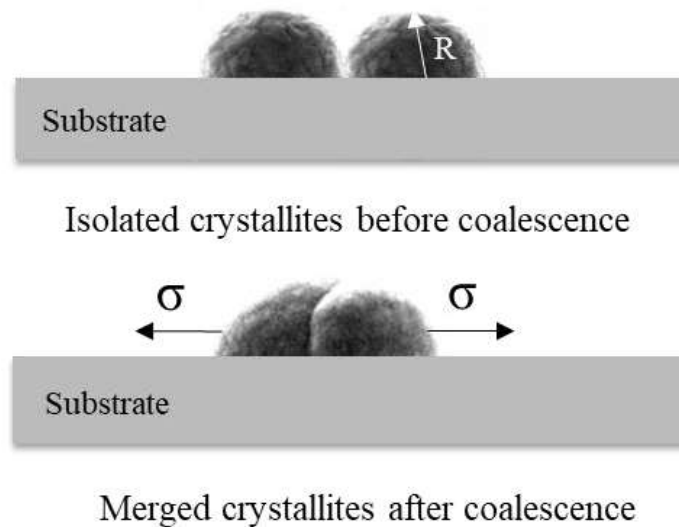


Figure I.9. The sketch illustrates the tensile stress developed due to crystallites coalescence. Adapted from reference [137].

Defect annihilation

The defects generated in the film deposition process could be annihilated by diffusion. These defects, which could be annihilated, include vacancies, dislocations, and grain boundaries.

Vacancy annihilation would reduce volume was a film free to contract. Thus, a film on a substrate would develop intrinsic tensile stress if it experienced vacancy annihilation.

The grain growth is accompanied by the merge of grains and eliminating grain boundaries. The grain boundaries are the places where the atoms are less densely arranged than inside the grain. Therefore, reducing the grain boundaries also generates tensile stress in the film.

Recrystallization occurs when the coatings are subject to heat during the deposition process. It is associate with eliminate residual stress, create new grain boundaries from rearrangement of existing dislocations, and grain growth. At high substrate temperatures, the film recrystallizes completely, so the stress is low. At very low substrate temperatures, no rearrangement is possible; hence the stress is also small¹³⁹.

Impurities inclusion

The impurity is another defect form that results in either compressive or tensile intrinsic stress depend on whether the impurity atoms occupy an interstitial site or substantial site of the lattice and also depend on the atomic size of the impurity atom.

Phase transformations

Phase transformation usually changes the volume of the film due to the lattice parameter change in different phases, which results in the intrinsic stresses.

1.5.3 Methods to measure internal stress

There have been several methods to measure the residual stresses in a deposited film¹⁴⁰. The most commonly used method to quantify the residual stress is to directly measure the deflection of a thin substrate upon which the film is deposited. The typical geometry of the substrate is a thin strip of metal^{141, 142}. Due to the residual stress remaining in the coating after deposition, the thin strip will curve with the deposited film. Some modifications of the strip-like Brenner Senderoff spiral contractometer magnifies the reading¹⁴³. The stress can be calculated from the curvature of the strip by:

$$\sigma_f = \frac{1 + \frac{E_f(1-\nu_s)(h_f)^3}{E_s(1-\nu_f)(h_s)^3}}{1 + \frac{h_f}{h_s}} \frac{E_s h_s^2}{6(1-\nu_s)h_f} \kappa \quad \text{I-5}$$

where: σ_f is the stress in the deposited film. E , ν , h are Young's modulus, Poisson's ratio, and thickness, respectively. The subscripts: s and f represent the substrate and the deposited film. κ is the curvature of the strip, which can be calculated from the shape of the strip after deposition:

$$\kappa = 1/r = \frac{8d}{4d^2 + L^2} \quad \text{I-6}$$

Where κ demotes the curvature, and it is the reciprocal of the radius of the curvature r . d is the height of the arc, and L is the length of the strip, seen in Figure I.10, adapted from Figure 1 in Chen et al's paper¹⁴¹.

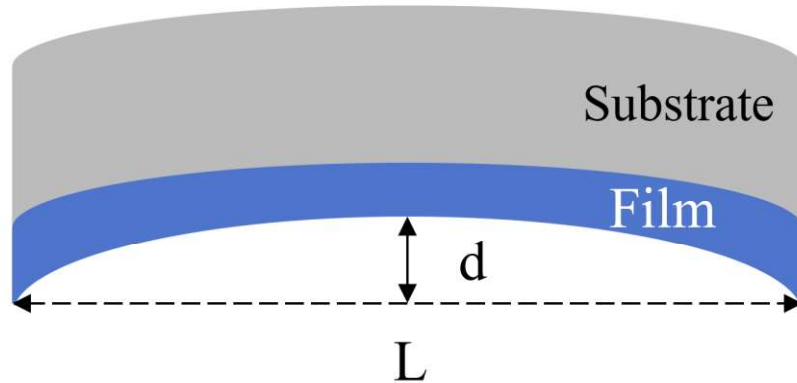


Figure I.10. Strip deflection caused by the stress in the deposited film. Adapted from reference [141].

For deflection in a very small magnitude in which the curvature is not observed from the cross-section, optical fringe measurements are generally conducted using interferometry^{144, 145}. If the anisotropic stresses exist in the film, a circular substrate clamped at the center is used for the measurements. If only scalar stress is needed, the cantilever beam technique is used^{146, 147}.

Another way to measure the residual stress through the substrate deflection is to apply an end loading on the substrate to restore the position. The force needs to do so is measured, which can be used to calculate the residual stress¹³⁹.

The methods described above measure the total residual stress. In some cases, the thermal effect is inevitable even though the temperature of the deposition environment is closely monitored and controlled. For example, the deposition energy, either release by discharge or condensation, will heat the film and the substrate and cause the temperature to increase. The increased temperature then leads to heat dissipation through conduction

to the thermal sink connected to the substrate, and through convection and radiation to the environment. To minimize the thermal effects, one can use a substrate that is short and thick or use a substrate material with a similar thermal expansion coefficient as the film material^{139, 148}.

1.5.4 Factors influencing internal stress

Intrinsic stress in the deposited coating is induced by the microstructure change of the film. The microstructure of the deposited coatings is mainly controlled by the composition of the deposition solution and the operation conditions¹⁴⁹. Experimental studies were carried out to find the critical factor that influences the residual stress in the coating.

Researchers found that high pH and solution aging affect intrinsic stress significantly, which is through the change of the deposition rate^{141, 150}. The components in the plating bath, such as complexing agent, stabilizer, or inhibitors, also affect the stress either from tensile to compressive or from compressive to tensile¹⁵¹. Since coalescence of deposit nodules create tensile stress in the coating, coalesces inhibitor-saccharin was added to the plating solution to reduce the tensile stress. It also has an effect of brightening the electroless Ni-Cu-P coating on aluminum substrate¹⁵².

Research also studied the internal stress with the composition and microstructure of the coating and found that the stress is compressive with low phosphorus content and change positively to tensile stress when the P% increases and revert to compressive stress when P% further increase to be larger than P%¹⁵³. The residual stress was found to change to the compressive direction when the thickness of the coating increases¹⁴⁵. The

phase transformation from the amorphous Ni-P phase to crystalline Ni and Ni₃P gives rise to a tensile stress burst during heat treatment¹⁵⁴.

The thermal factor may also be an important contribution to the residual stress in the electroless Ni-P coatings since the plating temperature is usually above room temperature and sometimes can approach 100 °C. The big temperature drop from the deposition condition to the room temperature will result in the contraction of the coating and the substrate when the sample is taken out of the plating solution. If the thermal expansion coefficients are different, the thermal residual stresses are left in the film. Considering a Ni-P electroless coating on the diamond substrate, the coefficient of thermal expansion (CTE) of Ni-P and diamond are $12\sim 13\times 10^{-6} \text{ }^{\circ}\text{C}^{-1}$, and $0.7\times 10^{-6} \text{ }^{\circ}\text{C}^{-1}$, respectively^{155, 156}. The deposition at 70 °C results in thermal stress of about 50 MPa when the sampled is cooled down to room temperature.

1.6 Summary

In this chapter, the background of coating depositions is introduced to link the processing methods with the microstructure and properties of the coating materials.

The principles of the vapor deposition methods and liquid phase deposition methods to generate coatings are introduced and compared. The microstructure features of the coatings deposited and the factors that affect the microstructures are discussed. Finally, the internal stresses of the coatings and methods to study them are introduced.

This chapter provides the theoretical and technical background for the research goal which will be proposed in the next chapter.

CHAPTER II

MOTIVATION AND OBJECTIVES

2.1 Motivation of this research

The electroless coating on diamond particles has been widely used to make machining tools, as described in chapter I. The coatings can significantly improve the quality of the tools compared to uncoated diamond abrasives. However, under the following procedures in tool manufacturing, the coatings need to survive from a harsh environment, which may cause the coating to detach from the substrate. The functionality of the coating relies on the integrity of the coating and good adhesion on the substrate. Therefore, the coating properties are necessary to be characterized by the plating conditions to generate coating of good quality.

Another challenge is that it is difficult to characterize the coatings on fine particles electrochemically and mechanically. Due to the free movement of the particle in the deposition process, the study of the morphology evolution of the electroless plating is difficult, if not impossible.

The likelihood for the coating to fail depends on the properties of coatings. Porosity, composition, residual stress are the major ones that affect the coatings' erosion and corrosion behaviors. The porosity, which is caused by the evolved hydrogen gas during the deposition, leaves the paths in which fluid can penetrate and cause crevice corrosion¹⁵⁷. The composition of the coating, mainly the phosphorus content, can influence the coating's crystallinity and corrosion resistance^{142, 158, 159}. The mismatch of

substrate and coating, spatial deposition rate change and composition change can lead to the local stress concentration in the coating. These three properties together also determine the mechanical strength of the coating.

Besides, for coatings that are deposited on some non-conductive materials, the binding force mainly comes from the mechanical locking or van der Waals forces between the substrate and coating material. This force can be extremely large if the two surfaces are brought close together with a large contact area. However, in the deposition process, lots of factors such as hydrogen bubble generation, foreign contaminants, and inefficient diffusion will cause the binding force to decrease dramatically.

The extent of corrosion and erosion also related to the morphology of the coating. The rougher surface has a larger exposed surface area to the solution and is easily attacked by flowing fluid.

All these properties are determined in the plating process. The research areas on electroless Ni-P coatings are summarized in Table II-1^{74, 160-164}.

Table II-1. Research areas on electroless Ni-P coatings

Research has been done	Research contents
Solution formulation	Reaction mechanisms Deposition rate Composition (p%)
Operation conditions	pH, concentration control Agitation, Impurity filtration
Heat treatment	Microstructure modification
Pre-treatment	Etching, Activation

It is noticed that few researchers studied the synergistic effect of substrate morphology and operation conditions on coating properties, which will be the focus of this study.

The motivations of this research area are to develop better electroless Ni-P coatings on the diamond particles substrate with better corrosion resistance and coating integrity.

2.2 Objectives

The first objective of this study is to develop effective methods to evaluate the Ni-P coating on diamond grits in the diamond tool manufacturing process.

The second objective is to find the coating failure mechanism and a model to describe the coating morphology evolution in the process that causes the coating failure.

2.3 Research approach

The following methodology was followed to reach the objectives of this research. Since the coating needs to survive from the corrosive environment, the corrosion resistance needs to be characterized. The electrochemical characterization can provide plenty of information indicating the coating condition change. It can also tell the catalytic activity of the coatings. Therefore, one major branch of this research is the electrochemical characterization of the coatings.

Morphology change of the coating indicates the coating's response to the different environments; therefore, the other investigation method is through morphology characterization. In this study, several microscopic and tomographic methods are used for this purpose, which is described in detail in the next chapter.

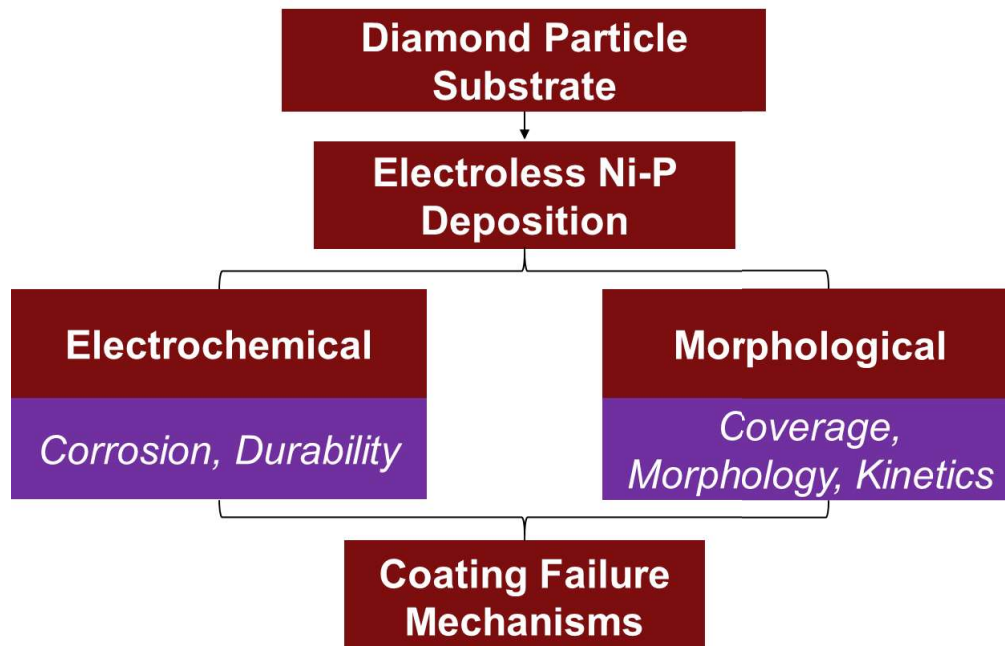


Figure II.1. Research flow chart.

2.4 Dissertation structure

Chapter I will give an introduction of different film deposition methods and the factors which influenced the microstructure and properties. The motivations and objectives will be presented in Chapter II. Materials and methods to characterize and investigate the coating performance will be presented in Chapter III. The corrosion resistance of the electroless Ni-P coating will be presented in Chapter IV. Chapters V presents the morphology of the coatings and the deposition kinetics of the coating on diamond particles. Chapter VI analyzes and explains the mechanisms of coating failure on diamond particles. Conclusions and future recommendations will be given in Chapter VII.

CHAPTER III

MATERIALS AND METHODS²

In this chapter, the coating synthesis processes for different applications are described, followed by the methods in characterization of the microstructure and composition. The electrochemical study is carried out to examine the coatings' performance as the abrasive coating and electrocatalyst. And finally, the morphology evolution characterization using the X-ray tomography methods is introduced.

3.1 Electroless plating setup and process

The plating was performed on loose diamond abrasives and specifically designed electrodes for subsequent characterizations for different purposes.

3.1.1 Electroless plating process for electrochemical characterization

The diamond abrasives of the size 88-105 μm (140-170 mesh) were used as the substrate for plating. Before the electroless plating, the substrate needs to be pretreated to form Pd catalyst sites on the surface. The pretreatment process is sketched in Figure III.1. The electrode with diamond substrates was cleaned in acetone and then immersed in 10 vol.% H_2SO_4 solution for pickling to remove organic and oxide. After this, the electrode was immersed in the SnCl_2/HCl solution and PdCl_2/HCl solution for sensitization and activation, respectively. The sensitization and activation details are

²Part of this chapter is reprinted with permission from “Electrochemical Characterization of a Nickel-Phosphorus Coating on Diamond Grits” by Lian Ma, Xihua He, Alex Fang, and Hong Liang, *Materials Performance and Characterization* **2018**, 7(3), 266-280, Copyright [2018] by ASTM International.

shown in Table III-1. The above pretreatment steps were all done at room temperature, and proper rinses were conducted between steps. The diamond particles are let dry in air after the final rinse.

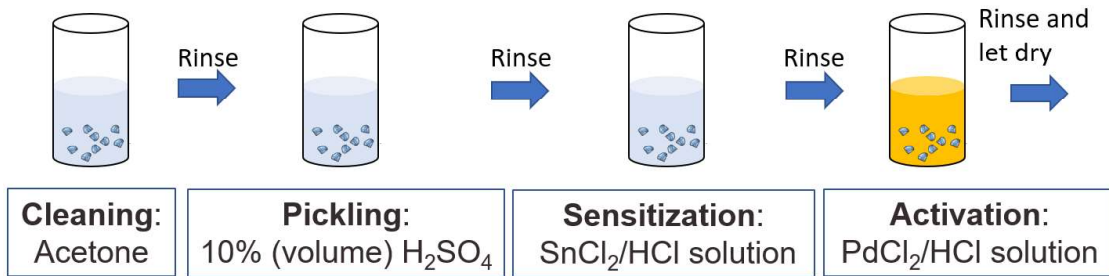


Figure III.1. Pretreatment process of diamond abrasives for electroless plating.

Table III-1 Pretreatment details

Treatment	Chemicals	Concentration	Immersion time (min)
Sensitization	SnCl ₂ ·2H ₂ O	20 g/L	2
	HCl	40 mL/L	
Activation	PdCl ₂	0.5 g/L	1
	HCl	10 mL/L	

The electroless plating solution was prepared right before the plating. The components and concentrations are listed in Table III-2. The pH value of the solution was adjusted to 10 by NH₄OH, and the bath was heated to 70°C using a thermostatic bath. The electroless plating set up is shown in Figure III.2. The plating time was 15 min.

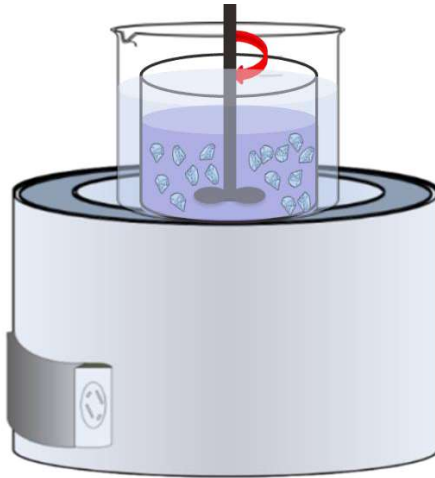


Figure III.2. Electroless plating setup.

Table III-2 Electroless plating solution components and concentration

Chemicals	Concentration (mol/L)
Nickel Sulfate hexahydrate, $\text{NiSO}_4 \cdot 6\text{H}_2\text{O}$	0.1
Sodium hypophosphite monohydrate, $\text{NaH}_2\text{PO}_2 \cdot \text{H}_2\text{O}$	0.4
Trisodium citrate dihydrate, $\text{C}_6\text{H}_5\text{Na}_3\text{O}_7 \cdot 2\text{H}_2\text{O}$	0.1
Ammonium sulfate, $(\text{NH}_4)_2\text{SO}_4$	0.1

3.1.2 Electroless plating process for tomography characterization

Diamond grits in the range of $400\mu\text{m}$ to $600\mu\text{m}$ (30-40 mesh) were used as a plating substrate. The same pretreatment procedure was carried out, as described in 3.1.1. The diamond grits are first cleaned with acetone and then with 10 vol.% H_2SO_4 in an ultrasonic cleaner for 5 min to remove organic and oxide contaminants. Then the diamond grits are immersed in 20g/L SnCl_2 aqueous solution for sensitization and

activated in 0.5g/L PdCl₂ aqueous solution to deposit Pd catalytic sites on the diamond surface. The sensitization and activation solution compositions are listed in Table III-1. Between every two steps mentioned above, the diamond grits are rinsed in deionized water.

Four different plating solutions are made with varying concentrations of sodium hypophosphite, while the concentrations of other components are the same. The compositions of plating solutions are listed in Table III-3.

Table III-3 The Electroless plating bath components and concentrations

Chemicals	Concentration (mol/L)
Nickel Sulfate hexahydrate, NiSO ₄ ·6H ₂ O	0.1
Sodium hypophosphite monohydrate, NaH ₂ PO ₂ ·H ₂ O	0.1, 0.2, 0.3, 0.4
Trisodium citrate dihydrate, C ₆ H ₅ Na ₃ O ₇ ·2H ₂ O	0.1
Ammonium sulfate, (NH ₄) ₂ SO ₄	0.1

The molar ratio of nickel ion to reductant (hypophosphite ion) are 1:1, 1:2, 1:3, 1:4 respectively, therefore the plating solutions are denoted as Ni:P=1:1, Ni:P=1:2, Ni:P=1:3, Ni:P=1:4. The pH of all the four solutions is adjusted with ammonia hydroxide to 9. The pH values of the solution before and after adjusting are recorded and shown in Table III-4.

Table III-4 The pH values of the plating solution before and after adjusting

Plating solution	pH before adjusting	pH after adjusting
Ni:P=1:1	6.07	9.06
Ni:P=1:2	6.05	9.07
Ni:P=1:3	6.05	9.05
Ni:P=1:4	6.00	9.07

For each plating bath, around 50 pretreated diamond grits were dropped in the plating bath of 3 mL. The estimated bath loading is about 1.3 dm²/L (0.53 ft²/gal). At plating time of 5 min, 10 min, 20 min, 30 min, 60 min, and 180 min, several diamond grits were taken out from the solution and properly stored.

3.1.3 Nomenclature of samples

The coated diamond grits were labeled as Ni:P=1:1-5 min, Ni:P=1:1-10 min, ..., Ni:P=1:4-180 min, to indicate the plating bath and the plating time.

3.2 Chemical composition and surface morphology characterization

The chemical composition of the coating was obtained from the energy dispersive spectrum (EDS) associated with FE-SEM and X-ray diffraction (XRD) using Bruker D8-Focus X-ray powder diffractometer. The XRD measurements can also provide information about the crystallinity of the synthesized coatings.

The morphology of coating on diamond particles is examined by scanning electron microscope (SEM) (Vega, Tescan Corp.) and JEOL JSM-7500F ultra-high-resolution field emission scanning electron microscope (FE-SEM). A tabletop digital

microscope (Dino-Lite AM4113ZTS) was used to check the coating coverage on the diamond abrasives. Image processing software ImageJ version 1.52a was used for dimension measurements for some of the images taken.

The surface morphology of the activated diamond surface was evaluated using an atomic force microscope (Nano-R2, Pacific Nanotechnology) in noncontact mode to check the distribution of the palladium metal clusters. Nanorule (Pacific Nanotechnology, Inc.) program was employed for analysis and image processing.

3.3 Tomography of coatings on diamond particles

3.3.1 X-ray tomography

X-ray tomography is a powerful, non-destructive method to image the internal structure of a sample across length scales spanning orders of magnitude¹⁶⁵. Using X-ray tomography to analyze the Ni-P coated diamond abrasives allows us not only to see the morphology of coating but also from the inner layer of coating to find out the morphology of the diamond abrasives where the coatings are grown on.

The synchrotron X-ray micro-computerized tomography experiments were conducted at Advanced Light Source (ALS) beamline 8.3.2, Lawrence Berkeley National Lab. The X-ray from the synchrotron source is filtered by a monochromator and selected energy level exit. Then by opening the shutter, the monochromatic X-ray beam shines on the sample on a rotational stage. Some X-ray is absorbed by the sample, and the transmit X-ray is converted and to visible light by a 50 μm LuAG scintillator. The visible light then goes through a 10 \times optical lens and is reflected by a mirror and captured by a PCO.Edge scientific CMOS camera¹⁶⁶.

In this study, the imaging energy was in the range of 8 keV to 22 keV depending on the contrast of the image for different samples. The beam current is 500 mA. The exposure time was 200ms for recording each projected image, and 1313 projections were taken by rotating the sample over 180°.

3.3.2 Samples fixture for X-ray tomography

The deposition of Ni-P on diamond abrasive is described in section 3.1. The coatings on different samples have varied plating time and ratios of reducing agent to nickel ion. Those samples are mounted in a way shown in Figure III.3, which can be easily installed on the sample stage by gluing.



Figure III.3. The configuration to examine the morphology of Ni-P coatings deposited on diamond abrasives.

A thin plastic tube was cut into several sections from one side to mount the coated diamond particles with a size of 400-600 μm . A small piece of transparent tape was inserted as section bottom. Then one coated diamond particle was dropped inside one section of the tube and glued at the position by the tape. Then the process was

repeated until all the sections are filled with one diamond particle, seen in Figure III.4. Then the tubes were wrapped around by tape and fixed in the lids of the vial containers with hot glue. Each tube contains 5 to 6 particles, and the X-ray scan of each particle can be conducted successively by adjusting the stage height slightly. This design makes the sample easy to carry and reduces the time needed to change samples and adjust the sample position.

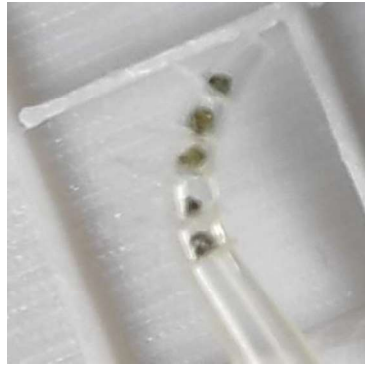


Figure III.4. Preparation of sample holder for coated diamond abrasives.

3.3.3 X-ray tomography image processing

The cross-section image datasets were reconstructed by Xi-CAM software. The resolution of the reconstructed cross-section image is $0.641\mu\text{m}$ per pixel for the abrasives in all three directions. The images generated by X-ray tomography were processed by 3D Slicer software version 4.10.2 to view the coatings in 3-dimension. Through the processed tomography images, both the inner and outer surfaces of the coatings can be reviewed from any angle. ImageJ software was also used for the dimension measurements for the topographies. Python codes were used to calculate the

thickness of the coating after the adjustment of the image direction and selection of the proper brightness value of the images.

3.4 Electrochemical characterization of coatings on diamond particles

3.4.1 Preparation of Ni-P coated abrasive electrodes

The working electrode should meet the following requirements so that suitable data reflecting the Ni-P coating condition can be obtained. The coating needs to be conductively connected to the potentiostat/galvanostat so that the current through the coating surface can be measured or controlled. Besides, the coating needs to have a large enough surface to ensure the accuracy of the current measurement.

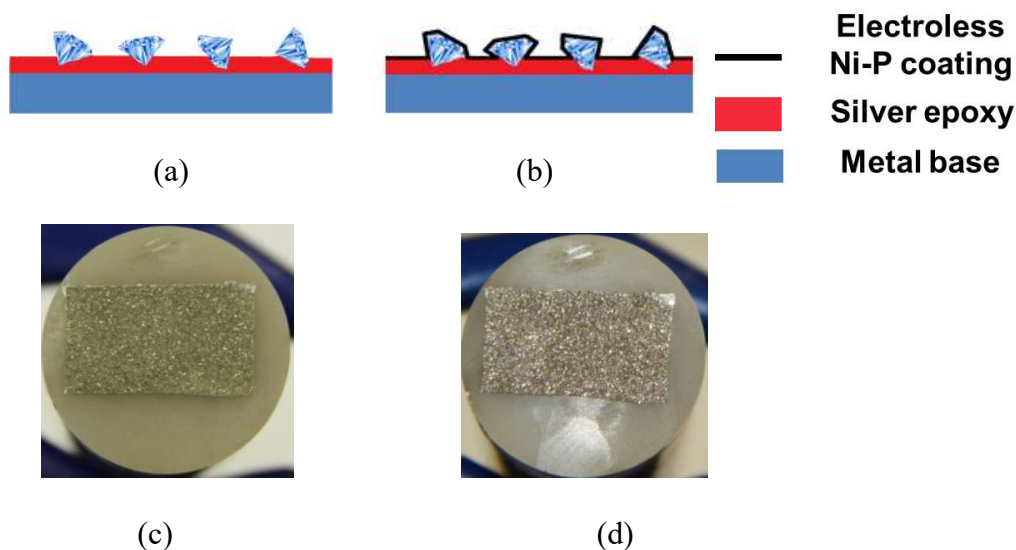


Figure III.5. (a) (b) Schematics and (c) (d) pictures of electrode preparation.

The following steps were taken to make the working electrode. First, a metal block threaded to the steel rod was encapsulated with epoxy, and only the end of the rod and the bottom surface of the metal base was exposed (the rectangular area in Figure

III.5(c) (d)). Then a conductive silver epoxy layer was applied to the exposed metal base surface, followed by sprinkling a thin layer of diamond powder onto the silver epoxy. A glass slide was used to press down slightly on the diamond grits to make sure they were securely fixed in the epoxy (Figure III.5 (a) (c)). After the epoxy is cured, blow away loose diamond particles and coat the bonded diamond with Ni-P alloy by electroless plating

Another working electrode with the coating on the nickel-metal substrate was also prepared. It is used for comparison in the durability test, which will be introduced later. This electrode was plated for 90 min to generate a thicker coating.

3.4.2 Corrosion potential, corrosion rate

The electrochemical properties of the synthesized coating are essential to its various applications such as corrosion protection layer and electrode or active material for catalytic reactions.

A three-electrode corrosion cell was used to evaluate the Ni-P coating. The working electrode is the Ni-P coating. The reference electrode used is a Ag/AgCl electrode. A Luggin probe with the tip close to the working electrode was used to minimize the potential drop due to solution resistance. A platinum foil is used as the counter electrode. A potentiostat/galvanostat was used to control the potential and measure the current of the cell or vice versa. The schematic of a three-electrode corrosion cell is shown in Figure III.6.

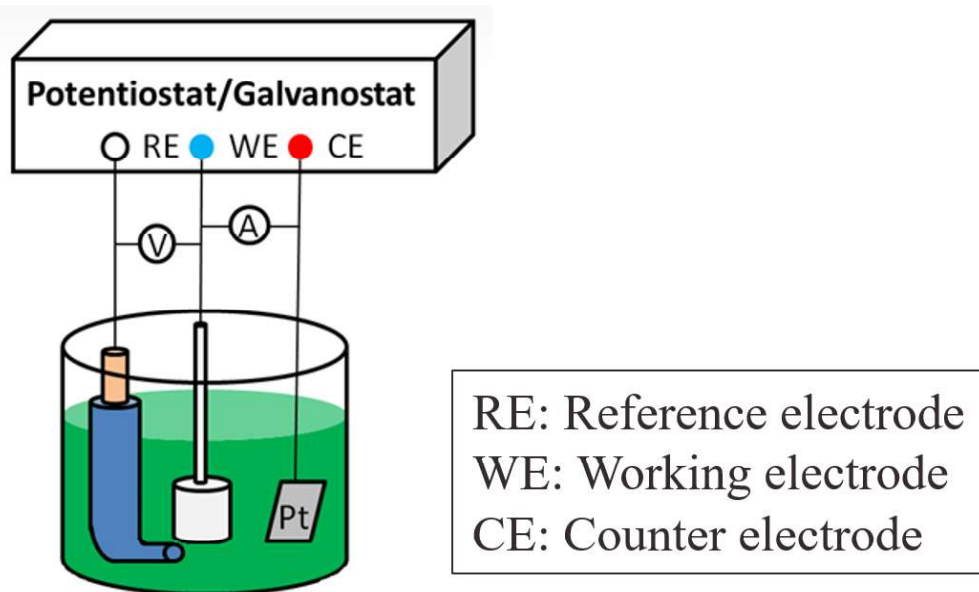


Figure III.6. Schematic of the three-electrode cell.

The electroplating solution was used as the electrolyte for the above corrosion cell. Because different manufacturers use different component concentrations for their process, two compositions) of plating baths are used: a low concentration bath (solution A) and a high concentration bath (solution B) (Table III-5). The electrolyte was heated to and maintained at 60°C. A cooling tube was used to minimize the electrolyte evaporation and to keep the reference electrode at room temperature. CorrWare software was used to program the Solartron Analytical 1287A potentiostat/galvanostat and obtain the data.

Potentiodynamic polarization experiments were conducted for the coating in both solutions. The electrode was immersed in the solution for 1 hour to achieve stable open circuit potential (OCP) before the polarization experiment. The potential was swept from -0.25V vs. OCP to +0.25V vs. E_{ref} at a rate of 0.1667mV/s, with the current measured at a rate of 1 s⁻¹.

Table III-5 Composition and pH value of the electrolyte

Chemicals	Solution A	Solution B
	Concentration (g/L)	Concentration (g/L)
Nickel sulfamate, Ni (SO ₃ NH ₂) ₂	60	300
Nickel chloride, NiCl ₂ .6H ₂ O	5	30
Boric acid, H ₃ BO ₃	13.33	30
pH value	5.1	4.0

3.4.3 Durability test

Then in the low concentration solution A, corrosion rate and open circuit potential were monitored to check the durability of the coating. For comparison, both the coating on diamond grits and the coating plated on nickel substrate were used for this monitoring. Three programs were run for 92 hours to obtain the linear polarization resistance, Tafel plot, and open circuit potential. In the first 20 hours, the linear polarization resistance was measured at the end of every 4th hour by varying the potential in the range of ± 15 mV vs. OCP. At the end of the 20th hour, a potentiodynamic polarization experiment was performed, with the potential swept from -0.2V vs. OCP to +0.2V vs. Ag/AgCl. After the potentiodynamic polarization test, the linear polarization resistance was measured every 12 hours to monitor the corrosion rate change with time. The potential scan rate and data recording rate are 0.1667 mV/s and 1 s⁻¹. For the rest of the time, open circuit potentials were measured with a data recording rate of 0.025 s⁻¹.

The electrochemical characterization applies polarized potential, thus introduces a current through the coating. So, it is a destructive test. But it mimics the possible current flow in a diamond-wire-tool manufacturing process through electroplating. For comparison, the immersion test, which involves no external current, was also performed. 0.9g electroless coated diamond grits were immersed in solution A at 60°C for seven days. The weights were measured before and after the immersion test with proper rinsing and drying steps. 0.9g uncoated diamond grits were also used for the immersion test to estimate the amount of weight loss during rinsing and drying operations.

3.4.4 Electrochemical test data processing

From the data obtained from the above experiments, the corrosion rate can be calculated by using the Tafel extrapolation, the Stern-Geary equation, and Faraday's law¹⁶⁷. In this paper, the corrosion rates are in the unit of cm/yr.

Tafel equation:

$$\eta = \beta \log \frac{i}{i_{corr}} \quad \text{III-1}$$

Stern-Geary equation:

$$i_{corr} = \frac{\beta_a \beta_c}{2.3(\beta_a + \beta_c)} \frac{1}{R_p} \quad \text{III-2}$$

The equation to calculate the corrosion rate:

$$\text{Corrosion rate (cm/yr)} = \frac{3.15 \times 10^7 \text{ s/yr} \times i_{corr} \times EW}{F \times \rho} \quad \text{III-3}$$

η : Overpotential ($E - OCP$), V ;

i : Corrosion current density, measured current divided by metal base surface area, A/cm^2 ;

β_a, β_c : Anodic, cathodic Tafel constant, *V/decade*;

R_p : Linear polarization resistance, $\Omega \cdot \text{cm}^2$;

F : Faraday's constant, 96,485, *coulombs/mole*;

EW : Equivalent weight, g/mol

ρ : density, g/cm³

CHAPTER IV
CORROSION RESISTANCE OF ELECTROLESS Ni-P COATING ON DIAMOND
PARTICLES³

This chapter will describe the compositional and microstructural features of electroless Ni-P coating. The corrosion resistance and the durability of the coatings characterized by a novel electrochemical monitoring method will also be demonstrated. The relationship between the microstructure and corrosion resistance of the coating will be discussed, and a coating failure mechanism is going to be proposed.

4.1 Morphology and composition of the coating

To check whether the coating surface was subjected to damage, before and after the electrochemical experiments and immersion test, samples were collected for morphology and composition characterization. The SEM images of the as-plated diamond grits (Figure IV.1(a)) show the diamond grits were fully coated with Ni-P coatings. A larger magnification image of the coating in the inset showed the coating layer was grown by aggregated nodules. The energy dispersive spectroscopy (EDS) indicates that the coating mainly consisted of nickel and phosphorus. The phosphorus composition in the Ni-P alloy was 11.6 wt.% in the as-plated coating. Figure IV.1 (b) shows the SEM images of the coated diamond grits after immersion in the low

³Part of this chapter is reprinted with permission from “Electrochemical Characterization of a Nickel-Phosphorus Coating on Diamond Grits” by Lian Ma, Xihua He, Alex Fang, and Hong Liang, *Materials Performance and Characterization* **2018**, 7(3), 266-280, Copyright [2018] by ASTM International.

concentration solution for seven days. No significant damage to the coating was seen. The composition analysis showed the phosphorus content is 9.6 wt.% in the Ni-P alloy. The weight of the immersed diamond grits decreased from 0.900g to 0.862g, while a control group of uncoated diamond showed a decrease of weight from 0.900g to 0.873g. The weight loss measurement of the powder, though involving errors during the rinsing and drying, indicated that there wasn't significant corrosion during the 7-day immersion. The morphology and composition analysis and the weight change all showed that the coating remained in good shape after 7-day immersion in the electroplating solution at 60°C.

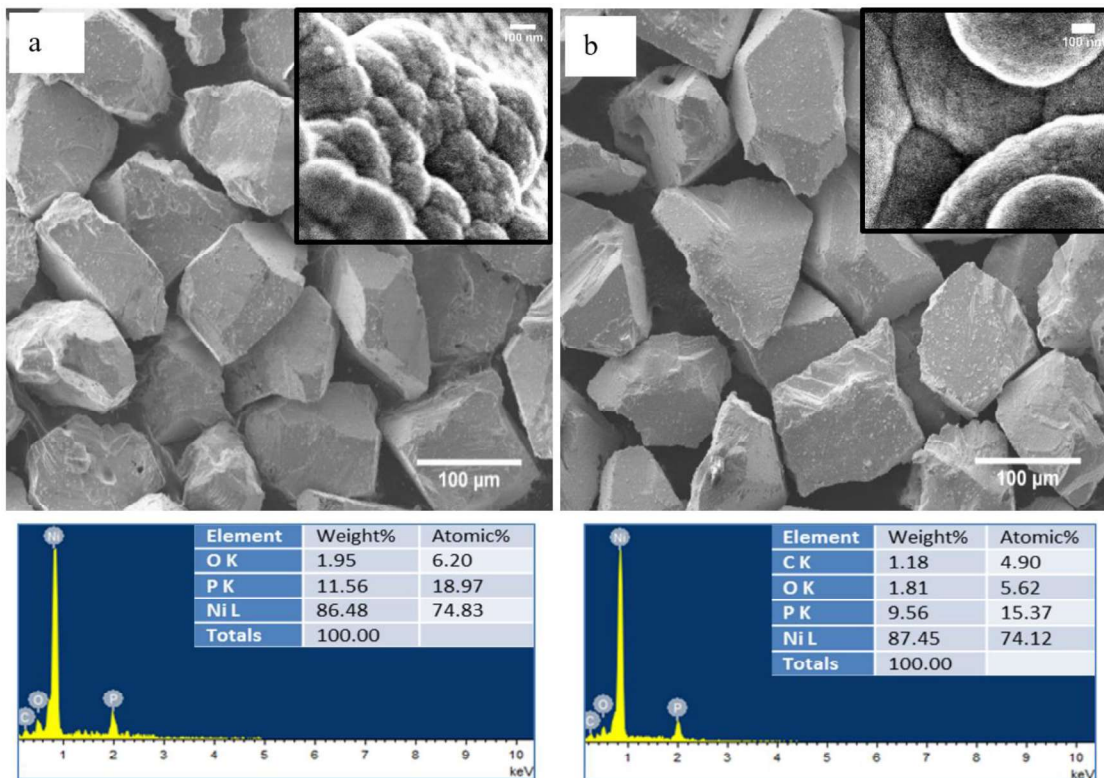
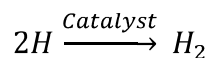
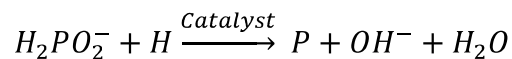
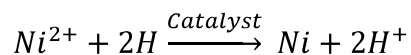
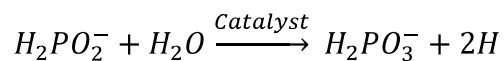


Figure IV.1. SEM image and EDS of (a) as-plated diamond grits and (b) coated diamond grits after immersion test.

The XRD pattern of the as-plated diamond grits and the uncoated diamond grits were shown in Figure IV.2. A broad peak(hump) at the base of the sharp diamond (111) peak indicates the amorphous structure of the Ni-P coating. It is the high phosphorus content in Ni-P alloy coating that causes the amorphous structure. And the amorphous structure has a high resistance to corrosion due to lack of grain boundaries ⁹¹. Several mechanisms of the bath reaction have been proposed since the first publication of electroless plating in 1946 ⁶². The atomic hydrogen mechanism is capable of explaining the hydrogen gas evolution and phosphorus content in the coating ¹⁶⁸.



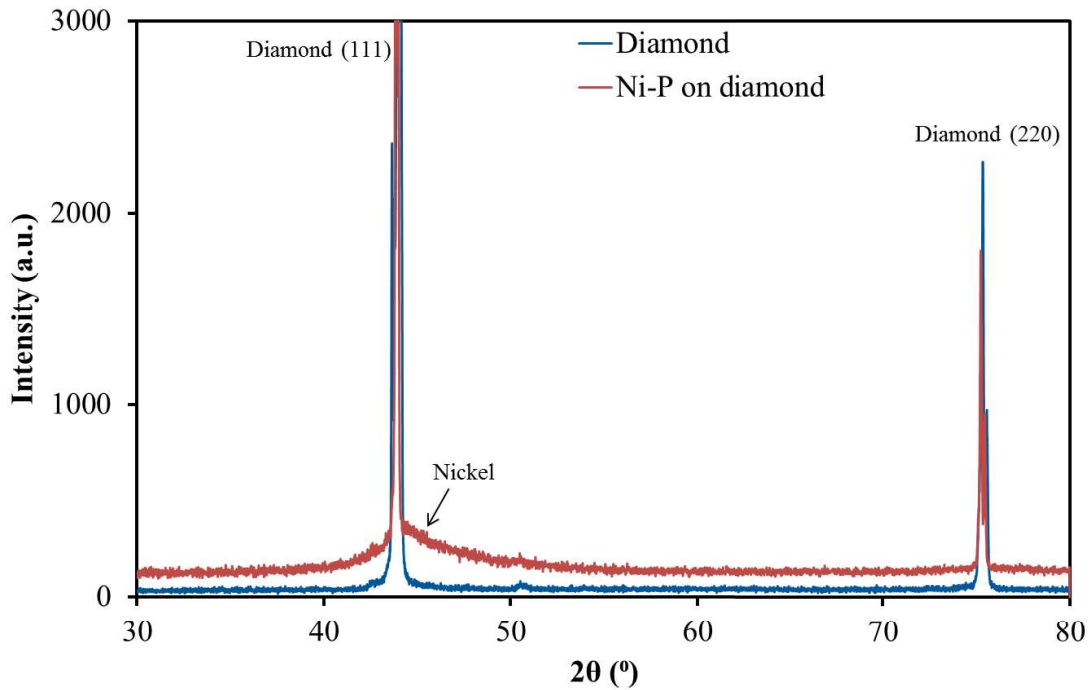


Figure IV.2. XRD patterns of as-plated coatings on diamond grits.

4.2 Corrosion resistance of the coatings

The polarization curves of the two samples tested in both low and high concentration plating solutions were shown in Figure IV.3. Both curves show the coating will passivate when the potential is around 0 V vs. Ag/AgCl. However, for the test in the high concentration bath, there is an additional passivation stage at -0.32 V vs. Ag/AgCl, and the trans-passivation occurred at -0.28 V vs. Ag/AgCl. These two stages of passivation indicated two passivation reactions that happened at their preferred potentials. The corrosion rates obtained from the Tafel extrapolation are shown in Table IV 1.

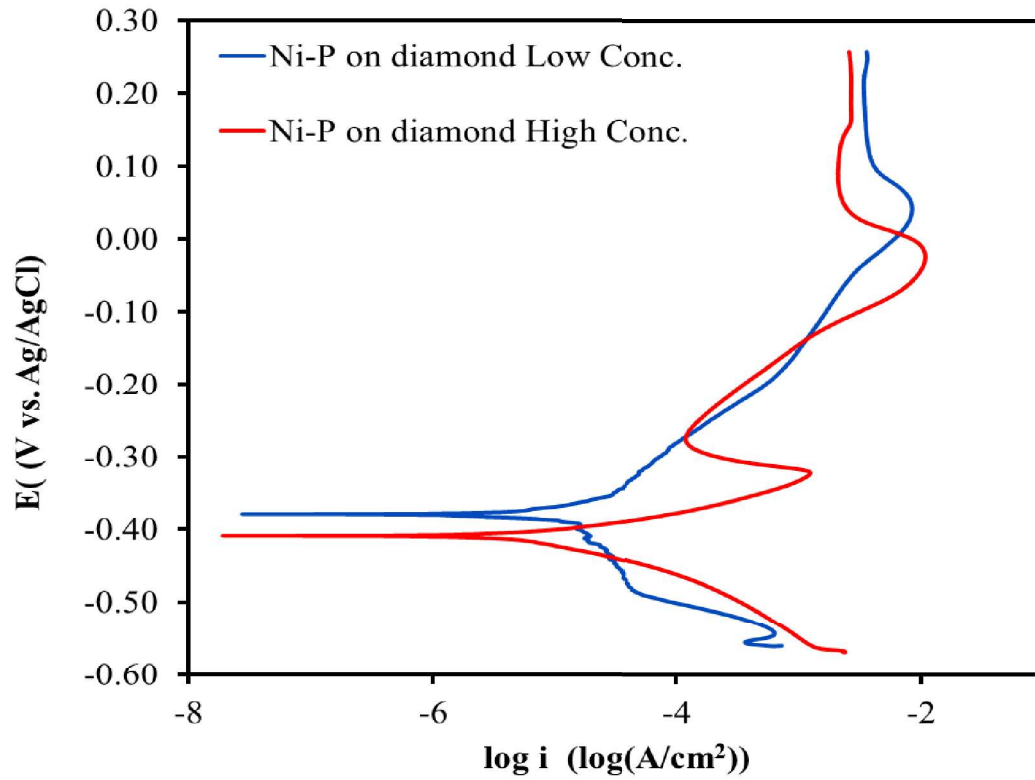


Figure IV.3. Polarization curves of Ni-P on the diamond in low and high concentration electroplating solutions

Table IV-1 Parameters obtained from the Tafel plot

Test curves	Ni-P on diamond particles in high conc. solution	Ni-P on diamond particles in low conc. solution	Ni-P on diamond particles 20hr in low conc. solution	Ni-P on Ni metal 20hr in low conc. solution
β_c/β_a (V/decade)	0.05/0.03	0.20/0.11	0.39/0.23	0.45/0.14
E_{corr} (V)	-0.41	-0.38	-0.11	-0.35
Corrosion current density i_{corr} ($\mu A/cm^2$)	7.9	14.1	34.5	35.5
Corrosion rate (cm/yr)	0.01	0.018	0.03	0.04
Maximum current density (A/dm^2)	1.09	0.85	0.18	2.18

The SEM images of the coatings on the diamond electrode before and after polarization experiments were shown in Figure IV.4. As seen in Figure IV.4(a), the as-plated electrode surface was entirely covered with the Ni-P alloy coating. This result was anticipated since one of the advantages of the electroless plating method is to generate uniform coatings on irregular surfaces¹⁶⁹. A larger magnification image of the coating surface on the right revealed that the surface is made up of small nodules with a distinguishable nodule size of 100-200nm. It is also seen that the surface contains some pinholes of 30-90nm in diameter. Figure IV.4(b) shows the coating after polarization experiments in a low concentration solution. Most of the coatings were ruptured, exposing the diamond substrate. The higher magnification image showed that the coating surface has lots more pinholes than the as-plated coating. Figure IV.4(c) shows the coating after polarization experiments in a high concentration bath. In this figure, except for several diamond grits, most of the diamond grits were still fully covered. The larger magnification image shows the surface was free from pinholes. The morphology showed that the coating is less susceptible to cracking in the high concentration solution.

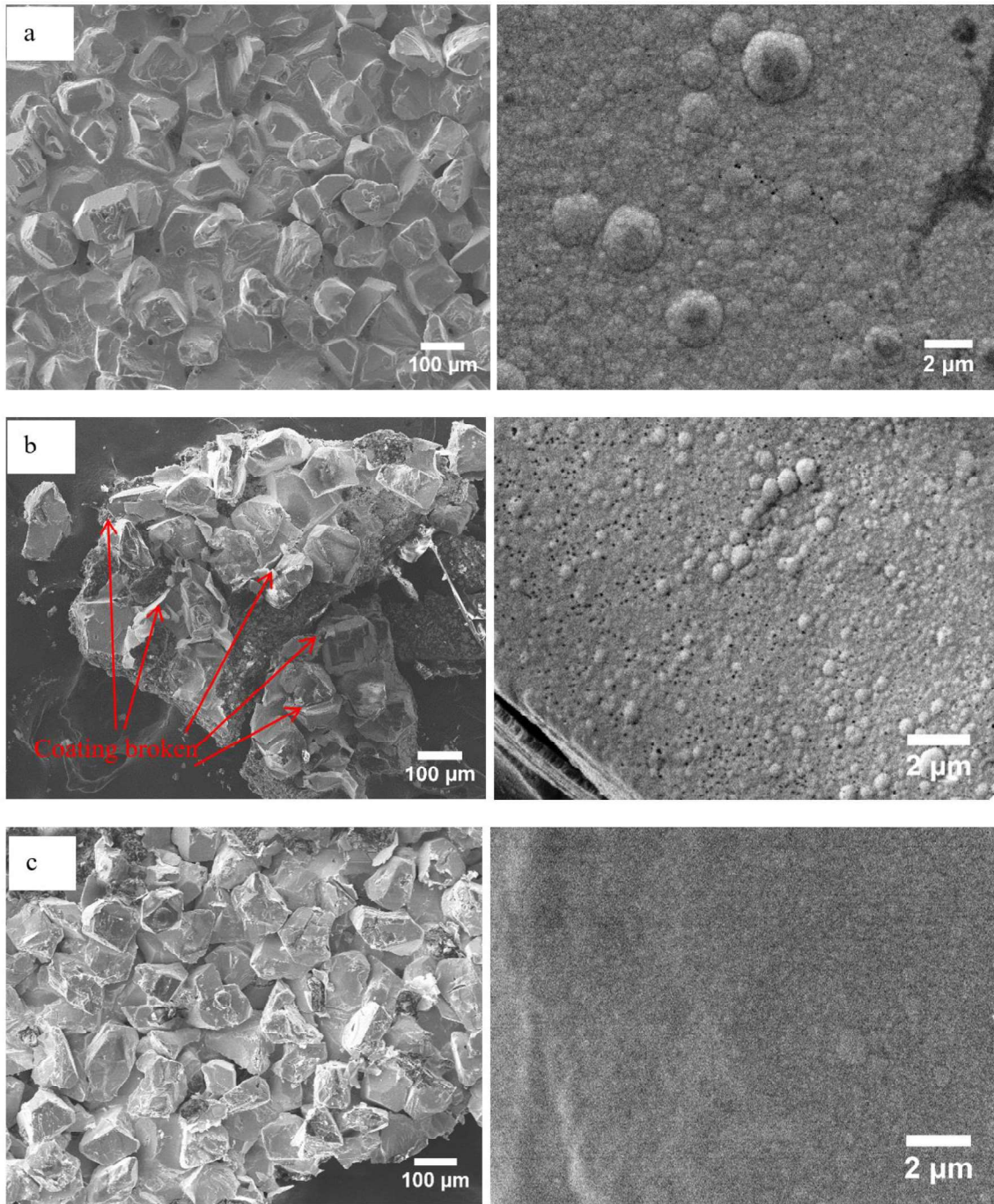


Figure IV.4. SEM image of Ni-P coating on diamond (a) as plated, after polarization examination in (b) low concentration electrolyte (c) high concentration electrolyte.

Combining the polarization curves and the SEM images, the different Ni-P coating performances in low and high concentration solutions can be described as follows. During the polarization experiment, the overpotential gradually increases to a more positive value, forcing the coating to lose electrons. In high concentration electrolyte, when the potential increase to $-0.32\text{ V vs. Ag/AgCl}$, the coating reacted with the electrolyte to generate a passive film, and therefore the current density decreased. When the potential continued to increase, the passive layer was broken down by the current, so the current density started to increase again. When the potential increased to $-0.02\text{V vs. Ag/AgCl}$, another passive layer was formed, and within the potential range in this experiment, this second passive layer didn't break down. While in the low concentration electrolyte, the passive layer didn't form until the potential reached 0.02V vs. Ag/AgCl . A large amount of nickel dissolved into the solution in this active corrosion stage before the passivation.

An SEM image of the cracked coating at the cross-section (Figure IV.5) indicted the cracked interface has a high density of pinholes, which almost go through the whole thickness of the coating. These pinholes were created by the hydrogen gas generated in the electroless plating process¹⁷⁰. The immersion test shows that the electrolyte only wouldn't damage the coating significantly, even for seven days' immersion. Hence, The current applied in the polarization process must play a vital role in the dissolution of the coating.

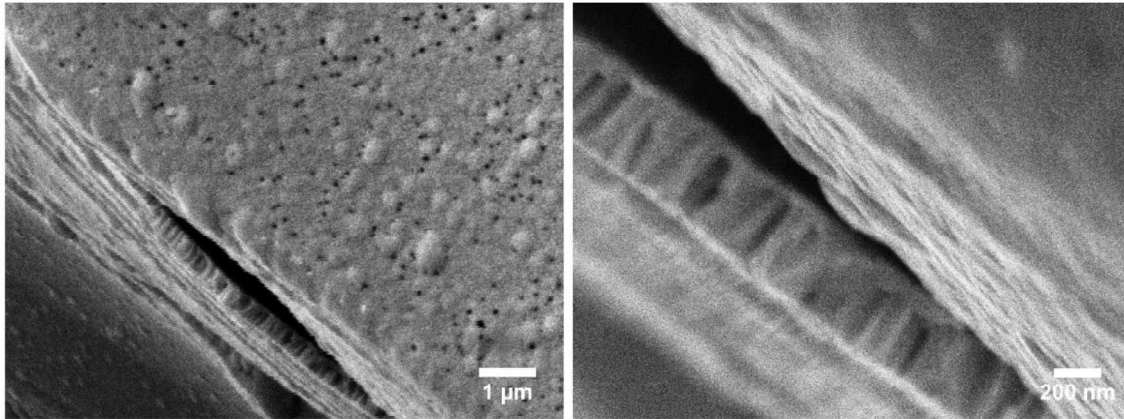


Figure IV.5. SEM image of Ni-P coating on the diamond after polarization examination in low concentration electroplating solutions from a ruptured coating location.

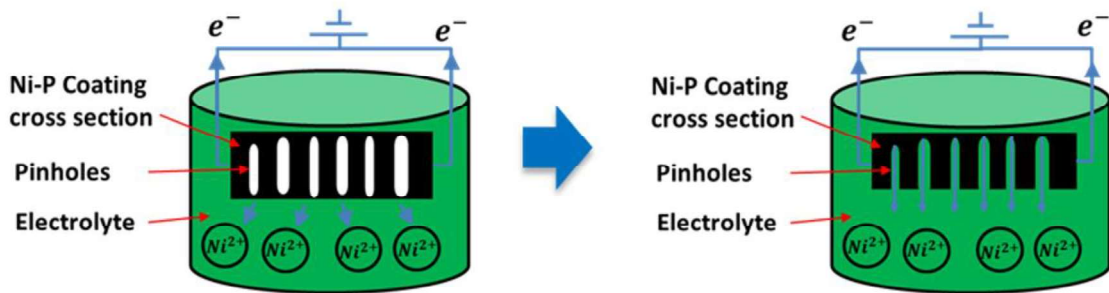


Figure IV.6. The current-assisted breakthrough of covered pinholes.

The coating failure mechanism is illustrated in Figure IV.6. The as-plated coating had pinholes imbedded. When the current passed through the coating, the dissolution of nickel will be enhanced, and those pinholes will be revealed. As more pinholes are exposed, the mechanical strength decreases significantly so that the residual stress in the coating will be big enough to cause coating cracking. After the coating fractured, the electrolyte can reach the interface and strip off the coating from the diamond surfaces.

The maximum current density occurred in the polarization test ($\sim 1\text{A}/\text{dm}^2$ in Table IV-1) is comparable with the current density used in the electroplating process, which is also in the order of $1\text{A}/\text{dm}^2$ ¹⁸. The current in the electroplating process will likely damage the coating if the plating solution is in a lower concentration.

4.3 Durability of coatings in an electroplating environment

The durability of the coating is exhibited by the plot of the open circuit potential versus exposure time, shown in Figure IV.7. Two samples were used, Ni-P coating on the diamond and Ni-P coating on Ni substrate, which was prepared as described in section 3.4.1. The coating on the nickel substrate was plated for a much longer time to generate a much thicker coating, which should be more durable in the electrolyte. The behaviors of these two coatings during these tests are compared below.

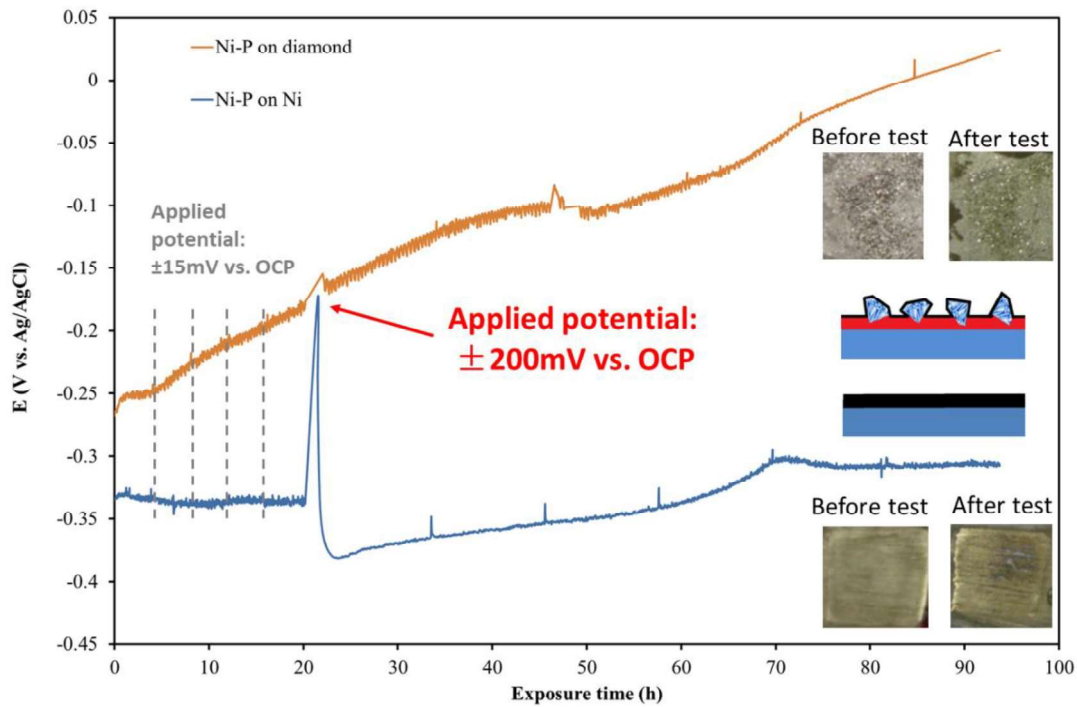


Figure IV.7. Open circuit potentials monitoring.

For the first 20 hours, the open circuit potential of the Ni-P coatings on nickel substrate remained stable at around $-0.33\text{V vs. Ag/AgCl}$. While for the coating on the diamond, after a stable stage ($-0.25\text{ V vs. Ag/AgCl}$) for about 4 hours, the open circuit potential of the coatings on diamond started to increase. Note that a small overpotential of $\pm 15\text{mV}$ was applied to measure the linear polarization resistance at the 4th hour. It is possible that the applied potential damaged the coating and exposed the nobler diamond substrate²¹. The current-assisted breakthrough of the pinholes, as discussed in the previous section, is the main reason for the coating cracking and detachment. Although this linear polarization resistance measurement is considered non-destructive to the thicker material, it is destructive for the thin coating with embedded pinholes.

In the 20th hour, the overpotential from -200 mV to 200 mV was applied to each of the samples with a scanning rate of 0.1667mV/s. The parameters obtained from this polarization are listed in Table IV-1.

After the polarization experiment, the OCP of the Ni-P on nickel started to increase, which means the coating was damaged by the supplied current. After 68 hours' immersion, the OCP became stable again, which indicated the passive layer was formed on the damaged surface. For the coating on diamond grits, the OCP kept increasing. The small spikes on the OCP curves are caused by the linear polarization resistance measurements.

The electrode surface before and after the durability test (insets of Figure IV.7) show that the coatings on the diamond grits are almost all lost. For the coating on the nickel substrate, the images after the durability test showed several cracks along the polishing direction, but most of the coating was still attached to the substrate. This difference is mainly because the coating-metal substrate bonding strength is much stronger than the strength of the physical bonding between the Ni-P coating and diamond substrate.

The corrosion rates of the two samples are also plotted against the exposure time in Figure IV.8. The trend of corrosion rate is in the opposite direction to that of open circuit potential. During the first 20 hours, the corrosion rates of Ni-P coatings on nickel changed very little, which corresponded to the stable OCP stage. For the coating on diamond grits, the corrosion rate started to decrease since the first measurement. Because the first linear polarization potential applied had already damaged the coating, and the cracked coating fell off the diamond surface readily due to poor adhesion, which caused the reduced area

of metal surface connected to the potentiostat. After the 12th hour, the corrosion rate becomes stable because all the coatings on diamond grits fell off the surface, and the metallic surface exposed to the electrolyte area became constant.

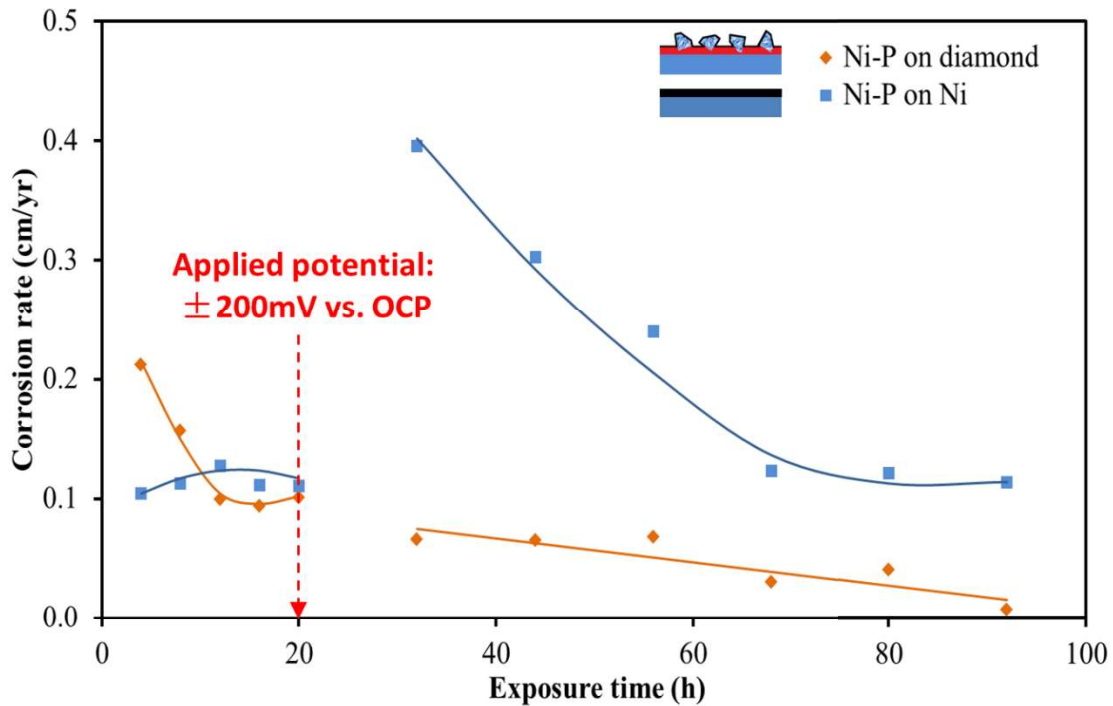


Figure IV.8. Corrosion rates monitoring.

After the polarization experiments at the 20th hour, the corrosion rate of the coating on a nickel substrate increased to about four times the value before the polarization. Then the corrosion rate started to decrease and became stable again after 68th hr. This trend corresponds to the OCP's change in Figure IV.7. The increase of the corrosion rate was caused by the increase of exposed surface to the electrolyte. The coating on the nickel substrate was still attached after slight damage due to a better adhesion to the substrate. Therefore, more surface area was created from the pitting and cracking. Besides, these

pittings and cracks promoted crevice corrosion, which further increases the corrosion rate. The followed decrease of the corrosion rate was due to the gradual passivation of the damaged surface. Finally, the passivation film built up became stable, so the corrosion rate stopped changing. After the 20th hr.'s polarization, this corrosion rate of coating on the diamond grits continued to decrease but at a slow speed. Since the picture of the coating on diamond grits showed all the coatings were gone after this durability test, this low corrosion rate should come from the silver epoxy and small patches of coating left on the silver epoxy.

So far, we have been able to identify two key factors in the coating degrading process. One is the current in the electroplating process, and the other one is the poor adhesion between the coating and the diamond substrate. Other potential factors like agitation in the electroplating process and high residual stress in the electroless plated coating may contribute to the coating failure. The agitation may introduce collision of coated particles, erosion of the electrolyte to the coating, or even cavitation. The undesirable residual stress makes the coating crack easily¹⁴². These aspects of the process need to be further studied in the future. How the synergy of those factors reduces the coating durability is an interesting topic to be further investigated.

4.4 Chapter summary of findings

To develop a better diamond tool with consistent performance, electroless plated Ni-P coating on diamond grits was investigated using an electrochemical method. With a new electrode made of Ni-P alloy coating on diamond grits, several electrochemical experiments were performed. Results led to the following conclusions.

The polarization experiments and morphology characterization revealed that the current plays a vital role in the coating degrading. In low concentration electrolyte (60g/L nickel sulfamate), a wide active corrosion stage exists before passivation. In this range, the current-assisted breakthrough of the pinholes causes the cracking and detachment of the coating. In high concentration solution (300g/L nickel sulfamate), the active corrosion stages are narrow, and two passivation stages existed. The combined effect of these two passivation stages protects the coating from peeling off.

The durability of the coating was successfully examined using open circuit potential (OCP) and linear polarization resistance (LPR) monitoring. The open-circuit potential shifted toward positive direction with time, suggesting the coating cracking and exposure of the nobler diamond substrate. The decrease in corrosion rate corresponds to the increase in open circuit potential further proved the decrease of coating surface area due to detachment. These results suggested that open circuit potential (OCP) and linear polarization resistance (LPR) monitoring over time give a good indication of coating conditions.

This study provides a methodology to examine the quality of electroless Ni-P coatings on abrasive diamond grits. This method can be applied to other metal coatings/powder substrate systems.

CHAPTER V
INFLUENCE OF PROCESSING PARAMETERS ON ELECTROLESS Ni-P
COATINGS ON DIAMOND PARTICLES

There are two challenges in electroless plating, the moving particles as substrate and the irregular morphologies of the same.

In this study, we successfully electrolessly deposited Ni-P coatings on diamond particles with a set of designed processing parameters. The deposited coatings were subsequently examined by optical microscopy, scanning electron microscopy, and X-ray computed tomography techniques to reveal the influence of the processing parameters on the coating growth.

In this chapter, the effects of plating time, substrate morphology, and the solution composition on coating coverage rate, coating morphology, and the deposition kinetics will be discussed.

5.1 Coating coverage rate

The coating coverage rate is an important indicator to evaluate the effectiveness of the coating process on diamond particles. A high coating coverage rate is expected to protect the diamond substrate from oxidation or graphitization in a machining process using a diamond-metal composite tool¹¹⁹. In the electroplating process to make diamond tools, a continuous coating on the diamond particle can prevent exposure of the interfaces to the electrolyte. Therefore, the corrosion and erosion attack of electrolyte is less likely to strip off the coating¹⁷¹. In this section, we are aiming to find out how the

various factors in the electroless plating process are influencing the coating coverage rate.

The coverage of a coating on the diamond particles can be observed from the optical images since the original diamond surface shows yellowish or greenish color. In contrast, the surface covered by coatings exhibits a shiny silver appearance. The correlation of the coverage rate with the initial reducing agent concentration and deposition time is evaluated. In Figure V.1, the optical images of the coated diamond particles are arranged with these two parameters. The row labeled Ni:P=1:1 presents the plating solution that initially composed of 0.1 mol/L NiSO₄ (same for all the solutions) and 0.1 mol/L NaH₂PO₂. During the deposition in each plating bath, diamond particles are sampled at six different deposition times: 5 min, 10 min, 20 min, 30 min, 60 min, and 180 min. And one diamond particle that represents the majority of sampled particles was selected for optical and micro-CT imaging. Two optical images of the selected particle from two different angles are displayed in Figure V.1. The optical images of the Ni:P=1:1-20 min and 30 min samples are missing because of a mistake in sample handling.

Ni:P	5min	10min	20min	30min	60min	180min
1:1						
1:2						
1:3						
1:4						

 500 μm

Figure V.1. Optical images of coatings on diamond particles.

5.1.1 Factors influencing coating coverage rate

Three factors were observed to influence the coating coverage rate according to the optical images of coated diamond particles displayed in Figure V.1. They are deposition time, substrate morphology, and reducing agent concentration. This section discusses the principles regarding how they affect the coverage.

5.1.1.1 Deposition time

Each row in Figure V.1 manifests the evolution of coating coverage against time for a given plating solution. The coating coverage rate increases with deposition time for the Ni:P=1:1, Ni:P=1:3, and Ni:P=1:4 solutions. For the Ni:P=1:1 and Ni:P=1:3 rows, for short plating times, i.e., 5 min and 10 min, the coatings only cover few diamond faces. As the deposition time increases, more faces of the diamond particles are covered with coatings, the Ni:P=1:3-60 min sample among these two rows reach full coverage. For the row labeled Ni:P=1:4, even short deposition times result in a high coating coverage rate in the 5 min and 10 min samples leaving only one or two faces uncovered. For deposition time longer than 20 min, the diamond particles are fully covered with coatings. Compared to other plating solutions, the diamond particles plated in the Ni:P=1:2 solution do not show an apparent increasing trend of coating coverage rate because almost all the samples show full coating coverage.

In addition to better coating coverage, longer deposition time also results in more fractures, deflections or curling of the coatings, as shown in Ni:P=1:1-60min, 180min, Ni:P=1:2-60min, 180 min, Ni:P=1:3-30 min and 60 min and Ni:P=1:4-10 min to 180 min samples. These defects are due to the stress build up in the coating during the

deposition process. Once these defects appear, the hydrogen bubbles agitated solution can cause the coatings to detach from diamond surfaces, which reduce the coating coverage rate.

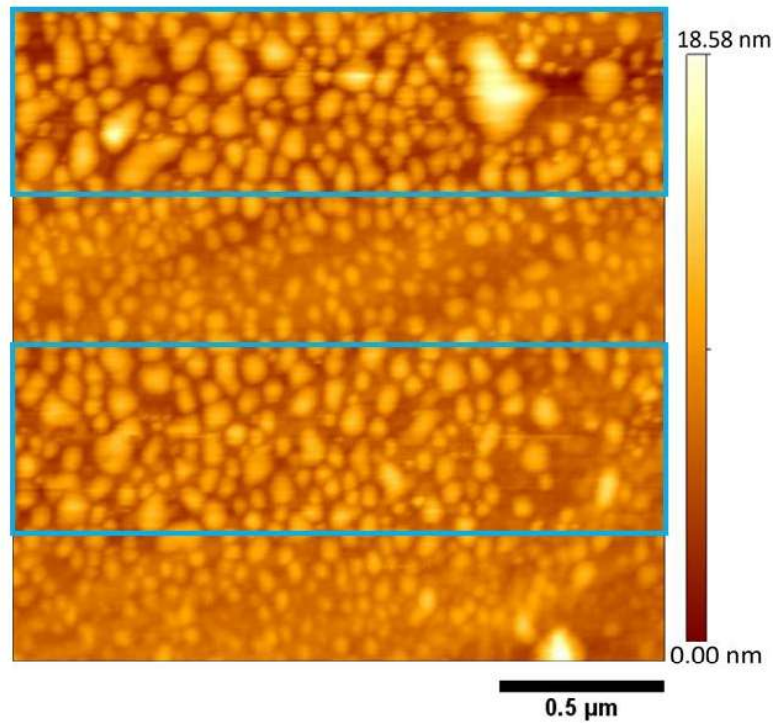
The above observations lead to the conclusion that the coating coverage rate depends on the synergistic effect of the coating deposition and detachment. The uncovered parts of the diamond particles were either because the coating has not yet formed due to short plating time or the coating fractured and detached from the diamond surfaces. As the deposition time increases, the coating grows to cover more substrate surfaces. While at the same time, the detaching of the coating starts to take place, which exposes the bare diamond surface to the solution. If the coatings detach right before the end of plating, the bare diamond surface is exposed. If the diamond remains in the plating solution for some time after the coating detachment, new coatings will be deposited on the surface again.

5.1.1.2 Substrate morphology

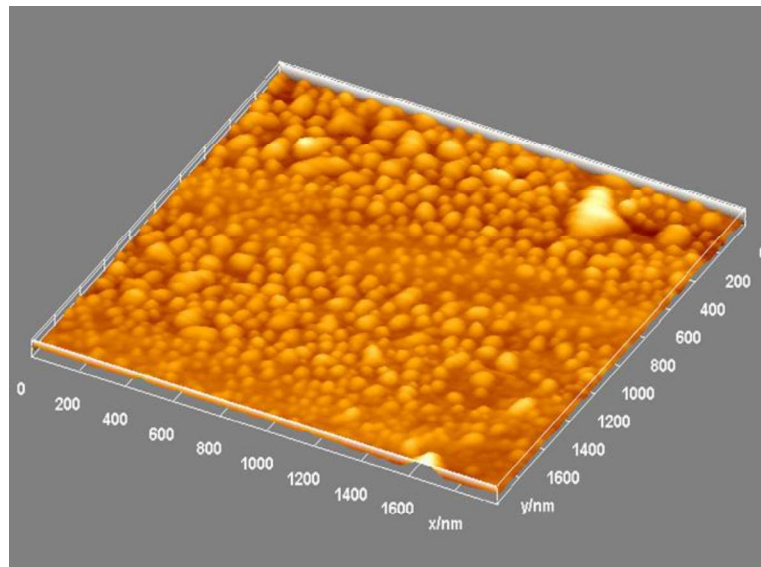
The coating coverage shows a strong dependence on the substrate morphology. For short deposition times (Ni:P=1:1- 5 min and 10 min, and Ni:P=1:3-5min and 10 min in Figure V.1), among the surfaces covered with coatings, the rough surface shows good coating adherence, while the flat and smooth surfaces exhibit deflection and curling at the edges of the coatings. For longer deposition times, all the uncovered surfaces are flat and smooth (Ni:P=1:1- 60 min and 180 min, Ni:P=1:2-60min, Ni:P=1:3-20 min, 30 min, and 180 min, and Ni:P=1:4-5min and 10 min in Figure V.1).

The substrate morphology affects the coating coverage in two aspects. First, the deposition of coatings begins earlier on rough surfaces. Second, coatings are generated on the rough surfaces are not easy to detach from the surfaces. The origin of the second aspect will be discussed in coating failure mechanisms in Chapter VI. In this chapter, the substrate surface morphology's influence on the initiation of coating deposition will be analyzed.

The initiation of coating growth relies on the existence of catalysts. The diamond surface after pretreatment was scanned with atomic force microscopy (AFM). The height image is shown in Figure V.2(a); the bright color indicates a higher height; the dark color indicates a lower height. The brighter particles in Figure V.2 are the palladium clusters for catalyzing the electroless deposition. To better visualize the particle distribution, a 3D rendered image is shown in Figure V.2(b). From Figure V.2, it is observed that the particles sizes are not evenly distributed but vary with the substrate height. Inside the blue boxes in Figure V.2(a), the background is darker red, meaning the substrate surface is shallower. The clusters sizes distributions inside and outside the blue boxes were analyzed respectively using ImageJ software, and results are shown in Figure V.3. The average size of catalyst clusters inside the blue boxes is 58 nm, while the value outside the blue boxes is 43 nm. Therefore, we can conclude that the lower altitude surface tends to have larger catalyst clusters after the pretreatment.



(a)



(b)

Figure V.2. AFM (a) height image and (b) 3D image of palladium clusters on the diamond surface.

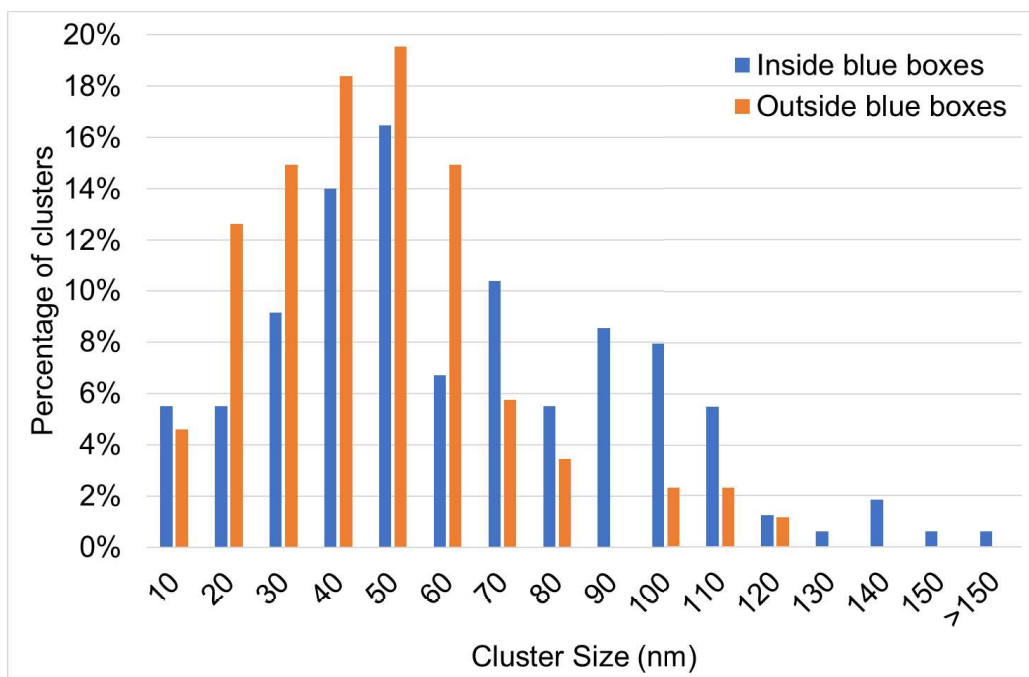


Figure V.3. Catalyst cluster size distribution on shallower and higher substrate surfaces. The blue boxes are drawn in Figure V.2 (a) to demonstrate the shallower substrate surface.

The distribution of catalyst clusters gives a clue of how the substrate morphology affects the initiation of coating deposition. For rough substrate surfaces, there are lots of upper and lower regions so that large catalyst clusters are present. The existence of these large catalyst clusters, which stick out of the average surface in the deposition solution, accelerate the mass transfer, and initiate the coating deposition at those locations.

5.1.1.3 Concentration of reducing agent

Here we discuss about effects of the concentration of reducing agent. From Figure V.1, the coating coverage rate for short plating times (5 min and 10 min) first increases with the reducing agent concentration (from Ni:P=1:1 to Ni:P=1:2), and then decreases in

the Ni:P=1:3 samples and increases again(Ni:P=1:4). This changing trend is mainly because the reducing agent concentration influences the coating morphology in two ways. First, with a higher concentration of the reducing agent (sodium hypophosphite), the deposition rate is faster, so the coating coverage rate increases. However, the higher concentration of reducing agents causes the plating process to be more violent, in which the produced hydrogen gas heavily agitates the solution. This agitation causes the diamond particles to move more vigorously, and collisions of the particles with each other may happen. Besides, the turbulent flow around the particle may introduce local cavitation on the coating surface. Both particle-particle collision and fluid erosion increase the probability of the coating fracture.

5.1.2 Process optimization

The above mentioned three factors are working together to influence the coating coverage rate on diamond particles. The diamond surfaces with more irregularities tend to have larger catalyst clusters and therefore are deposited with the coating first. During the deposition, the release of hydrogen bubbles from the coating surface agitates the solution. It causes the weakly bonded coating to detach from the diamond surface, which leads to a reduction in the coating coverage rate. The deposition process can continue on the exposed diamond surface after coating peeling off, given enough time for this process. Therefore, the coverage rate of coating on a randomly shaped diamond particle depends on the timing of both the deposition and detaching process, both of which are dynamic and influenced by the synergistic effect of the deposition time, substrate morphology and reducing agent concentration.

In this study, Ni:P=1:2 solution has the best coverage rate for the deposition time from 5 min to 30 min. When increasing the deposition time or increase the reducing agent concentration, the coatings all see more fracture and deflection or curling sites. Although plating for an extremely long time can provide full coverage, they are economically less efficient because it wastes metal and is more time-consuming. Therefore, while keeping all the other plating parameters the same (chemical concentrations, plating temperature: 70°C, pH=9), the recommended reducing agent concentration is 0.2 mol/L and deposition time is between 5 min and 30 min.

5.2 Coating morphology

The electroless deposition can create coatings of various surface morphologies depending on the deposition conditions. The coating generated in the electroless deposition is smoother and more uniform in thickness compared to electroplated coatings¹⁶⁹. But sometimes the coatings exhibit nodular morphology which consists of semi-spheres protruding from the coating surface^{172, 173}.

Different morphological features of the coatings are desired for different applications. For machining tools used in processes that require high dimensional accuracy, such as a single-layered abrasive wheel, smooth coatings with uniform thickness on abrasive particles are desired^{118, 172, 174}. The nodular coating morphology is better for making the particle reinforced composite, because it increases the contact surface area with the matrix, thus prevents abrasive grits from pullout^{124, 127, 175}.

The morphology can be adjusted through the deposition parameters, such as the deposition time, the reducing agent concentration, pH values, and additives^{175, 176}. But a systematic investigation on how these parameters affect the morphology is still lacking.

In this study, the surface morphology of the coatings electrolessly deposited on diamond particles is analyzed based on the optical images, SEM images, and 3D rendered micro-CT images among various imaging techniques. The correlation between the morphology and the deposition parameters is discussed to find the most suitable deposition condition for the required morphology.

5.2.1 Factors influencing coating morphology

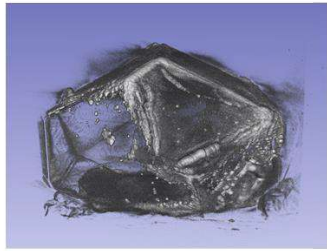
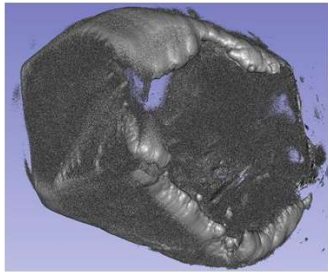


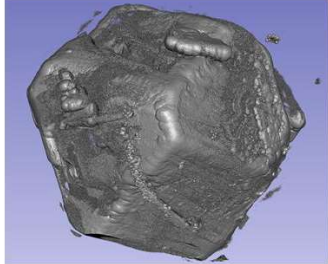
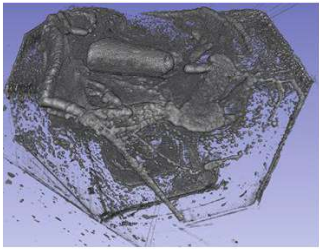
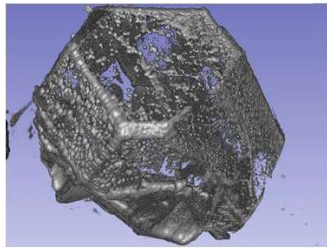

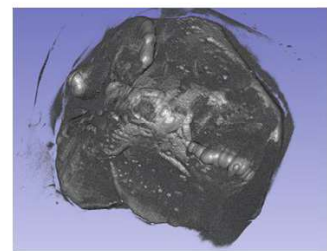
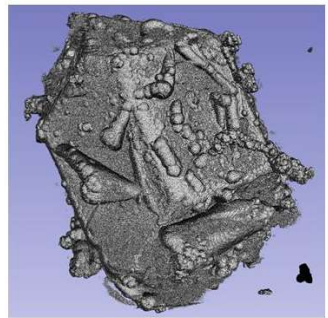
There are three factors found to affect the coating's morphology: deposition parameters, coating integrity, and substrate morphology.

5.2.1.1 Deposition parameters

Two deposition parameters are studied in this research: deposition time and the reducing agent concentration. From the optical images in Figure V.1, it is found that the coatings plated for short times all exhibit a shinier surface than longer plated coatings. The glossiness of the coating in the optical images can tell whether a coating surface is smooth or rough. A smooth coating reflects light in a mirror-like direction hence exhibit a shiny appearance. While a rough coating looks dull because the light goes through diffuse reflection. Therefore, albeit having a low resolution, the optical images still demonstrate that longer plating time renders the rougher coating surface. For some of the samples deposited for 60 min and 180 min, not only the coatings are dull, but also the nodules become big enough to see directly in these images.

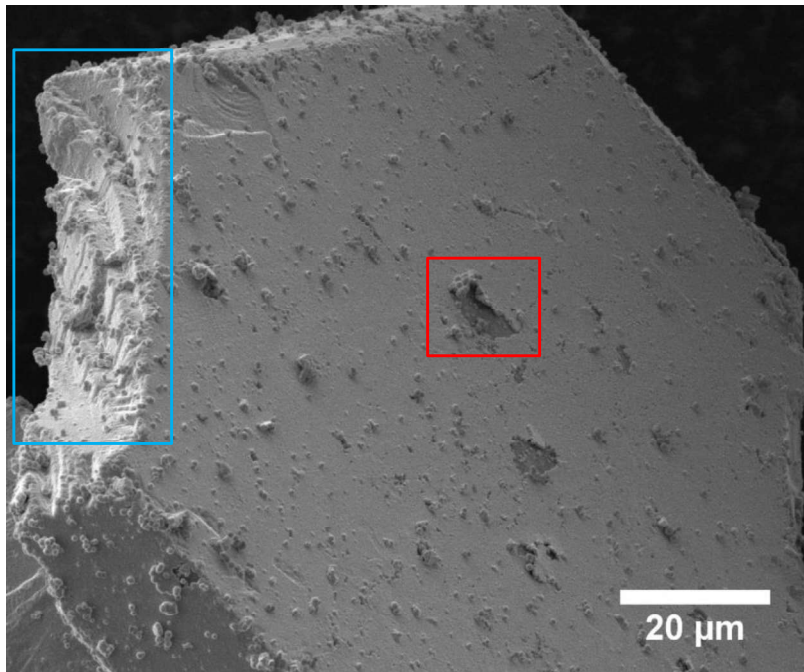
The 3D rendering of the micro-CT scanned data was performed to view the coating morphology with a wide range of magnifications and from various angles. Since the 3D rendered images with thinner coating contain too much noise, only the samples with deposition time equal to or longer than 30 mins are analyzed. The views from selected angles of the 3D images are shown in Figure V.4. The images of samples plated in the Ni:P=1:3 and Ni:P=1:4 solutions in Figure V.4 clearly show that the size of nodules increases with deposition time. From Figure V.4, it is also found that higher reducing agent concentration produces a rougher coating surface compared to that deposited in a lower concentration solution for the same deposition time.

To understand how the morphology is influenced by the deposition parameters, we need to understand the coating nucleation and growth process in an electroless deposition. When a substrate is immersed in the plating bath, the palladium clusters on the surfaces will catalyze the reduction of nickel ions at discrete nucleation sites. The nickel atoms precipitate around the nucleation sites and merge to form hemispheres for lowering surface energy. As the deposition continues, these hemispherical deposits grow bigger until they meet their neighbors and merge into a continuous film¹⁷⁷. This process is evidenced by the SEM images of a coating in Figure V.5, where a smooth electroless Ni-P coating is shown made up of small spheres which merged into each other. The relatively dense and uniformly distributed nucleation sites grow into the same small sizes before merging, thus generate coating with a smooth surface, as shown in Figure V.6(a). If the nucleation sites are loosely distributed, they will grow larger before merging, so the film formed will be rough, as demonstrated by Figure V.6(b).

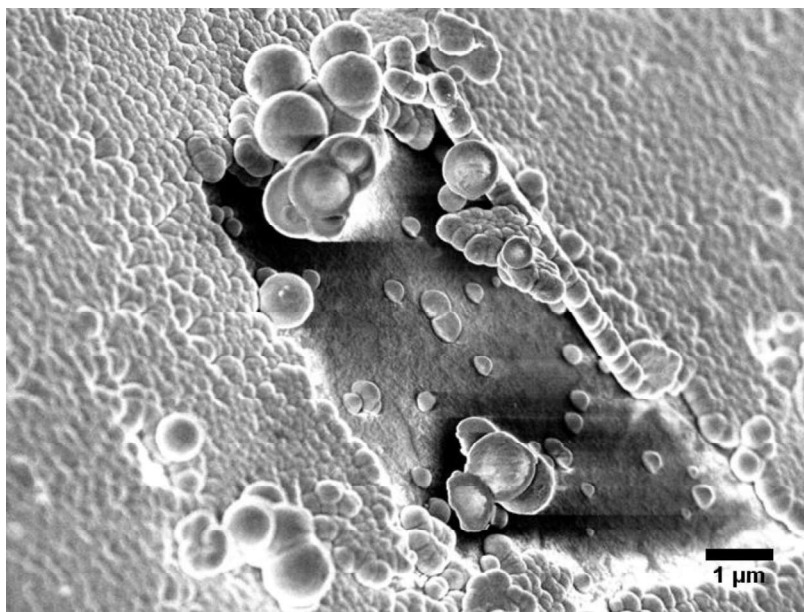
Ni:P	30min	60min	180min
1:1			
1:2			
1:3			
1:4			


500 μm

Figure V.4. Volume rendered images of coated diamond particles showing nodules on the surface.

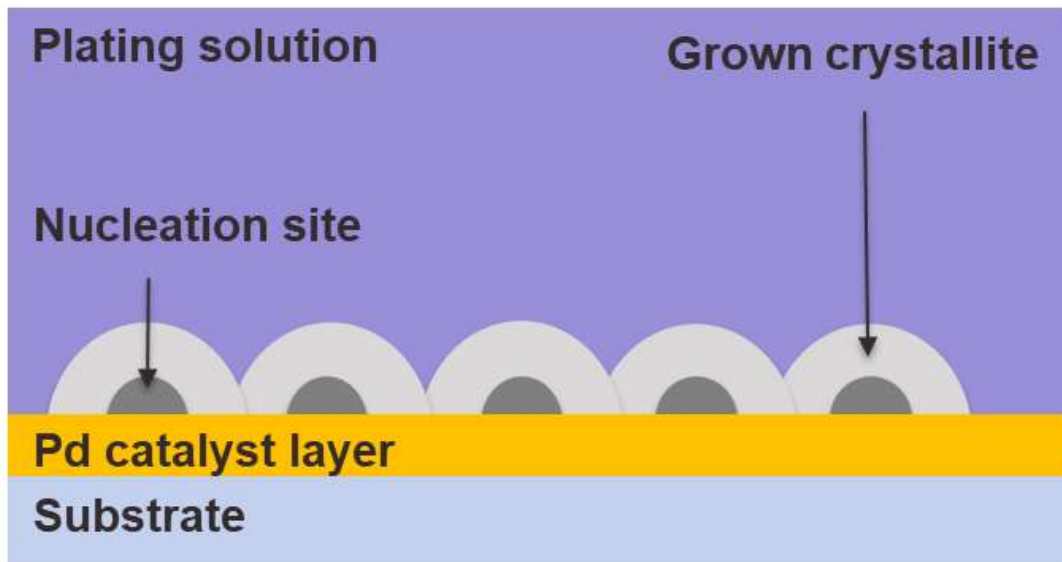


(a)

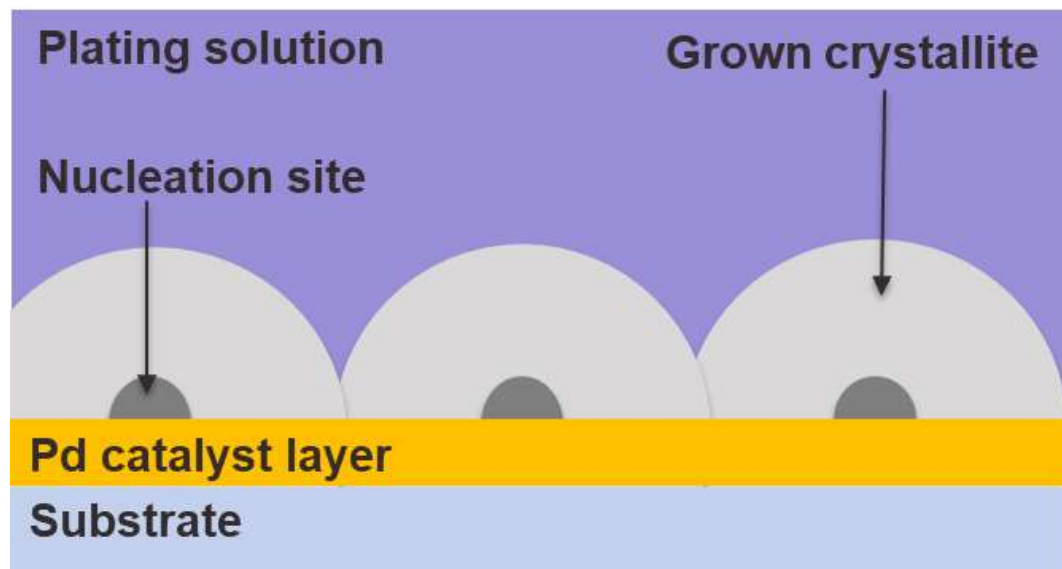


(b)

Figure V.5. The SEM images of (a) a coated diamond showing the nodules at different locations. (b) high magnification image of the red box area in (a).



(a)



(b)

Figure V.6. Sketches illustrate the formation process of coating with (a) uniformly and densely distributed nucleation sites, (b) uniformly but loosely distributed nucleation sites.

The nuclei density depends on the catalyst type and distribution, and the concentration of reactants in the plating solution. Figure V.2 shows that the palladium catalyst clusters almost cover the entire diamond surfaces after pretreatment, which means the entire diamond surface can catalyze the reduction reaction. The reactants concentration determines the Gibbs free energy change (ΔG) of the reduction reaction, which is the driving force of the deposition. At the beginning of the deposition, the concentrations of reactants are high, so the driving force is high. Therefore, a large number of embryos can overcome the energy barrier caused by the increase of surface energy and form stable nuclei. This high nucleation density results in a smooth, shiny surface by the naked eye. After the first continuous coating is formed, the surface is fully covered with Ni-P alloy, which has a lower catalytic activity than palladium. And after deposition for a while, the solution concentration is reduced. Both of the changes, in catalyst type and reactant concentration, result in a lower nucleation density and hence rougher coating surface. This phenomenon is manifested in Ni:P=1:4-30min and 60 min samples in Figure V.4

Figure V.4, where some discrete hemispherical nodules are on top of a smooth layer of coatings.

5.2.1.2 Coating integrity

The quality of the coating influences the formation of nodular morphology. From the Ni:P=1:1-60 min and 180 min, Ni:P=1:2-60 min and 180 min, Ni:P=1:4-180min samples in Figure V.4, nodular morphology is seen on the edges of the fractured coatings. During a deposition, the coating fracture is usually accompanied by coating deflection, which causes the fractured edges to detach from the diamond surfaces. After

the edge detaches, the continued coating growth from the edge is catalyzed by the Ni-P. And the fracture occurs after the first continuous film is formed when the concentration of the solution becomes lower. So low nucleation density leads to the nodular morphology formation at the fractured coating edges as well.

The coating at the fractured edge is also thicker because the fractured coating edge is surrounded by the plating solutions in three directions (above the coating, below the coating and side of the coating edge). So the supply of the reactants to the edge of a coating is easier.

This edge type of nodular morphology is not desirable since the newly grown coating is not touching the diamond surface, hence there is no or little adhesion force. Besides, this dangling piece of coating will be easily knocked off the substrate by collisions or fluid drag during the deposition process.

When a cracked coating peels off the substrate surface, nodular morphology tends to form on the original substrate surface. This was observed in the Ni:P=1:3-30 min and 60 min samples in Figure V.4, which show both continuous smooth coatings and separate nodules. As discussed in the coating coverage section (section 5.1.1), the coatings formed in this solution have lots of fractures and peeling-offs. The continuous smooth coatings are formed by the coalescences of deposits around the high-density nuclei formed at an early stage of the deposition. The nodular morphology is formed after the initial coating has peeled off. After the coating failure, which exposes the underlying diamond surfaces to the plating bath, new nucleation sites with lower density will be formed. The lower nucleation density is due to the lower concentration of the

reactants. Due to the discontinuity of this nodular deposits, this kind of morphology is not desired, because it cannot provide full coverage and protection for the diamond substrate.

5.2.1.3 Substrate morphology

The surface morphology of a substrate affects the nodular morphology with a different mechanism. Ideally, the nucleation only took place on the diamond substrates. However, when impurities appear in the solution, nucleation in the solution occurs. The growth of the nuclei in the solution creates spherical deposits, and when such spheres encounter a diamond particle, they have a chance to attach to the diamond surface. If the deposition reaction occurs near the interface between the attached spheres and the coating, the attached spheres will be “welded” to the coating. The chance of these spheres to settle down is high when the encountered surface is concave. The evidence of this behavior is shown in Figure V.5(a) within the blue boxes, where a large number of the spherical particles aggregate on the rugged surface. The nodules created in this manner can be somewhere between a whole sphere and a hemisphere. This process results in the spherical nodular morphology in the Ni:P=1:2-30 min and Ni:P=1:4-180 min samples in Figure V.4.

We can add some impurities or increase the concentration of the reactants to promote the nodular morphology formed in this mechanism. However, if the parameters are not controllable, solution decomposition may occur, which means most deposits are in powder form, and very little deposit is formed on the diamond surface.

5.2.2 Process suggestions

Four kinds of nodular morphologies are found on the electrolessly deposited coatings on diamond particles. They are on top of a uniform coating, on the edge of a fractured coating, on the surface from which a previous coating is detached, and on a rough substrate surface. The mechanisms of the nodular morphology formation are either due to a lower nucleation density on the substrate or high nucleation rate in the solution. Understanding this, we can provide the process suggestions for desired morphology.

The measures to ensure a smooth and uniform coating include low coating thickness, good coating integrity, and flat substrate morphology. On the other hand, if a coating with nodular morphology is required, a rough substrate and a thicker coating should be used. However, any causes to introduce coating failure should still be avoided because even though coating fracture may help form nodular morphology, it may also render partial or complete coating loss.

5.3 Deposition kinetics

The kinetics of electroless deposition provides a guideline to choose the solution compositions and operation parameters for the desired thickness. Many factors are affecting the deposition kinetics. In this study, we discuss the influence of crystallographic orientation and reactants concentrations.

5.3.1 Influence of crystallographic orientation

The thickness of the coatings on diamond surfaces with different crystallographic orientations was obtained from the tomographic images for the Ni:P=1:2-10 min sample.

This specific sample is investigated since it has integral coatings on all of the faces. The 14 faces on this diamond particle are numbered 1 to 14, as shown in Figure V.7. They can be divided into two categories: six (100) faces and eight (111) faces, among which four (100) faces and eight (111) are with clear pixel information to be discussed here. The thickness distribution of each face is obtained using a python code, which is attached in the appendix. Only the thickness of the smooth part of each face is processed so that the noises on the rough surface are eliminated. The obtained thickness distributions are shown in Figure V.8. The rectangular surfaces in the first column are (100) faces, and the hexagonal or triangular surfaces in the second and third columns are the (111) faces. The thickness of the edges was also obtained.

The coating thickness is represented by the color indicated by the color bar: the blue color means a lesser thickness, and the red color indicates a greater thickness. There is non-uniformity observed on the coating thickness obtained from tomography images, as shown in Figure V.8. This non-uniformity is due to beam hardening and X-ray scattering, which makes the coating look thicker near the edges and thinner near the center. The non-uniformity was excluded by using the average thickness value for each face. The results show that the coatings are uniform in the coating thickness on diamond surfaces regardless of the crystallographic orientations. The edges have less scattering effect so that the differences between the maximum and average thickness are small.

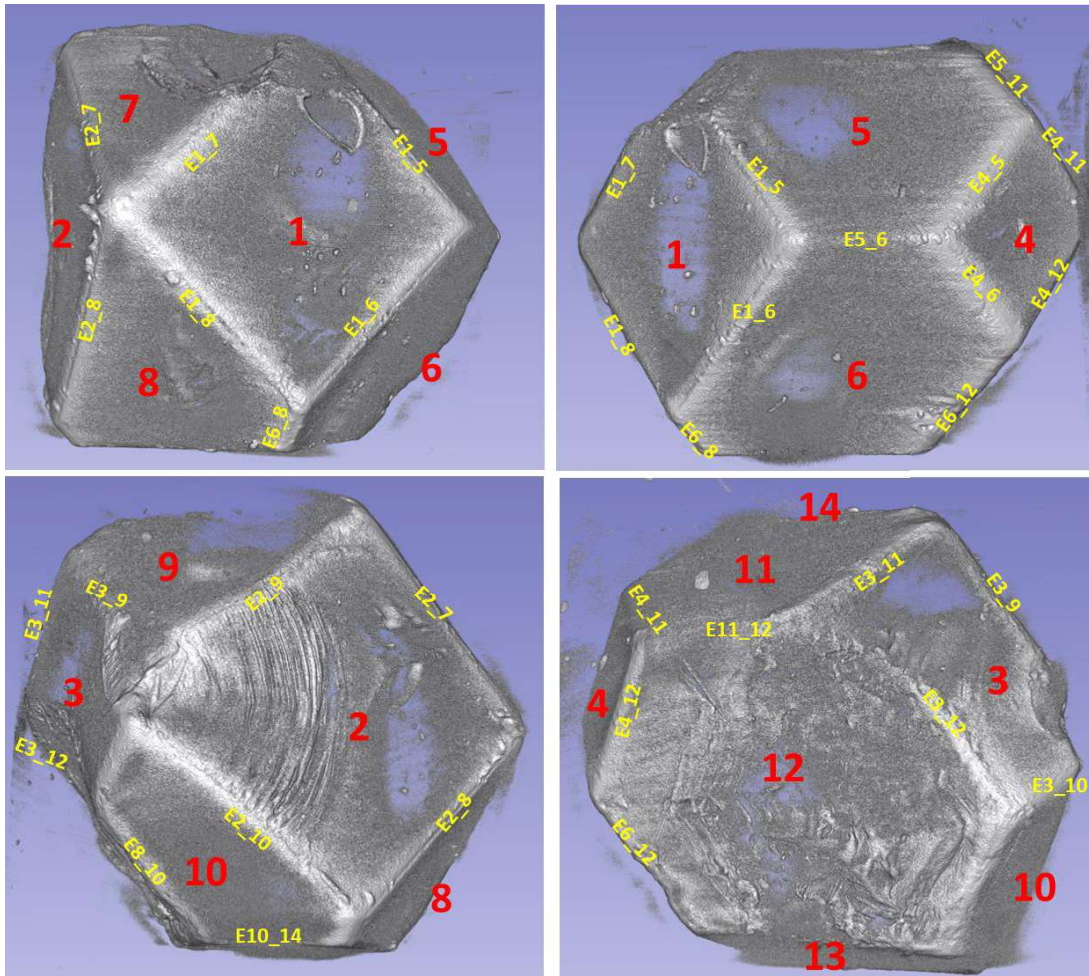


Figure V.7. Labels of different faces and edges of the Ni:P=1:2-10min diamond grit.

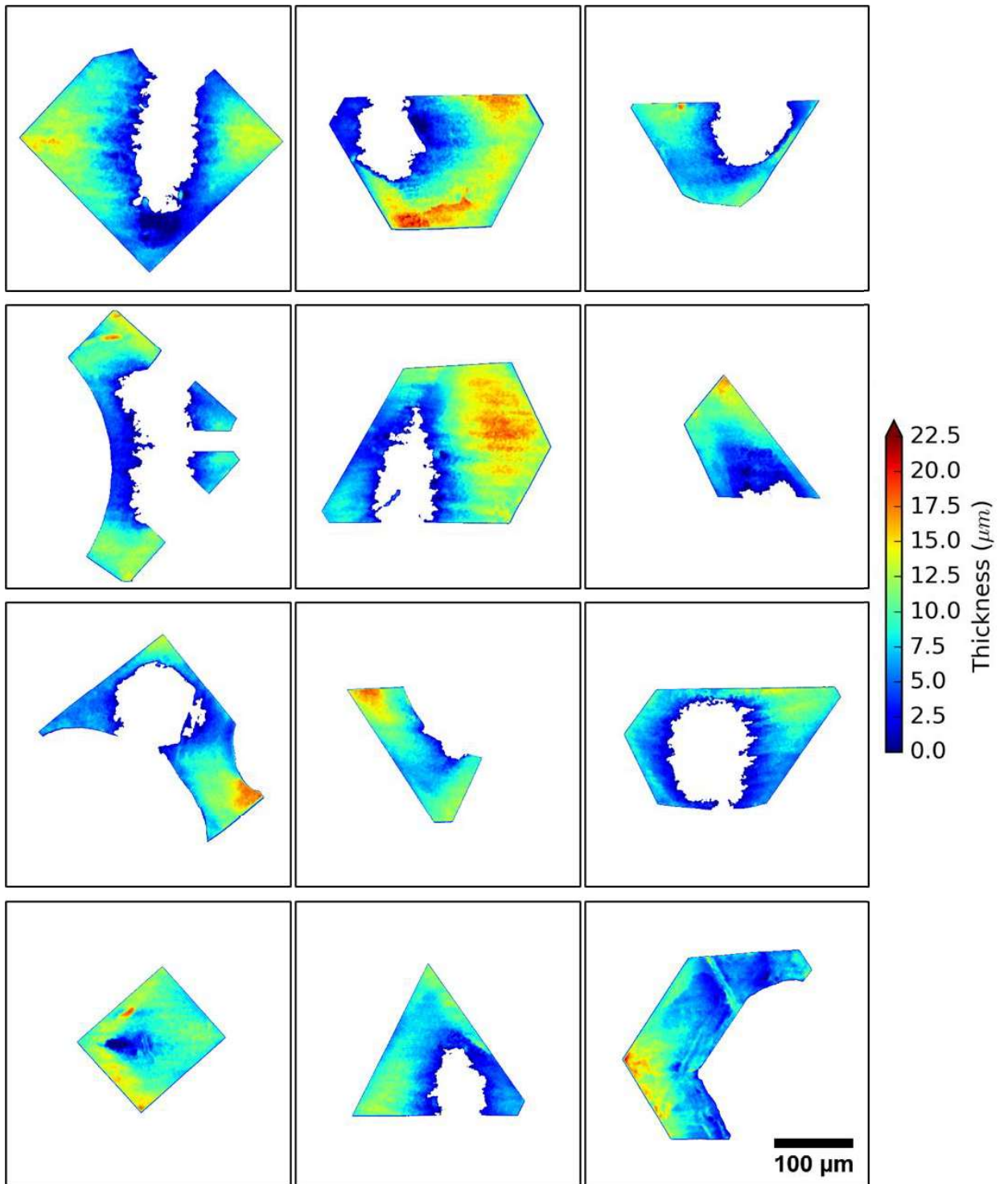


Figure V.8. Coating thickness distribution on different diamond faces.

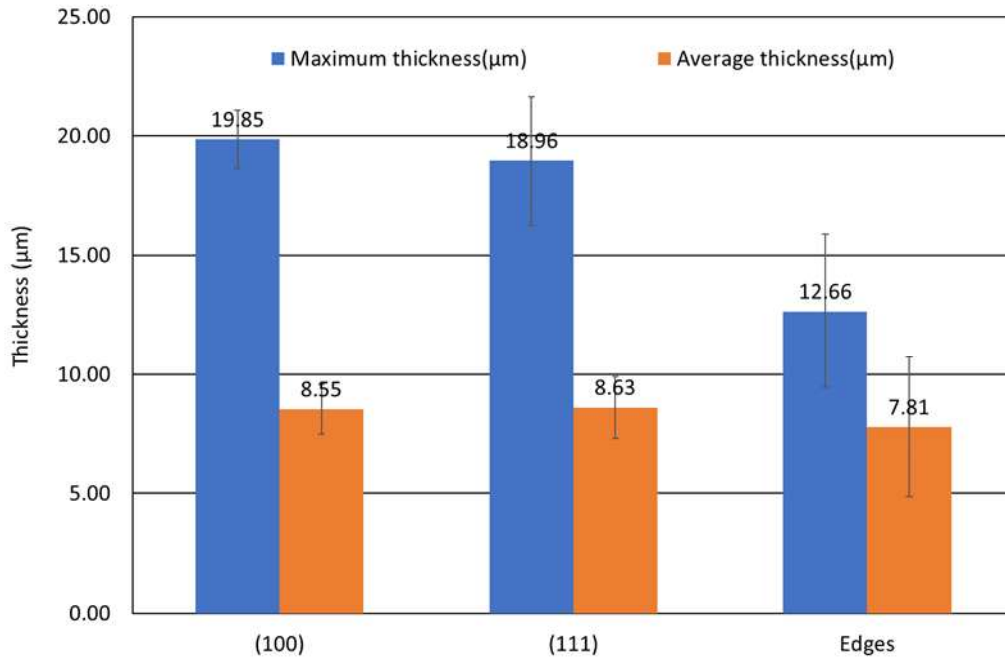


Figure V.9. Coating thickness on different faces and edges of the Ni:P=1:2-10min diamond grit.

5.3.2 Influence of reactants concentration

The thickness of electroless Ni-P coatings on each diamond particle is measured at flat surfaces from the tomography, and the results are plotted in Figure V.10.

According to the plots, the thickness increases with the plating time and the concentration of the reducing agent. In Figure V.10, it is seen that the coating thickness change with time has a steeper slope initially, and then the slopes decrease.

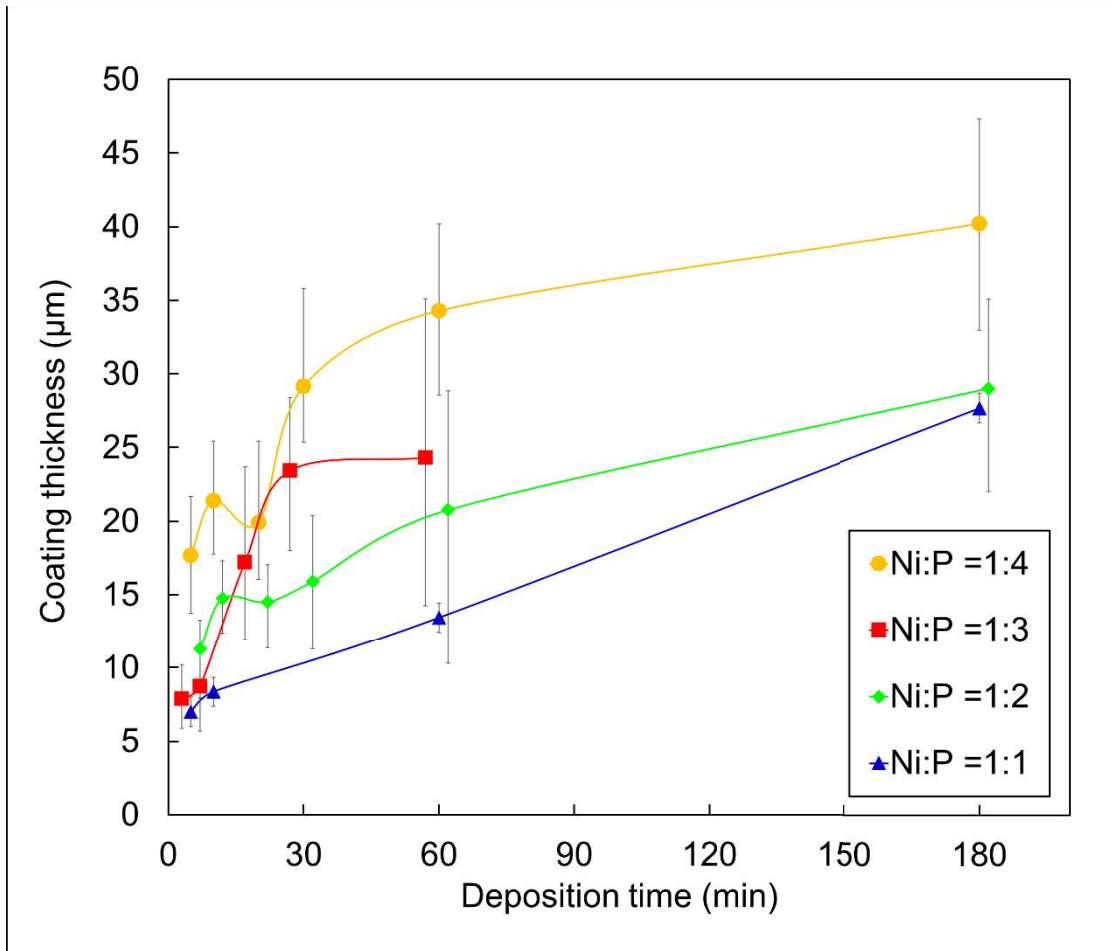


Figure V.10. Coating thickness with different deposition time and reducing agent concentrations. The position of time is shifted a little to show the error bar.

The average deposition rate was calculated by dividing the coating thickness by the deposition time, and the results are shown in Figure V.11. From this figure, the initial deposition rate is high and then decreases significantly within 20 minutes of deposition. After 1 hour's deposition, the rates reach a plateau. The deposition rate exhibits an increasing trend with the increase of the initial reducing agent concentration.

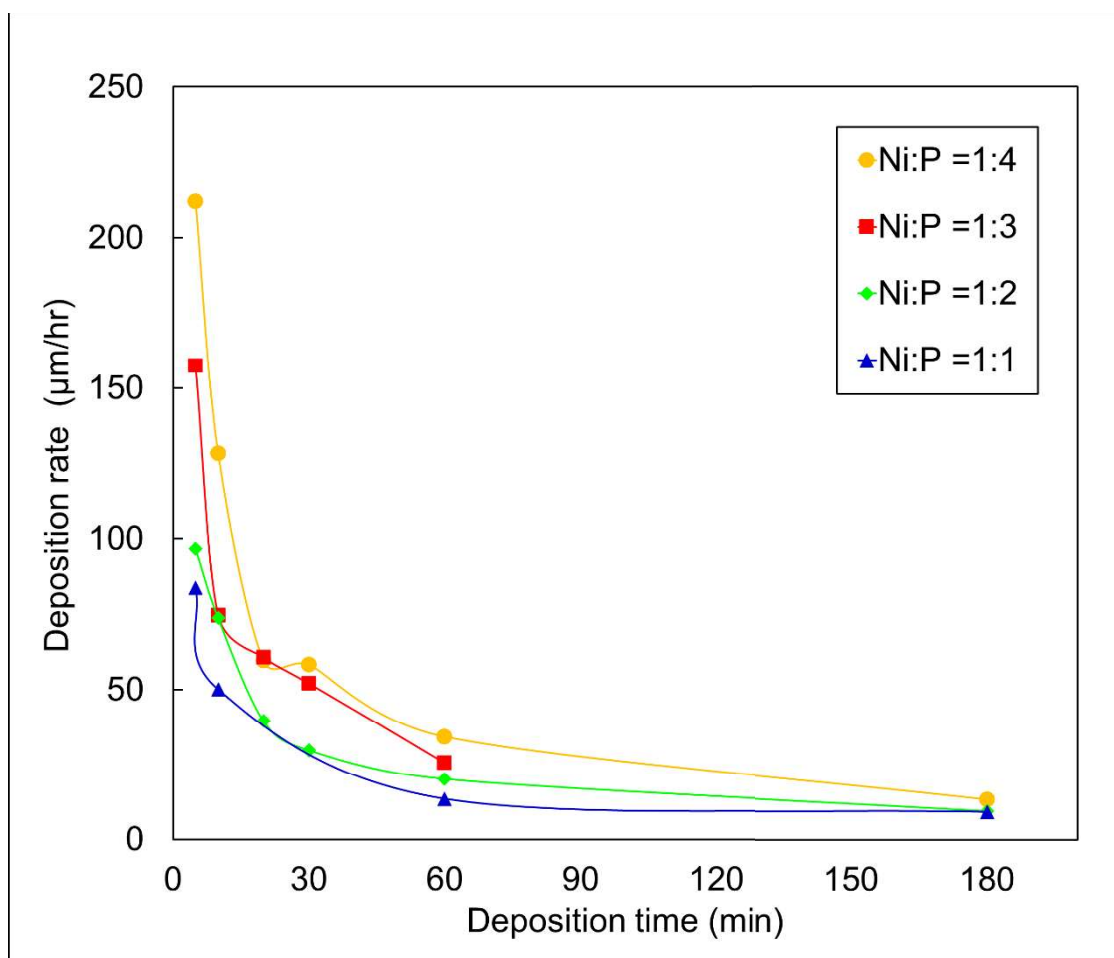


Figure V.11. Deposition rate change with different deposition time and reducing agent concentrations.

The decrease in deposition rate is mainly due to the consumption of reactants. To find the relationship between the deposition rate and reactant concentration, the concentrations of nickel species at different deposition time were calculated based on the conservation of nickel. The nickel species consists of free nickel ions and the nickel complexed with different complexing agents. So, the amount of the nickel species can

be calculated by subtracting the amount of deposited solid nickel from the total nickel input from the salt added to the solution. The results are plotted in Figure V.12.

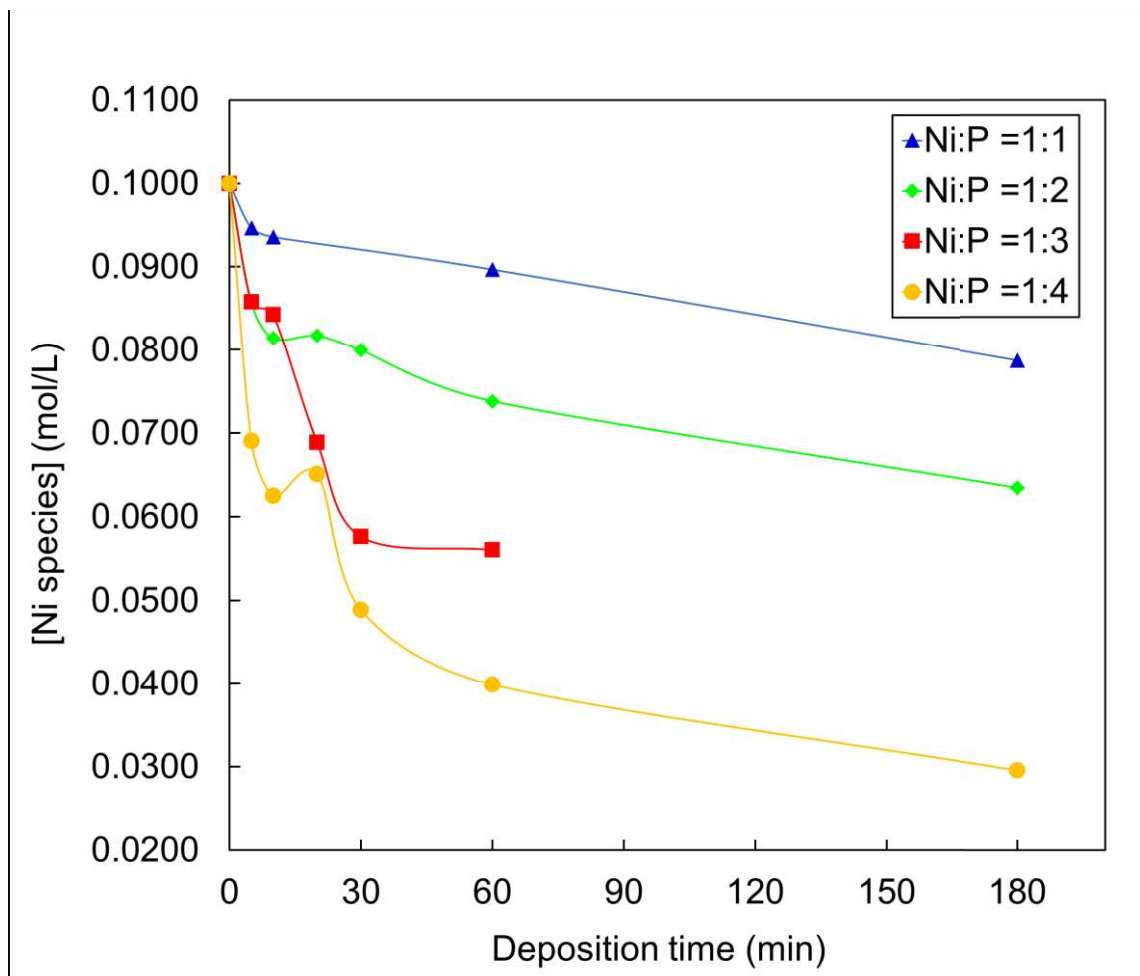


Figure V.12. The concentration of nickel species in the plating bath.

The deposition rates change with the nickel species concentration are plotted in Figure V.13. The curves are showing two separate stages. At low nickel species concentration, the deposition rates are low, and there is a linear correlation between deposition rate and nickel species concentration. When the nickel species concentration increases to a certain value, the deposition rate dramatically increases to a high value,

and there is no correlation between the nickel species concentration and the deposition rate. This phenomenon is in accordance with other reports^{69, 178}, yet there has been no explanation in their studies.

The dependence of the deposition rate with nickel ions concentration might be due to the complexing agent's action on the nickel species. When the nickel species concentration is low, there are enough complexing agents to form nickel complexes, leaving limited free nickel ions available for deposition. When the reduction reaction takes place, the consumption of nickel ions shifts the equilibrium of the complexing reaction and leads to the release of more free nickel ions from the complexes. In this case, the deposition rate depends on free nickel ions in the solution. When the nickel species concentration increases to a certain value, there is not enough complexing agent, such that the amount of free nickel ion in the solution is abundant. Therefore, the deposition rate depends on the release speed of electrons from the reducing agent oxidation.

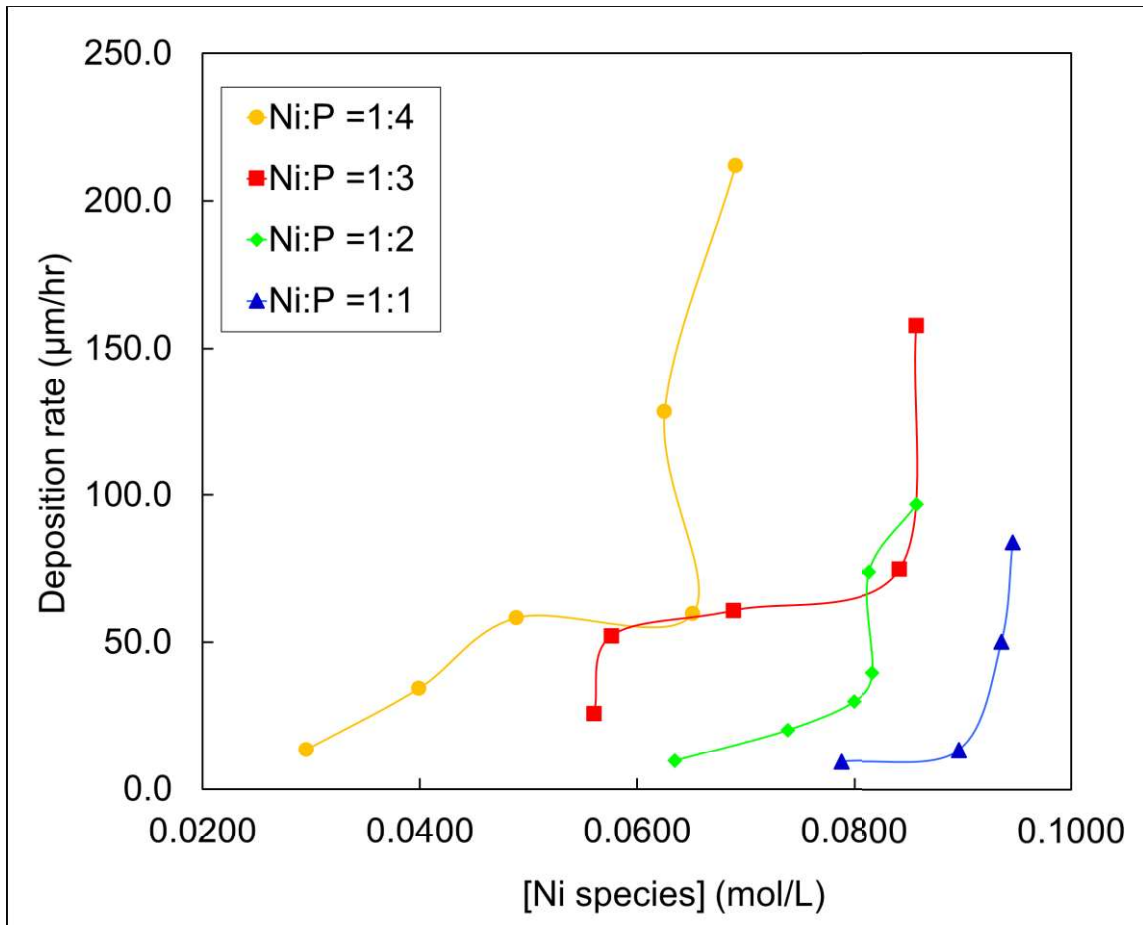


Figure V.13. Relationship of deposition rate with nickel species concentration.

To verify the above-proposed explanation of the relationship between the deposition rate and nickel species concentration, the free nickel ions concentration is calculated based on chemical reaction equilibrium. In the plating bath used in this study, the concentration of ammonia and citrate determines the free nickel ion concentrations because both the ammonia and the citrate can form complexes with nickel ions. The following reversible reactions and their equilibrium constants in Table V-1 help to find the free nickel ion concentration.

Table V-1 Equilibrium constants of the nickel ion determining reversible reactions

Reactions	Equilibrium. Constant. K	Expression of K
$NH_3 + H_2O \leftrightarrow NH_4^+ + OH^-$	1.76×10^{-5}	$K = \frac{[NH_4^+][OH^-]}{[NH_3]}$
$Ni^{2+} + 6NH_3 \leftrightarrow Ni(NH_3)_6^{2+}$	1.0×10^8	$K = \frac{[Ni(NH_3)_6^{2+}]}{[Ni^{2+}][NH_3]^6}$
$NiC_6H_5O_7^- \leftrightarrow Ni^{2+} + C_6H_5O_7^{3-}$	1.26×10^{-7}	$K = \frac{[Ni^{2+}][C_6H_5O_7^{3-}]}{[NiC_6H_5O_7^-]}$

The concentrations of reactants and products could be correlated using the expression of equilibrium constants - K. With the conservation of species in the solution, the following relationships are also built.

$$[Ni(NH_3)_6^{2+}] + [Ni^{2+}] + [NiC_6H_5O_7^-] = \text{Conc. of nickel species}$$

$$[NiC_6H_5O_7^-] + [C_6H_5O_7^{3-}] = 0.1 \text{ mol/L}$$

$$[NH_4^+] + [NH_3] + 6 \times [Ni(NH_3)_6^{2+}] = 2.09 \text{ mol/L}$$

$$[OH^-] = \frac{10^{-14}}{10^{-9.06}} = 1.14815 \times 10^{-5} \text{ mol/L}$$

The ammonium species concentration is larger than 2 mol/L from 0.1 mol/L $(NH_4)_2SO_4$ because the NH_4OH was added to adjust the pH value of the plating bath. The concentration of hydroxyl ions is calculated based on the measured pH value.

By solving the equations above, the relationship between the free nickel ions and the total nickel species in the solution can be identified, and results are plotted in Figure

V.14. The vertical axis is in logarithmic scale. The free nickel ion concentration and the increase rate (the slope of the curve) both increase with total nickel species. When the total nickel species concentration is less than 0.08 mol/L, the free nickel ions concentration is below 5×10^{-7} mol/L, and the slope is less than 3.5×10^{-5} , indicating a slow change rate. When the total nickel concentration is larger than 0.09 mol/L, the free nickel ion concentration is larger than 1×10^{-6} mol/L, and the slopes are larger than 1.5×10^{-4} , which is more than four times faster than the change rate at 0.08 mol/L. Since there is a big jump in the free nickel ion concentration when the total nickel species concentration change from 0.08 mol/L to 0.09 mol/L, the rate determine step change from the reduction of the free nickel ions (low free nickel ion concentration) to the oxidation of reducing agent (high free nickel ion concentration).

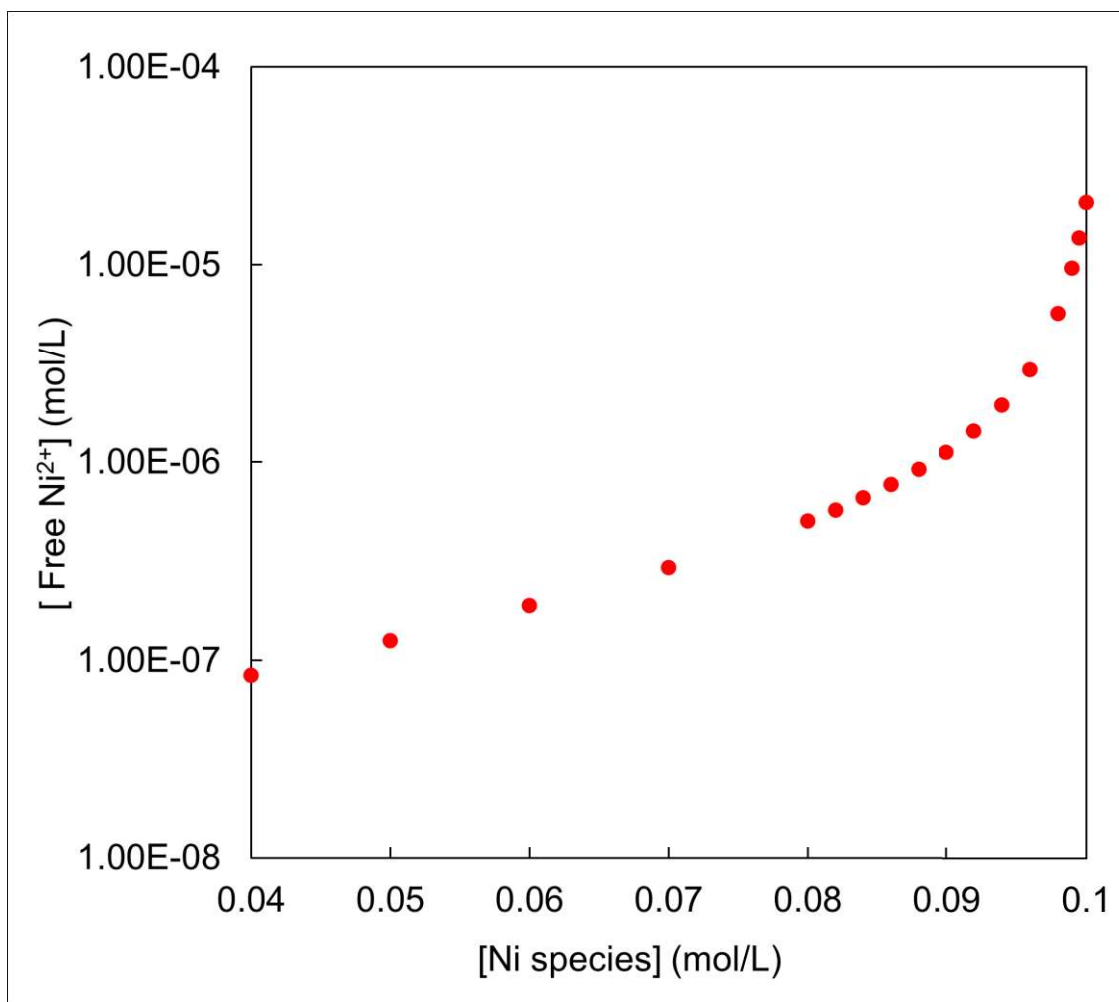


Figure V.14. Relation of free nickel ion concentration with total nickel species concentration in the plating solution.

5.4 Chapter summary of findings

This chapter discussed the morphology and tomography of the electroless deposited Ni-P coatings on diamond particles. The coating coverage, morphology, and deposition kinetics were obtained, and the factors influencing them were discussed. The following conclusions are drawn from the results.

The coating coverage is affected by the deposition time, substrate morphology, and reducing agent concentration. The nodular and smooth morphology are two major features of the coating. The formation of these morphologies is influenced by the deposition parameters, coating integrity, and substrate morphology. The processing suggestions based on the factors are provided for good coating coverage and desired coating morphology.

The deposition rate is not affected by the difference in crystallographic orientation. The dependence of the deposition rate on reactants concentrations is in a unique manner. The reducing agent concentration plays an important role in the deposition rate at the initial stage of the deposition. The higher the reducing agent concentration, the higher the deposition rate. As the deposition time increase, the dependence on reducing agent concentration diminishes while the deposition rate has a linear dependence on the nickel species concentration. This phenomenon is explained by the free nickel ion concentration calculated from the equilibrium of the complexes forming chemical reactions.

CHAPTER VI

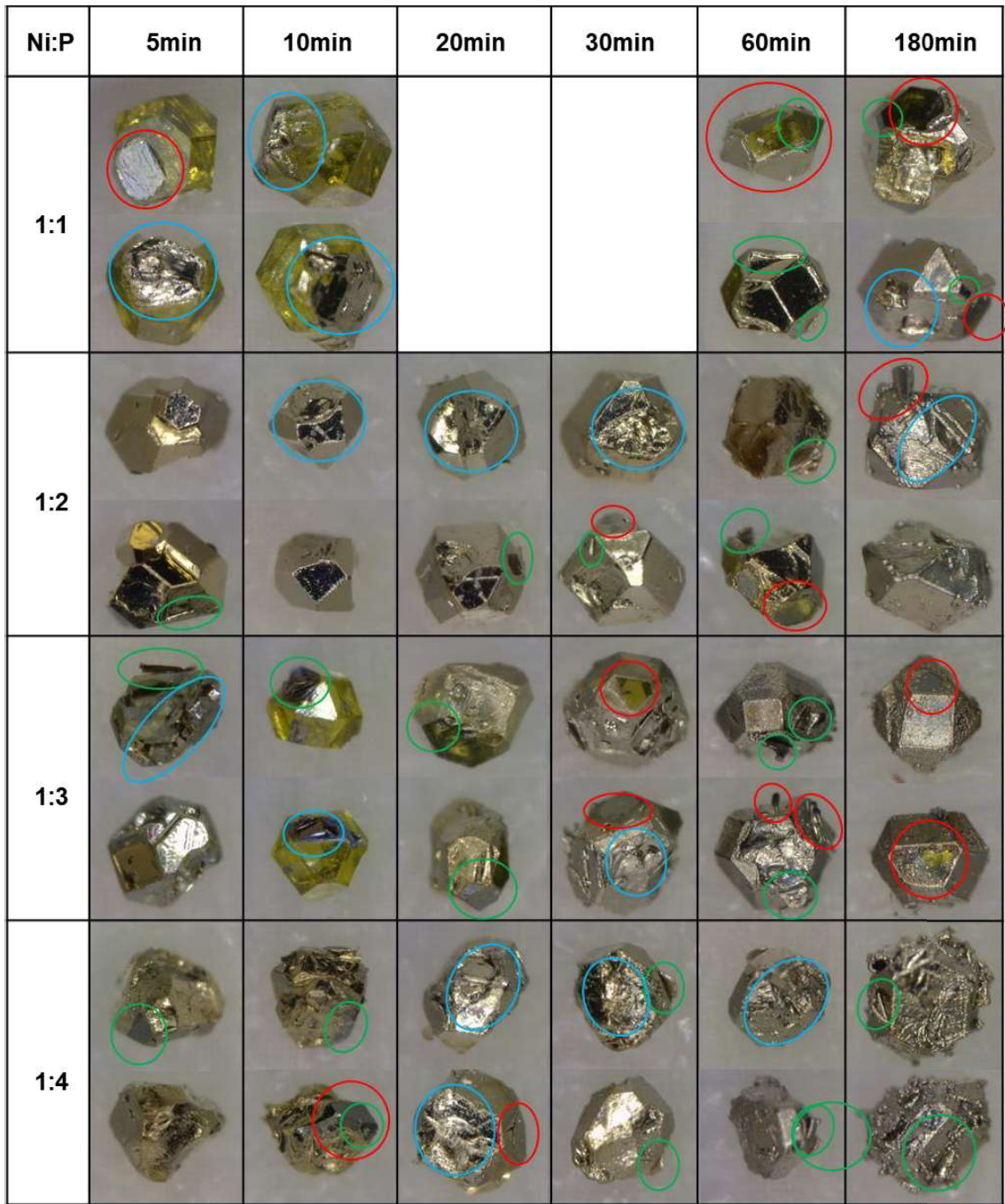
FAILURE MECHANISMS OF ELECTROLESS Ni-P ON DIAMOND PARTICLES

When using electrolessly-coated-diamond abrasives to fabricate machining tools, coating failure leads to lower manufacturing efficiency and reduced tool quality. To eliminate coating failure, the cause and the mechanism of the coating failure need to be understood. In this chapter, the substrate morphological features which promote or inhibit coating failure were identified based on the morphology analysis. The underlying mechanisms of how the substrate morphologic features affect coating failure tendencies were discovered.

6.1 Observation of coating failure

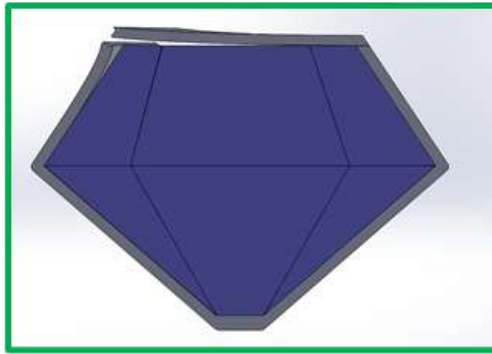
The coatings on diamond particles are damaged preferentially at certain locations. The locations of coating fracture and peeling off are encircled with different colors in the optical images of the as-plated samples, as shown in Figure VI.1. Most of the coating failures are found on the corners of the diamond particles (marked with green circles). Some of the failures are located on a flat surface of the diamond particles (marked with red circles). On the other hand, for the rough substrate surface, the coatings are in good shape (marked with blue circles). The tendencies of coating failure are summarized and illustrated in Figure VI.2.

To understand why the morphologies affect the coating affinity on the substrate, both the force that causes the coating fracture and the strength of the coating need to be analyzed.

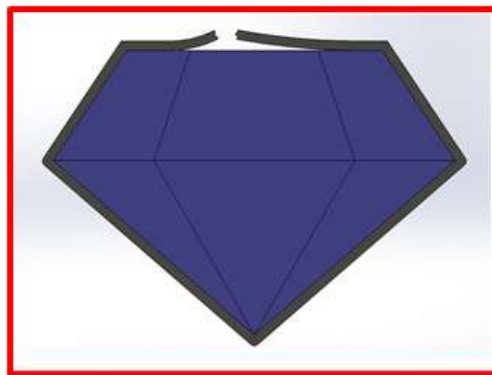


500 μm

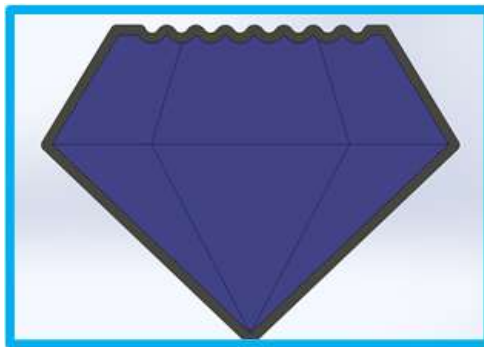
Figure VI.1 Optical images showing the coating failure locations: green color indicate corners, red indicates flat surface, and blue indicates rough surfaces.



(a)



(b)



(c)

Figure VI.2 Substrate morphologies with different coating failure tendencies. (a) the coating on the corner promotes failure, (b) the coating on flat surface promotes failure, (c) the coating on rough surface inhibits failure.

6.2 Physical model for coating failure

6.2.1 Origins of intrinsic stresses

The intrinsic stress created during the deposition process is the main cause of the coating failure when there are no other external forces exerted on the coatings. The intrinsic stresses in a coating arise from different origins, which include lattice misfit, defect annihilation, impurity inclusion, phase transformation, and crystallites coalescence. The possible origins are analyzed below to find out the critical ones which lead to the stress and cause the coating failure during the electroless deposition.

First, the lattice misfit is ruled out of the true origin in the electroless deposition. Since the generated coating is amorphous or polycrystalline, either there is no regular lattice parameter in the coating or the lattice misfit is other compensated by the grain boundaries. So the stress due to the difference in atomic spacing will not be accumulated in the coating.

The defects annihilation may also introduce intrinsic stresses in the electroless deposition process, but they will be on a much smaller scale. The defects include vacancies, dislocations, and grain boundaries which can be annihilated by diffusion. However, the low-temperature nature of the process indicates the annihilation of these defects occurs at a very low frequency during electroless deposition. So the stress generated will be very small.

Impurity in the electroless Ni-P coating mainly refers to the phosphorus atoms co-deposited with nickel. This kind of impurity can be regarded as uniform throughout the coating when the coating is thin, therefore, there is no volume change in the

thickness direction and thus no intrinsic stress is generated. For thick coatings, due to the consumption of hypophosphite in the plating bath, the phosphorus content will decrease as the thickness of coating increases. Because the size of the phosphorous atom is smaller, the volume of the coating will increase across the thickness, therefore, compressive stress will be generated in the coating. From the optical images, the outward curling of the fractured coating indicates tensile stress in the coating, so the phosphorus impurity is not the major cause in the coating failure.

The possible phase transformation of the Ni-P coating is from the amorphous phase to α -Ni and Ni₃P, but the temperature of transformation is 891 °C according to the Ni-P phase diagram¹⁷⁹. Since the deposition occurs at a relatively low temperature, the phase transformation is not likely to take place.

It is established that the electroless deposition is accompanied by the nodular crystallite's aggregation and growth^{172, 174}, which is also seen in our coatings, as shown in Figure IV.1 and Figure V.5. In a deposition process, the initiation of the coating is from heterogeneous nucleation sites, those sites are away from each other and grow bigger as the deposition time increases. Once the gap between the two crystallites becomes small enough, the cohesive force will attract the nearby crystallites. Because the bottoms of the crystallites are fixed on the substrate surface, the top portion of the crystallites will deform elastically and coalesce under the cohesive force. The coalescing results in a reduction of two units of solid-liquid interfacial energy and one unit of the grain boundary energy, hence the total surface energy of the coating is decreased¹³⁸. The

deformation is aiming to close the gap between the crystallites and reduce the total surface energy, so there will be stretching tensile stress generated in the coating.

Based on the analysis above, the intrinsic stress generated by the crystallites' coalescence in the electroless deposition is the dominating stress to cause coating fracture.

6.2.2 Estimation of the intrinsic stress

From the theory of intrinsic stress originated from coalesces of crystallites, the magnitude of the intrinsic stress can be estimated. The tensile stress generated in the coalescence is derived by Freund and Chase with a simple model¹³⁸. Equation VI-1 is used to calculate the average stress between two contacting spherical crystallites.

$$\sigma_{ave} = \frac{4(\gamma_{sl} - \frac{1}{2}\gamma_{gb})}{R} \quad \text{VI-1}$$

Where,

γ_{sl} is the surface energy at the solid-liquid interface

γ_{gb} is the grain boundary energy

Since the electroless deposition occurs in the solid-liquid interface, the surface energy in the equation is the interfacial energy between the plating solution and the deposited Ni-P alloy. The electroless Ni-P coatings have very different compositions and microstructure, thus the interfacial energy and grain boundary energies lack data.

Therefore, the interfacial energy of pure nickel and water and the grain boundary of pure nickel from literature are used to estimate the intrinsic stress. The surface energy γ_{sv} and grain boundary energy γ_{gb} of nickel are 1.78 J/m² and 0.57J/m² respectively¹⁸⁰. The

solid-liquid interfacial energy is estimated using Equation VI-2, with the surface energy of water at 70 °C to be 0.0644 J/m².

$$\gamma_{sl} = \gamma_{sv} - \gamma_{lv} \cos\theta \quad \text{VI-2}$$

The contact angle of nickel with water θ is measured to be around 90° for as-plated coating¹⁸¹. By plugging in all the data, the average stress in the coalesced crystallite is calculated for different nodular radius. The results are plotted in Figure VI.3 with blue dots and the blue curve. Equation VI-1 discloses that the average stress is inversely proportional to the radius of the crystallite. The estimated stress values show that for two crystallites of 1 nm radius, their coalescence can generate tensile stress as high as 6 GPa.

A simple criterion to determine whether the coating will fracture is by comparing the intrinsic stress with the tensile strength of the coating material. Many researchers have tested the tensile strength of electroless deposited Ni-P coatings with different compositions and after different heat treatment, in which the maximum tensile strength of as-plated Ni-P measure is 760 MPa¹⁸²⁻¹⁸⁴. When the crystallite radius is 7.8 nm, the stress is equal to the tensile strength of the coating.

However, the coating fracture is not likely to occur with only two nodules coalescence, because when the crystallites are too small, they are too far away from each other to coalesce. It is more likely when the crystallite grows bigger and more coalescences occur successively. When the accumulated stress is bigger than the tensile strength, the coating breaks. If we assume stress created by crystallite coalescence is cumulative, the number of successive coalescences that lead to the coating failure can be calculated. The calculated results are also plotted in Figure VI.3 with orange dots and the

orange curve. When the crystallites radii are 80 nm, it takes 10 successive coalescences for the generated intrinsic tensile stress to tear the coating apart.

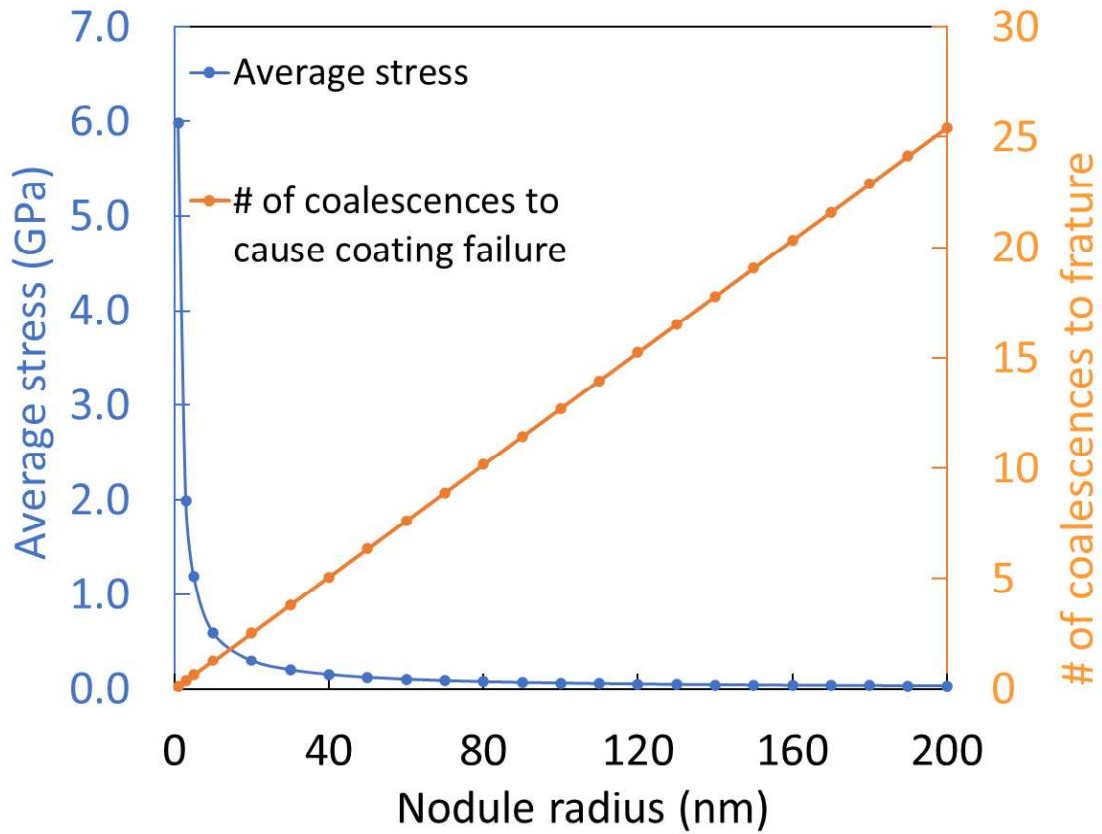
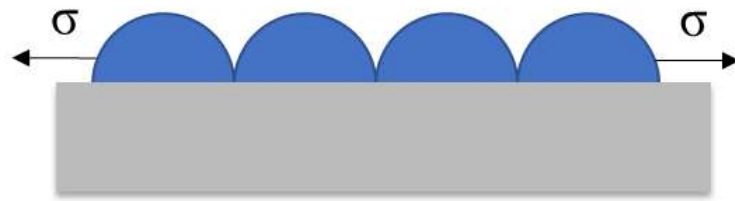


Figure VI.3. Average stress between two coalesced hemispheric crystallites and the number of coalescences to cause coating failure.

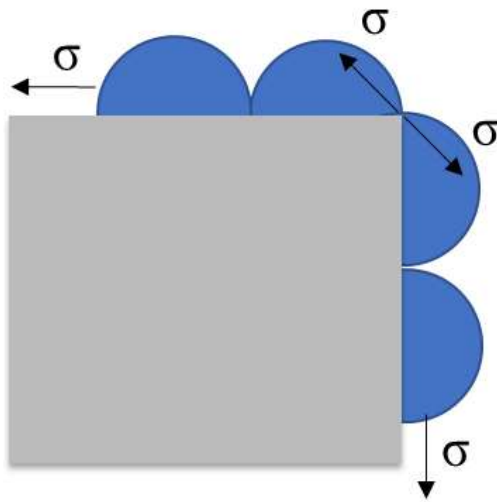
6.2.3 Coating failure mechanism

From the previous discussion, it is concluded that the coating in the electroless deposition process fails due to the accumulated intrinsic tensile stress generated by the coalescence of crystallites that forms the coating.

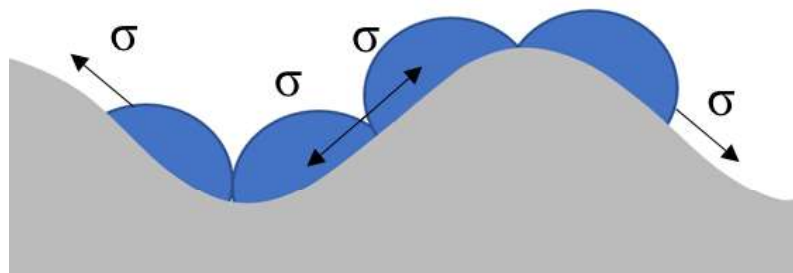
Based on this conclusion, the varied coating failure resistance of the different substrate morphological features can be explained. From the sketches in Figure VI.4, it is shown that the directions of stresses generated by crystallite coalescence change with the substrate morphologies. On a flat and smooth surface, as seen in Figure VI.4(a), the tensile stresses generated are parallel to the substrate surface when the crystallites coalesce. As more and more crystallites coalesce, the stress accumulates until the weakest point in the coating fractures. For the corner of a diamond substrate, presented in Figure VI.4(b), the tensile stresses are also parallel to the substrate and can accumulate when more crystallites merge. But the sharp corner acts as a stress concentrator, so it is easy to fracture. For a surface with some waviness, shown in Figure VI.4(c), the direction of tensile stress changes with the substrate waviness. In this case, the tensile stress may not accumulate to a big enough value if the distance between the peak and valley is too short, which prevents the coatings from fracture failures. Suitable substrate surface texture can be designed based on this mechanism to avoid coating failure.



(a)



(b)



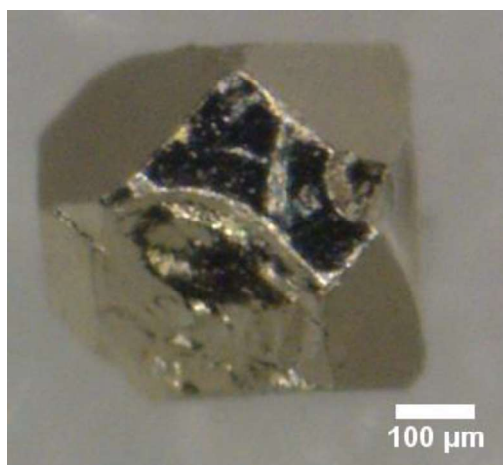
(c)

Figure VI.4. Ni-P crystallites coalescence on different morphologies of the substrate.

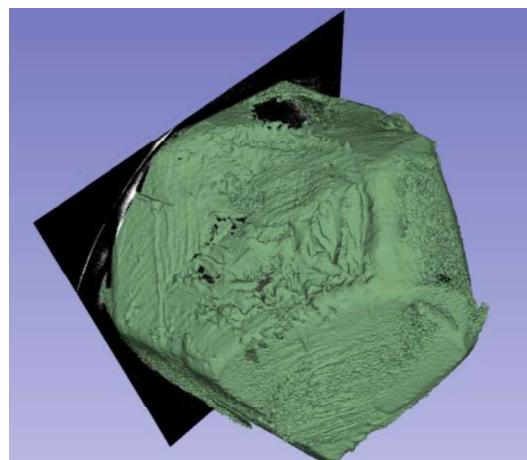
6.3 Coating failure modes

The internal stress can bend a thin strip of metal if a coating is plated on one surface of the strip. For coating on a diamond substrate, the substrate is extremely rigid and therefore will not bend. When the accumulated internal stress in the coating exceeds the coating's tensile strength, the coating fractures, deflects, and detaches from the diamond surface.

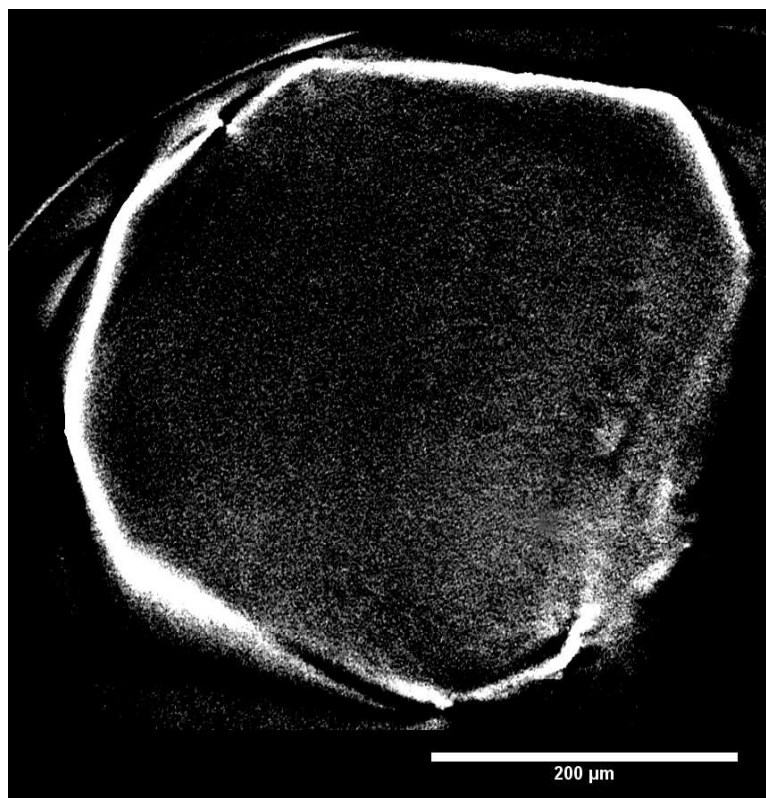
By observing tomography of the fractured coatings, two failure modes were found. The coatings which failed at the early stage of the deposition process, when the coating is still very thin, tend to experience plastic deformation (ductile) and can curl up heavily, as shown in Figure VI.6. The coatings which failed when the thickness already built up tend to fracture brittlely and little curling is present, as shown in Figure VI.5.



(a)

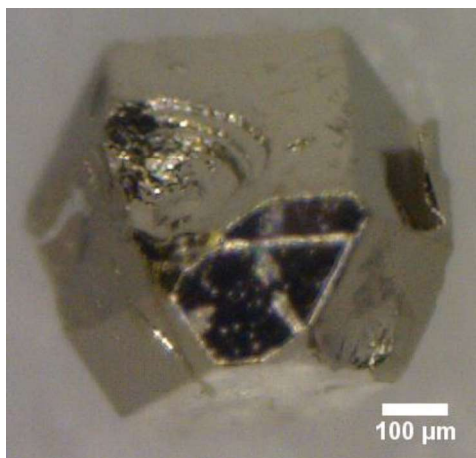


(b)

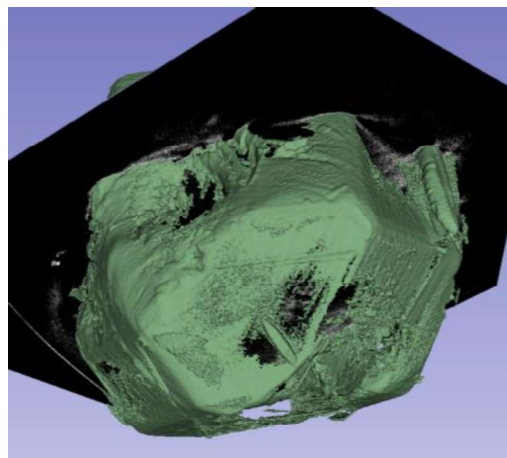


(c)

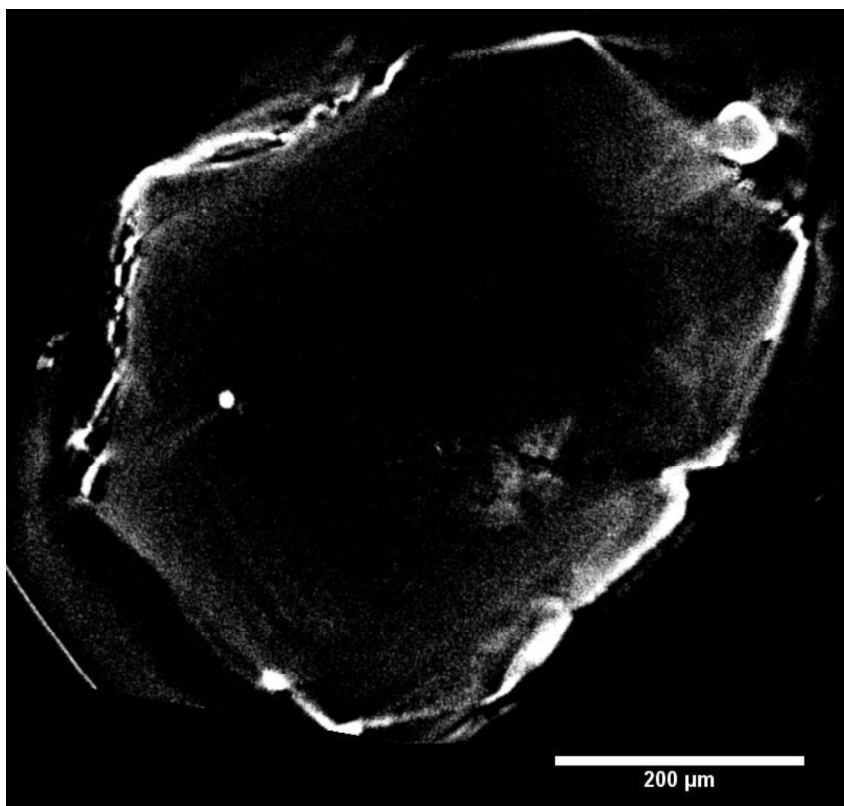
Figure VI.5. (a) The optical image, (b) 3D view of the volume-rendered image, and (c) tomography of Ni:P=1:2-10 min sample shows the brittle fracture.



(a)



(b)



(c)

Figure VI.6. (a) The optical image, (b) 3D view of the volume-rendered image, and (c) tomography of Ni:P=1:2-20 min sample shows the ductile fracture.

6.4 Chapter summary of findings

In this chapter, the coating failure mechanism is correlated to the substrate morphologies and the following findings are discovered.

The morphological features of the substrate are identified with different tendencies for coating failure. It was found that the coating prefers to fail at the flat surfaces and corners of the substrate while remaining intact at the rough surfaces.

By analyzing the origins of intrinsic stresses, the major cause of coating failure is found to be the intrinsic tensile stress induced by crystallites coalescence. The magnitudes of the intrinsic stress were calculated with different crystallite radii and the number of coalescences to break the coating was also estimated.

The discovered failure mechanism explains the relationship between the coating failure tendency with the substrate morphology. Coatings tend to fail on flat surfaces and corners formed by two flat surfaces because the accumulation of intrinsic stress generated by crystallite coalescence is allowed on large flat surfaces. On the other hand, the rough or waving surface limits the accumulation of intrinsic stress because the stress changes directions with the substrate.

Additionally, two modes of fractured coatings were categorized: ductile and brittle. The fracture and ductile curling occur when the film is thin or at high temperature, while the brittle fracture without much deformation occurs when the film is too thick to curl under the residual stress.

CHAPTER VII

CONCLUSIONS AND FUTURE RECOMMENDATIONS

7.1 Conclusions

This research investigated the electroless plated Ni-P coatings on diamond particles through electrochemical and morphological characterizations to understand the coating deposition process and its failure mechanisms. In this section, the major findings are summarized.

With a new electrode made of Ni-P alloy coating on diamond particles, several electrochemical experiments were performed and the following discoveries are found.

1. Potential polarization results show that a high concentration electroplating solution (300g/L nickel sulfamate) is less corrosive to the coatings due to two passivation stages.
2. The durability of the coating was successfully examined using open circuit potential (OCP) and linear polarization resistance (LPR) monitoring. The results suggested that open circuit potential (OCP) and linear polarization resistance (LPR) monitoring over time give a good indication of coating conditions.

The morphological study of the electroless Ni-P on diamond particles was conducted using X-ray tomography along with several other microscopic methods. The following conclusions were drawn.

3. The coating coverage rate on diamond particles is affected by the synergistic action of the deposition time, substrate morphology, and reducing agent concentration.
4. The two major morphological features of the coating: nodular and smooth are influenced by the deposition parameters, coating integrity, and substrate morphology.
5. The deposition rate is not affected by the difference in crystallographic orientation but mainly depends on the concentrations of the reactants. The dependence of deposition rate with nickel species concentration in the solution is explained by the free nickel ion concentration, which was successively calculated from the equilibrium of the complexes forming chemical reactions.
6. The morphological features of the substrate which affect the coating failures tendencies were recognized. Flat smooth surface and corners areas promote the coating failure while rough surfaces retain the coating.
7. Two modes of coating failure are identified: elastic deformation and plastic deformation after a fracture.

There two coating failure mechanisms found in this study.

8. The coatings fail through corrosion assisted pinhole breakthrough.
9. The coatings fracture due to residual stress developed during the deposition process.

This study provides two novel methods to characterize the electroless Ni-P coatings on abrasive diamond grits. Firstly, a self-designed electrode was used which enables the collecting of electrochemical signals in corrosion tests. Secondly, by applying X-ray tomography techniques that enable the 3D views in high resolution, the detailed information of the coating on the diamond particles was obtained. These methods can be applied to other metal coatings/powder substrate systems.

7.2 Future recommendations

The recommendations for future study have three aspects described below.

7.2.1 Plating bath modification

In this study, only few components in an electroless plating bath were used to simplify factors affecting coatings. In real industrial applications, more additives are added to improve coating properties. Therefore, in the future, the effects of other additives can be investigated.

Alkali solution was used since it has a faster plating rate. The purpose of this selection is to find a way to improve the coating quality while maintaining a high production rate. It is also recommended to use a slower plating bath to generate coatings with fewer defects and examine the coatings' quality subject to a harsh environment such as erosion or tribocorrosion.

7.2.2 Optimization of electrochemical performance

In chapter IV, the same coating was tested in different electrolytes mainly to study the electrolyte effects on the corrosion resistance. Various coatings with different compositions and the microstructures can be produced by changing the plating bath

composition and plating conditions. Therefore, these coatings can be electrochemically characterized to find optimal products for corrosion-resistant coatings.

7.2.3 Mechanical properties modeling

As mentioned at the end of chapter VI, the tomography can tell the curvature of the fractured coating and the thickness of the coating near the fractured section. Those parameters will help in building a model to correlate the coating's mechanical properties at the moment of fracture thus reveal the coating properties evolution during the deposition process.

REFERENCES

1. Fauchais, P.; Vardelle, A., Thermal Sprayed Coatings Used Against Corrosion and Corrosive Wear. In *Advanced Plasma Spray Applications*, 2012; pp 1-38.
2. Zhang, Z.; Chen, P.; Yang, X.; Liu, Y.; Ma, H.; Li, J.; Zhao, B.; Luo, J.; Duan, X.; Duan, X., Ultrafast growth of large single crystals of monolayer WS₂ and WSe₂. *National Science Review* **2020**, 7 (4), 737-744.
3. Galhenage, R. P.; Xie, K.; Diao, W. J.; Tengco, J. M. M.; Seuser, G. S.; Monnier, J. R.; Chen, D. A., Platinum-ruthenium Bimetallic Clusters on Graphite: a Comparison of Vapor Deposition and Electroless Deposition Methods. *Phys Chem Chem Phys* **2015**, 17 (42), 28354-28363.
4. Navinšek, B.; Panjan, P.; Milošev, I., PVD Coatings as an Environmentally Clean Alternative to Electroplating and Electroless Processes. *Surface and Coatings Technology* **1999**, 116-119, 476-487.
5. Yun, J.-H.; Park, S.-K., Theoretical study of step coverage and comparison with experimental results from low pressure chemical vapor deposition process of tungsten film. *Jpn J Appl Phys* **1995**, 34 (6R), 3216.
6. Jilani, A.; Abdel-wahab, M. S.; Hammad, A. H., Advance Deposition Techniques for Thin Film and Coating. In *Modern Technologies for Creating the Thin-film Systems and Coatings*, 2017; pp 137-149.
7. Freund, L. B.; Suresh, S., *Thin Film Materials: Stress, Defect Formation and Surface Evolution*. Cambridge University Press: Cambridge, 2004.
8. Schwartz, M., Deposition from aqueous solutions: an overview. In *Handbook of Deposition Technologies for Films and Coatings—Science, Technology and Applications*, 1994; pp 506-616.
9. Davidson, R.; Verma, A.; Santos, D.; Hao, F.; Fincher, C.; Xiang, S.; Van Buskirk, J.; Xie, K.; Pharr, M.; Mukherjee, P. P.; Banerjee, S., Formation of Magnesium Dendrites during Electrodeposition. *ACS Energy Letters* **2018**, 4 (2), 375-376.

10. Lu, L.; Sui, M. L.; Lu, K., Cold Rolling of Bulk Nanocrystalline Copper. *Acta Materialia* **2001**, *49* (19), 4127-4134.
11. Natter, H.; Hempelmann, R., Nanocrystalline Copper by Pulsed Electrodeposition: The Effects of Organic Additives, Bath Temperature, and pH. *The Journal of Physical Chemistry* **1996**, *100* (50), 19525-19532.
12. Jeon, S.-H.; Choi, W.-I.; Song, G.-D.; Son, Y.-H.; Hur, D., Influence of surface roughness and agitation on the morphology of magnetite films electrodeposited on carbon steel substrates. *Coatings* **2016**, *6* (4), 62.
13. Zamanzad-Ghavidel, M.; Raeissi, K.; Saatchi, A., Effect of Substrate Texture and Deposition Current Density on Properties of Ni nanocrystalline Electrodeposits. *Iranian Journal of Materials Science and Engineering* **2012**, *9* (2), 1-14.
14. Tsyntaru, N.; Cesiulis, H.; Pellicer, E.; Celis, J. P.; Sort, J., Structural, Magnetic, and Mechanical Properties of Electrodeposited Cobalt–tungsten Alloys: Intrinsic and Extrinsic Interdependencies. *Electrochim Acta* **2013**, *104*, 94-103.
15. Kahanda, G.; Tomkiewicz, M., Morphological Evolution in Zinc Electrodeposition. *J Electrochem Soc* **1989**, *136* (5), 1497-1502.
16. Ebothé, J.; Vilain, S., Surface roughness and morphology of Co-(Fe and Ni) binary alloy electrodeposits studied by atomic force microscopy. *Journal of Physics D: Applied Physics* **1999**, *32* (18), 2342.
17. Vas'ko, V. A.; Tabakovic, I.; Riemer, S. C.; Kief, M. T., Effect of organic additives on structure, resistivity, and room-temperature recrystallization of electrodeposited copper. *Microelectron Eng* **2004**, *75* (1), 71-77.
18. Marinho, F. A.; Santana, F. S. M.; Vasconcelos, A. L. S.; Santana, R. A. C.; Prasad, S., Optimization of operational parameters and bath control for electrodeposition of Ni-Mo-B amorphous alloys. *J Brazil Chem Soc* **2002**, *13* (4), 522-528.

19. Rusli, E.; Xue, F.; Drews, T. O.; Vereecken, P. M.; Andricacos, P.; Deligianni, H.; Braatz, R. D.; Alkire, R. C., Effect of additives on shape evolution during electrodeposition - II. Parameter estimation from roughness evolution experiments. *J Electrochem Soc* **2007**, *154* (11), D584-D597.
20. Qin, Y.; Li, X. H.; Xue, F.; Vereecken, P. M.; Andricacos, P.; Deligianni, H.; Braatz, R. D.; Alkire, R. C., Effect of additives on shape evolution during electrodeposition - III. Trench infill for on-chip interconnects. *J Electrochem Soc* **2008**, *155* (3), D223-D233.
21. Walsh, F. C.; de Leon, C. P.; Kerr, C.; Court, S.; Barker, B. D., Electrochemical characterisation of the porosity and corrosion resistance of electrochemically deposited metal coatings. *Surf Coat Tech* **2008**, *202* (21), 5092-5102.
22. Xu, X. Q.; Miao, J.; Bai, Z. Q.; Feng, Y. R.; Ma, Q. R.; Zhao, W. Z., The corrosion behavior of electroless Ni-P coating in Cl⁻/H₂S environment. *Appl Surf Sci* **2012**, *258* (22), 8802-8806.
23. Vossen, J. L.; Schnable, G. L.; Kern, W., Processes for multilevel metallization. *Journal of Vacuum Science and Technology* **1974**, *11* (1), 60-70.
24. Bleeks, T. W.; Brindisi, F. In *The properties and characteristics of electroless nickel coatings applied to gas turbine engine components*, Proceedings of the ASME 1989 International Gas Turbine and Aeroengine Congress and Exposition, Toronto, Ontario, Canada, June 4-8; American Society of Mechanical Engineers: Toronto, Ontario, Canada, 1989; pp 1-6.
25. Mainier, F. B.; Fonseca, M. P. C.; Tavares, S. S. M.; Pardal, J. M., Quality of Electroless Ni-P (Nickel-Phosphorus) Coatings Applied in Oil Production Equipment with Salinity. *Journal of Materials Science and Chemical Engineering* **2013**, *01* (06), 1-8.
26. Yoshino, M.; Nonaka, Y.; Sasano, J.; Matsuda, I.; Shacham-Diamand, Y.; Osaka, T., All-wet fabrication process for ULSI interconnect technologies. *Electrochim Acta* **2005**, *51* (5), 916-920.

27. Kim, T.-Y.; Son, H.-J.; Lim, S.-K.; Song, Y.-I.; Park, H.-S.; Suh, S.-J., Electroless Nickel Alloy Deposition on SiO₂ for Application as a Diffusion Barrier and Seed Layer in 3D Copper Interconnect Technology. *J Nanosci Nanotechno* **2014**, *14* (12), 9515-9524.
28. Liu, D. G.; Mai, Y. J.; Sun, J.; Luan, Z. J.; Shi, W. C.; Luo, L. M.; Li, H.; Wu, Y. C., Surface metallization of Cu/Ni/Au coatings on diamond/Cu composite materials for heat sink application. *Ceram Int* **2017**, *43* (16), 13133-13139.
29. Hamid, Z. A.; Moustafa, S. F.; Morsy, F. A.; khalifa, N. A. A.; Mouez, F. A., Fabrication and characterization copper/diamond composites for heat sink application using powder metallurgy. *Natural Science* **2011**, *03* (11), 936-947.
30. Parameswaran, M.; Xie, D.; Glavina, P., Fabrication of Nickel Micromechanical Structures Using a Simple Low - Temperature Electroless Plating Process. *J Electrochem Soc* **1993**, *140* (7), L111-L113.
31. Tottori, S.; Zhang, L.; Qiu, F.; Krawczyk, K. K.; Franco-Obregon, A.; Nelson, B. J., Magnetic helical micromachines: fabrication, controlled swimming, and cargo transport. *Adv Mater* **2012**, *24* (6), 811-6.
32. Wang, J.; Zhang, F.-L.; Zhang, T.; Liu, W.-G.; Li, W.-X.; Zhou, Y.-M., Preparation of Ni-P-diamond coatings with dry friction characteristics and abrasive wear resistance. *International Journal of Refractory Metals and Hard Materials* **2018**, *70*, 32-38.
33. Yan, M.; Ying, H. G.; Ma, T. Y., Improved microhardness and wear resistance of the as-deposited electroless Ni-P coating. *Surface and Coatings Technology* **2008**, *202* (24), 5909-5913.
34. Sahoo, P.; Das, S. K., Tribology of electroless nickel coatings – A review. *Mater Design* **2011**, *32* (4), 1760-1775.
35. Mukhopadhyay, A.; Duari, S.; Barman, T. K.; Sahoo, P., Wear behavior of electroless Ni-P-W coating under lubricated condition - a Taguchi based approach. *IOP Conference Series: Materials Science and Engineering* **2016**, *149*, 012004.

36. Krishnaveni, K.; Sankara Narayanan, T. S. N.; Seshadri, S. K., Electroless Ni–B coatings: preparation and evaluation of hardness and wear resistance. *Surface and Coatings Technology* **2005**, *190* (1), 115-121.
37. Song, Y. W.; Shan, D. Y.; Han, E. H., High corrosion resistance of electroless composite plating coatings on AZ91D magnesium alloys. *Electrochim Acta* **2008**, *53* (5), 2135-2143.
38. Ohring, M., Chapter 4 - Discharges, Plasmas, and Ion–Surface Interactions. In *Materials Science of Thin Films (Second Edition)*, Ohring, M., Ed. Academic Press: San Diego, 2002; pp 145-202.
39. Ohring, M., Chapter 3 - Thin-Film Evaporation Processes. In *Materials Science of Thin Films (Second Edition)*, Ohring, M., Ed. Academic Press: San Diego, 2002; pp 95-144.
40. Carlsson, J.-O.; Martin, P. M., Chapter 7 - Chemical Vapor Deposition. In *Handbook of Deposition Technologies for Films and Coatings (Third Edition)*, Martin, P. M., Ed. William Andrew Publishing: Boston, 2010; pp 314-363.
41. Ohring, M., Chapter 6 - Chemical Vapor Deposition. In *Materials Science of Thin Films (Second Edition)*, Ohring, M., Ed. Academic Press: San Diego, 2002; pp 277-355.
42. Tsao, J. Y., *Materials Fundamentals of Molecular Beam Epitaxy*. Academic Press: San Diego, CA, 2012.
43. Pimpinelli, A.; Villain, J., *Physics of crystal growth*. Cambridge University Press: Cambridge, U.K., 1998.
44. Venables, J., *Introduction to surface and thin film processes*. Cambridge University Press: Cambridge, U.K., 2000.
45. Mohler, J. B., *Electroplating and Related Processes*. Chemical Publishing Company: Los Angeles, CA, 1969.

46. McCafferty, E., *Introduction to Corrosion Science*. Springer: New York, 2010.
47. Watanabe, T., *Nano Plating - Microstructure Formation Theory of Plated Films and a Database of Plated Films*. Elsevier: Amsterdam, 2004.
48. Paunovic, M.; Schlesinger, M., *Fundamentals of electrochemical deposition*. Wiley: New Jersey, 2006.
49. Djokic, S. S., *Electrodeposition: Theory and Practice*. Springer: New York, 2010.
50. Kanani, N., *Electroplating: Basic Principles, Processes and Practice*. Elsevier: Amsterdam, 2004.
51. Reed-Hill, R. E.; Abbaschian, R.; Abbaschian, R., *Physical metallurgy principles*. Cengage Learning: Boston, MA, 1973; Vol. 17.
52. Schuh, C. A.; Nieh, T. G., Hardness and Abrasion Resistance of Nanocrystalline Nickel Alloys Near the Hall-Petch Breakdown Regime. *MRS Proceedings* **2002**, 740, I1.8.1-I1.8.6.
53. Bockris, J. O. M.; Reddy, A. K. N., *Modern Electrochemistry: An Introduction to an Interdisciplinary Area*. Plenum Press: New York, 1970; Vol. 1.
54. Mizushima, I.; Chikazawa, M.; Watanabe, T., Microstructure of Electrodeposited Cu - Ni Binary Alloy Films. *J Electrochem Soc* **1996**, 143 (6), 1978-1983.
55. Watanabe, T., Formation of metastable phases by the plating method. *Materials Science and Engineering: A* **1994**, 179-180, 193-197.
56. Yeh, X.; Samwer, K.; Johnson, W., Formation of an amorphous metallic hydride by reaction of hydrogen with crystalline intermetallic compounds—a new method of synthesizing metallic glasses. *Appl Phys Lett* **1983**, 42 (3), 242-243.

57. Kim, Y.-G.; Lee, J.-Y., The mechanism of hydrogen-induced amorphization in intermetallic compounds. *J Alloy Compd* **1992**, *187* (1), 1-7.
58. Aoki, K.; Masumoto, T., Hydrogen-induced amorphization of intermetallics. *J Alloy Compd* **1995**, *231* (1-2), 20-28.
59. Shibuta, Y.; Oguchi, K.; Takaki, T.; Ohno, M., Homogeneous nucleation and microstructure evolution in million-atom molecular dynamics simulation. *Scientific reports* **2015**, *5*, 13534.
60. Gavrilov, G. G., *Chemical (electroless) nickel-plating*. Portcullis Press: Redhill, Surrey, 1979.
61. Roux, F. A. Process of producing metallic deposits. U.S. Patent 1,207,218, Dec 5, 1916.
62. Brenner, A.; Riddell, G. E., Nickel Plating on Steel by Chemical Reduction. *J Res Nat Bur Stand* **1946**, *37* (1), 31-34.
63. Brenner A, R. G. Nickel plating by chemical reduction. U.S. Patent 2,532,283, Dec 5, 1950.
64. Mallory, G. O., The Fundamental Aspects of Electroless Nickel Plating. In *Electroless Plating: Fundamentals and Applications*, Mallory, G. O.; Hajdu, J. B., Eds. Cambridge University Press: Cambridge, U.K., 1990; pp 1-56.
65. Lambert, R. M.; Pacchioni, G., Chemisorption and Reactivity on Supported Clusters and Thin Films : Towards an Understanding of Microscopic Processes in Catalysis. In *NATO ASI series Series E: Applied sciences*, Kluwer Academic Publisher: Dordrecht 1997; pp 1-27.
66. Watanabe, T., Amorphous plating. In *Current Topics in Amorphous Materials*, Sakurai, Y.; Hamakawa, Y.; Masumoto, T.; Shirae, K.; Suzuki, K., Eds. Elsevier: Oxford, 1993; pp 137-149.

67. Singh, D. D. N.; Ghosh, R., Electroless nickel-phosphorus coatings to protect steel reinforcement bars from chloride induced corrosion. *Surf Coat Tech* **2006**, *201* (1-2), 90-101.
68. Balaraju, J. N.; Anandan, C.; Rajam, K. S., Electroless deposition of ternary Ni-W-P alloys from sulphate and chloride based baths. *Surf Eng* **2005**, *21* (3), 215-220.
69. Mallory, G. O.; Hajdu, J. B., *Electroless Plating: Fundamentals and Applications*. Cambridge University Press: Cambridge, U.K., 1990; p 62-65.
70. Liang, H.; Xiao, K.; Wei, L.; Yang, B.; Yu, G.; Deng, S.; Duan, H.; Zhu, C.; Li, J.; Zhang, J., Decomplexation removal of Ni(II)-citrate complexes through heterogeneous Fenton-like process using novel CuO-CeO₂-CoO_x composite nanocatalyst. *Journal of Hazardous Materials* **2019**, *374*, 167-176.
71. Loto, C. A., Electroless Nickel Plating - A Review. *Silicon* **2016**, *8* (2), 177-186.
72. Van Den Meerakker, J. E. A. M., On the mechanism of electroless plating. II. One mechanism for different reductants. *J Appl Electrochem* **1981**, *11* (3), 395-400.
73. Kumaresan, T.; Joshi, J. B., Effect of impeller design on the flow pattern and mixing in stirred tanks. *Chem Eng J* **2006**, *115* (3), 173-193.
74. Ping, Z. X.; He, Y. D.; Gu, C. D.; Zhang, T. Y., Electroless plating of Ni-P coatings on carbon steel in a stirred bed of glass balls. *J Appl Electrochem* **2009**, *39* (6), 879-885.
75. Tenno, R.; Kantola, K. In *Bath and Deposit Monitoring System for Electroless Nickel Plating Process*, Proceedings of the 9th WSEAS International Conference on Automatic Control, Modeling and Simulation, Istanbul, Turkey, May 27-29; WSEAS: Istanbul, Turkey, 2007.
76. Shacham - Diamand, Y. Y., Electroless copper deposition using glyoxylic acid as reducing agent for ultralarge scale integration metallization. *Electrochemical and Solid-State Letters* **2000**, *3* (6), 279-282.

77. Sricharoenchaikit, P.; Calabrese, G. S.; Gulla, M. Controlled electroless plating. U.S. Patent 5,203,911, Apr 20, 1993.
78. Aal, A. A.; Shaaban, A.; Hamid, Z. A., Nanocrystalline soft ferromagnetic Ni–Co–P thin film on Al alloy by low temperature electroless deposition. *Appl Surf Sci* **2008**, *254* (7), 1966-1971.
79. Balaraju, J. N.; Selvi, V. E.; Grips, V. K. W.; Rajam, K. S., Electrochemical studies on electroless ternary and quaternary Ni–P based alloys. *Electrochim Acta* **2006**, *52* (3), 1064-1074.
80. Georgieva, J.; Armyanov, S., Electroless deposition and some properties of Ni–Cu–P and Ni–Sn–P coatings. *J Solid State Electr* **2007**, *11* (7), 869-876.
81. Shashikala, A. R.; Mayanna, S. M.; Sharma, A. K., Studies and characterisation of electroless Ni–Cr–P alloy coating. *Transactions of the IMF* **2013**, *85* (6), 320-324.
82. Fukumuro, N.; Nishiyama, J.; Shigeta, K.; Takagami, H.; Yae, S.; Matsuda, H., Confirmation of hydroxide in electroless cobalt alloy films by GDOES. *Transactions of the IMF* **2013**, *85* (2), 111-112.
83. Nwosu, N. O.; Davidson, A. M.; Hindle, C. S., Effect of Sodium Dodecyl Sulphate on the Composition of Electroless Nickel – Ytria Stabilized Zirconia Coatings. *Advances in Chemical Engineering and Science* **2011**, *01* (03), 118-124.
84. Fayyad, E.; Abdullah, A.; Hassan, M.; Mohamed, A.; Wang, C.; Jarjoura, G.; Farhat, Z., Synthesis, Characterization, and Application of Novel Ni-P-Carbon Nitride Nanocomposites. *Coatings* **2018**, *8* (1).
85. Winowlin Jappes, J. T.; Ramamoorthy, B.; Kesavan Nair, P., Novel approaches on the study of wear performance of electroless Ni–P/diamond composite deposits. *J Mater Process Tech* **2009**, *209* (2), 1004-1010.

86. Alexis, J.; Gaussens, C.; Etcheverry, B.; Bonino, J.-P., Development of nickel–phosphorus coatings containing micro particles of talc phyllosilicates. *Mater Chem Phys* **2013**, *137* (3), 723-733.
87. Balaraju, J. N.; Kalavati; Rajam, K. S., Influence of particle size on the microstructure, hardness and corrosion resistance of electroless Ni–P–Al₂O₃ composite coatings. *Surface and Coatings Technology* **2006**, *200* (12-13), 3933-3941.
88. Mafi, I. R.; Dehghanian, C., Comparison of the coating properties and corrosion rates in electroless Ni–P/PTFE composites prepared by different types of surfactants. *Appl Surf Sci* **2011**, *257* (20), 8653-8658.
89. Huang, Y. S.; Zeng, X. T.; Annergren, I.; Liu, F. M., Development of electroless NiP–PTFE–SiC composite coating. *Surface and Coatings Technology* **2003**, *167* (2), 207-211.
90. Ankita, S.; Singh, A. K., Corrosion and wear resistance study of Ni-P and Ni-P-PTFE nanocomposite coatings. *Central European Journal of Engineering* **2011**, *1* (3), 234-243.
91. Sudagar, J.; Lian, J. S.; Sha, W., Electroless nickel, alloy, composite and nano coatings - A critical review. *J Alloy Compd* **2013**, *571*, 183-204.
92. Mainier, F., Fonseca, M. , Tavares, S. and Pardal, J., Quality of Electroless Ni-P (Nickel-Phosphorus) Coatings Applied in Oil Production Equipment with Salinity. *Journal of Materials Science and Chemical Engineering* **2013**, *1* (6), 1-8.
93. Liao, J. Y.; Yang, J.; Fan, W. J.; Li, Q. C.; Zhang, Q.; Zhao, X. D., Influence of Ni-Sn-P Electroless Plating on Anticorrosion Performance of CF Steel. *Int J Electrochem Sc* **2016**, *11* (2), 899-905.
94. Gu, C. D.; Lian, J. S.; He, J. G.; Jiang, Z. H.; Jiang, Q., High corrosion-resistance nanocrystalline Ni coating on AZ91D magnesium alloy. *Surf Coat Tech* **2006**, *200* (18-19), 5413-5418.

95. Liu, J. A.; Zhu, X. Y.; Sudagar, J.; Gao, F.; Feng, P. B., Preparation and Corrosion Resistance of Electroless Ni-P Coating on Open-Cell Aluminum Foams. *Int J Electrochem Sc* **2012**, 7 (7), 5951-5961.
96. Singh, R., The application of an electrochemical technique to determine the porosity of electroless nickel coatings produced in hypophosphite baths. *Anti-Corros Method M* **2003**, 50 (2), 121-128.
97. Valova, E.; Georgieva, J.; Armyanov, S.; Avramova, I.; Dille, J.; Kubova, O.; Delplancke-Ogletree, M. P., Corrosion behavior of hybrid coatings: Electroless Ni-Cu-P and sputtered TiN. *Surf Coat Tech* **2010**, 204 (16-17), 2775-2781.
98. Olawale Olarewaju Ajibola, A. O. A., Daniel Toyin Oloruntoba, Corrosion of Heat Treated Electroless-Ni Plated Mild Carbon Steels in Dilute H₂SO₄. *International Journal of Materials Science and Applications* **2015**, 4 (5), 333-342.
99. Mimani, T.; Mayanna, S. M., The effect of microstructure on the corrosion behaviour of electroless Ni-P alloys in acidic media. *Surf Coat Tech* **1996**, 79 (1-3), 246-251.
100. Zeller, R. L.; Salvati, L., Effects of Phosphorus on Corrosion-Resistance of Electroless Nickel in 50-Percent Sodium-Hydroxide. *Corrosion* **1994**, 50 (6), 457-467.
101. Ashassi-Sorkhabi, H.; Rafizadeh, S. H., Effect of coating time and heat treatment on structures and corrosion characteristics of electroless Ni-P alloy deposits. *Surf Coat Tech* **2004**, 176 (3), 318-326.
102. Wang, L. L.; Zhao, L. H.; Huang, G. F.; Yuan, X. J.; Zhang, B. W.; Zhang, J. Y., Composition, structure and corrosion characteristics of Ni-Fe-P and Ni-Fe-P-B alloy deposits prepared by electroless plating. *Surf Coat Tech* **2000**, 126 (2-3), 272-278.
103. Ashassi-Sorkhabi, H.; Es'haghi, M., Corrosion resistance enhancement of electroless Ni-P coating by incorporation of ultrasonically dispersed diamond nanoparticles. *Corros Sci* **2013**, 77, 185-193.

104. Cisse, M.; Abouchane, M.; Anik, T.; Himm, K.; Belakhmima, R. A.; Ebn Touhami, M.; Tour, R.; Amiar, A., Corrosion Resistance of Electroless Ni-Cu-P Ternary Alloy Coatings in Acidic and Neutral Corrosive Mediums. *International Journal of Corrosion* **2010**, *2010*, 1-9.
105. Safizadeh, F.; Ghali, E.; Houlachi, G., Electrocatalysis developments for hydrogen evolution reaction in alkaline solutions – A Review. *Int J Hydrogen Energ* **2015**, *40* (1), 256-274.
106. Hutton, L. A.; Vidotti, M.; Patel, A. N.; Newton, M. E.; Unwin, P. R.; Macpherson, J. V., Electrodeposition of Nickel Hydroxide Nanoparticles on Boron-Doped Diamond Electrodes for Oxidative Electrocatalysis. *The Journal of Physical Chemistry C* **2011**, *115* (5), 1649-1658.
107. Liu, S.; Sankar, K. V.; Kundu, A.; Ma, M.; Kwon, J. Y.; Jun, S. C., Honeycomb-Like Interconnected Network of Nickel Phosphide Heteronanoparticles with Superior Electrochemical Performance for Supercapacitors. *ACS Appl Mater Interfaces* **2017**, *9* (26), 21829-21838.
108. Pollet, B. G.; Kocha, S. S.; Staffell, I., Current status of automotive fuel cells for sustainable transport. *Current Opinion in Electrochemistry* **2019**, *16*, 90-95.
109. Cetinkaya, T.; Uysal, M.; Akbulut, H., Electrochemical performance of electroless nickel plated silicon electrodes for Li-ion batteries. *Appl Surf Sci* **2015**, *334*, 94-101.
110. Irkham; Watanabe, T.; Einaga, Y., Hydroxide Ion Oxidation in Aqueous Solutions Using Boron-Doped Diamond Electrodes. *Anal Chem* **2017**, *89* (13), 7139-7144.
111. Miao, Y.; Ouyang, L.; Zhou, S.; Xu, L.; Yang, Z.; Xiao, M.; Ouyang, R., Electrocatalysis and electroanalysis of nickel, its oxides, hydroxides and oxyhydroxides toward small molecules. *Biosens Bioelectron* **2014**, *53*, 428-39.
112. Anantharaj, S.; Karthick, K.; Kundu, S., Evolution of layered double hydroxides (LDH) as high performance water oxidation electrocatalysts: A review with insights on structure, activity and mechanism. *Materials Today Energy* **2017**, *6*, 1-26.

113. Quaino, P.; Juarez, F.; Santos, E.; Schmickler, W., Volcano plots in hydrogen electrocatalysis—uses and abuses. *Beilstein J Nanotech* **2014**, *5* (1), 846-854.
114. Yao, Y.; Hu, S.; Chen, W.; Huang, Z.-Q.; Wei, W.; Yao, T.; Liu, R.; Zang, K.; Wang, X.; Wu, G., Engineering the electronic structure of single atom Ru sites via compressive strain boosts acidic water oxidation electrocatalysis. *Nature Catalysis* **2019**, *2* (4), 304-313.
115. Shan, J.; Ling, T.; Davey, K.; Zheng, Y.; Qiao, S. Z., Transition-Metal-Doped RuIr Bifunctional Nanocrystals for Overall Water Splitting in Acidic Environments. *Adv Mater* **2019**, *31* (17), e1900510.
116. Jiang, H.; Gu, J.; Zheng, X.; Liu, M.; Qiu, X.; Wang, L.; Li, W.; Chen, Z.; Ji, X.; Li, J., Defect-rich and ultrathin N doped carbon nanosheets as advanced trifunctional metal-free electrocatalysts for the ORR, OER and HER. *Energy & Environmental Science* **2019**, *12* (1), 322-333.
117. Hou, Y.; Qiu, M.; Kim, M. G.; Liu, P.; Nam, G.; Zhang, T.; Zhuang, X.; Yang, B.; Cho, J.; Chen, M.; Yuan, C.; Lei, L.; Feng, X., Atomically dispersed nickel-nitrogen-sulfur species anchored on porous carbon nanosheets for efficient water oxidation. *Nat Commun* **2019**, *10* (1), 1392.
118. Okumiya, M.; Tsunekawa, Y.; Saida, T.; Ichino, R., Creation of high strength bonded abrasive wheel with ultrasonic aided composite plating. *Surface and Coatings Technology* **2003**, *169-170*, 112-115.
119. Dong, Y.-h.; He, X.-b.; Ud-Din, R.; Guo, C.-y.; Xu, L.; Huang, Y.-t.; Qu, X.-h., Fabrication and thermal stability of Ni-P coated diamond powder using electroless plating. *International Journal of Minerals, Metallurgy, and Materials* **2011**, *18* (4), 479.
120. Petrova, M.; Noncheva, Z.; Dobрева, E., Electroless deposition of diamond powder dispersed nickel–phosphorus coatings on steel substrate. *Transactions of the IMF* **2013**, *89* (2), 89-94.
121. Wu, H., Wire sawing technology: A state-of-the-art review. *Precis Eng* **2016**, *43*, 1-9.

122. Powell, D. M.; Winkler, M. T.; Choi, H.; Simmons, C. B.; Needleman, D. B.; Buonassisi, T., Crystalline silicon photovoltaics: a cost analysis framework for determining technology pathways to reach baseload electricity costs. *Energy & Environmental Science* **2012**, 5 (3), 5874-5883.
123. Yang, S. M.; Tani, Y.; Zhang, Y.; Murata, J., Development of a Drum-Type Manufacturing Method for Electroplated Diamond Wire Tools. *Key Engineering Materials* **2012**, 523, 515-520.
124. Webster, J.; Tricard, M., Innovations in Abrasive Products for Precision Grinding. *CIRP Annals - Manufacturing Technology* **2004**, 53 (2), 597-617.
125. Semba, T.; Sato, H., Development of Electroformed Diamond Tool with Fine Grains Covered with Metal Oxide Coating. *CIRP Annals - Manufacturing Technology* **2000**, 49 (1), 157-160.
126. Chiba, Y.; Tani, Y.; Enomoto, T.; Sato, H., Development of a High-Speed Manufacturing Method for Electroplated Diamond Wire Tools. *CIRP Annals - Manufacturing Technology* **2003**, 52 (1), 281-284.
127. Son, K. S.; Lee, J. H.; Choi, Y. J.; Jung, U. C.; Chung, W. S., Effect of Intermediate Layer Coated Diamond Particles on Performance of Diamond Tool. *Journal of the Korean institute of surface engineering* **2013**, 46 (5), 216-222.
128. Zunke, I.; Kloss, D.; Heft, A.; Schmidt, J.; Grunler, B., Replacing the wet chemical activation with an atmospheric pressure technique in electroless deposition of Prussian blue. *Surf Coat Tech* **2016**, 289, 186-193.
129. Rau, K.; Singh, R.; Goldberg, E., Nanoindentation and nanoscratch measurements on silicone thin films synthesized by pulsed laser ablation deposition (PLAD). *Materials Research Innovations* **2002**, 5 (3-4), 151-161.
130. Bull, S., Nanoindentation of coatings. *Journal of Physics D: Applied Physics* **2005**, 38 (24), R393.

131. Sui, Y.; Sun, C.; Sun, J.; Pu, B.; Ren, W.; Zhao, W., Stability of an Electrodeposited Nanocrystalline Ni-Based Alloy Coating in Oil and Gas Wells with the Coexistence of H₂S and CO₂. *Materials* **2017**, *10* (6), 632.
132. Abadias, G.; Chason, E.; Keckes, J.; Sebastiani, M.; Thompson, G. B.; Barthel, E.; Doll, G. L.; Murray, C. E.; Stoessel, C. H.; Martinu, L., Stress in thin films and coatings: Current status, challenges, and prospects. *Journal of Vacuum Science & Technology A: Vacuum, Surfaces, and Films* **1996**, *36* (2), 020801.
133. Yamamoto, T.; Nagayama, T.; Nakamura, T., Thermal Expansion and Thermal Stress Behavior of Electroless-Plated Fe–Ni–B Alloy Thin Film for High-Density Packaging. *J Electrochem Soc* **2019**, *166* (1), D3238-D3245.
134. Thornton, J. A.; Hoffman, D. W., Stress-related effects in thin films. *Thin Solid Films* **1989**, *171* (1), 5-31.
135. Evans, A. G.; Hutchinson, J. W., The thermomechanical integrity of thin films and multilayers. *Acta Metallurgica et Materialia* **1995**, *43* (7), 2507-2530.
136. Nix, W. D., Mechanical properties of thin films. *Metallurgical Transactions A* **1989**, *20* (11), 2217.
137. Nix, W. D.; Clemens, B. M., Crystallite coalescence: A mechanism for intrinsic tensile stresses in thin films. *J Mater Res* **1999**, *14* (8), 3467-3473.
138. Freund, L.; Chason, E., Model for stress generated upon contact of neighboring islands on the surface of a substrate. *J Appl Phys* **2001**, *89* (9), 4866-4873.
139. Hoffman, R. W., Stresses in thin films: The relevance of grain boundaries and impurities. *Thin Solid Films* **1976**, *34* (2), 185-190.
140. Rossini, N. S.; Dassisti, M.; Benyounis, K. Y.; Olabi, A. G., Methods of measuring residual stresses in components. *Mater Design* **2012**, *35*, 572-588.

141. Chen, Z.; Xu, X.; Wong, C. C.; Mhaisalkar, S., Effect of plating parameters on the intrinsic stress in electroless nickel plating. *Surface and Coatings Technology* **2003**, *167* (2-3), 170-176.
142. Parker, K., Internal stress measurements of electroless nickel coatings by the rigid strip method. In *Testing of Metallic and Inorganic Coatings*, Harding, W.; Di, B., Eds. ASTM International: West Conshohocken, PA, 1987; pp 111-122.
143. Crotty, D. E.; Micyus, N., Internal Stress of Electroless Nickel Deposits. *Plat Surf Finish* **2008**, *95* (2), 30.
144. Doljack, F. A.; Hoffman, R. W., The origins of stress in thin nickel films. *Thin Solid Films* **1972**, *12* (1), 71-74.
145. Mitchell, D.; Guo, Y.; Sarihan, V., Methodology for studying the impact of intrinsic stress on the reliability of the electroless Ni UBM structure. *IEEE Transactions on Components and Packaging Technologies* **2001**, *24* (4), 667-672.
146. Klokhholm, E., An apparatus for measuring stress in thin films. *Review of Scientific Instruments* **1969**, *40* (8), 1054-1058.
147. Kinoshita, K., Recent developments in the study of mechanical properties of thin films. *Thin Solid Films* **1972**, *12* (1), 17-28.
148. Springer, R.; Hoffman, R., Growth Effects on Stress in Nickel Films. *Journal of Vacuum Science and Technology* **1973**, *10* (1), 238-240.
149. Shemanski, R. M.; Beach, J. G.; Maringer, R. E., Plating Stresses from Electroless Nickel Deposition on Beryllium. *J Electrochem Soc* **1969**, *116* (3), 402-409.
150. Duncan, R., The effect of solution age on corrosion resistance of electroless nickel deposits. *Plat Surf Finish* **1996**, *83* (10), 64-70.

151. Thurlow, K., Electroless nickel plating on aluminium connectors. *Transactions of the IMF* **1989**, 67 (1), 82-86.
152. Chen, C.-J.; Lin, K.-L., Internal stress and adhesion of amorphous Ni–Cu–P alloy on aluminum. *Thin Solid Films* **2000**, 370 (1-2), 106-113.
153. Duncan, R., The metallurgical structure of electroless nickel deposits: effect on coating properties. *Plat Surf Finish* **1996**, 83 (11), 65-69.
154. Song, J. Y.; Yu, J., Residual stress measurements in electroless plated Ni–P films. *Thin Solid Films* **2002**, 415 (1), 167-172.
155. Kinast, J.; Hilpert, E.; Rohloff, R.-R.; Gebhardt, A.; Tünnermann, A., Thermal expansion coefficient analyses of electroless nickel with varying phosphorous concentrations. *Surface and Coatings Technology* **2014**, 259, 500-503.
156. Moelle, C.; Klose, S.; Szücs, F.; Fecht, H. J.; Johnston, C.; Chalker, P. R.; Werner, M., Measurement and calculation of the thermal expansion coefficient of diamond. *Diam Relat Mater* **1997**, 6 (5), 839-842.
157. Fan, C.; Celis, J.-P.; Roos, J., Effect of substrate pretreatment on the porosity in thin nickel electrodeposits. *Surface and Coatings Technology* **1992**, 50 (3), 289-294.
158. Celis, J. P.; Roos, J. R.; Fan, C. L., Porosity of electrolytic nickel-phosphorus coatings. *T I Met Finish* **1991**, 69, 15-19.
159. Zhang, M.; Mu, S.; Guan, Q.; Li, W.; Du, J., A high anticorrosive chromium-free conversion coating prepared with an alkaline conversion bath on electroless Ni–P coating. *Appl Surf Sci* **2015**, 349, 108-115.
160. Yin, X.; Hong, L.; Chen, B. H.; Ko, T. M., Modeling the stability of electroless plating bath—diffusion of nickel colloidal particles from the plating frontier. *J Colloid Interf Sci* **2003**, 262 (1), 89-96.

161. Liu, H.; Guo, R.-X.; Liu, Z., Characteristics of microstructure and performance of laser-treated electroless Ni–P/Ni–W–P duplex coatings. *T Nonferr Metal Soc* **2012**, *22* (12), 3012-3020.
162. Ashassi-Sorkhabi, H.; Rafizadeh, S. H., Effect of coating time and heat treatment on structures and corrosion characteristics of electroless Ni–P alloy deposits. *Surface and Coatings Technology* **2004**, *176* (3), 318-326.
163. Liu, W. L.; Hsieh, S. H.; Tsai, T. K.; Chen, W. J.; Wu, S. S., Temperature and pH dependence of the electroless Ni–P deposition on silicon. *Thin Solid Films* **2006**, *510* (1-2), 102-106.
164. Wei, X.; Roper, D. K., Tin Sensitization for Electroless Plating Review. *J Electrochem Soc* **2014**, *161* (5), D235-D242.
165. Pietsch, P.; Wood, V., X-ray tomography for lithium ion battery research: a practical guide. *Annual Review of Materials Research* **2017**, *47*, 451-479.
166. Beamline 8.3.2 Manual. <http://microct.lbl.gov/manual> (accessed May 20).
167. Kelly, R. G., *Electrochemical Techniques in Corrosion Science and Engineering*. CRC Press: New York, 2003.
168. Agarwala, R. C.; Agarwala, V., Electroless alloy/composite coatings: A review. *Sadhana* **2003**, *28* (3), 475-493.
169. Parkinson, R., Properties and applications of electroless nickel. *Nickel Development Institute, Technical Series No. 10081* **1997**, 5-6.
170. Chen, B. H.; Hong, L.; Ma, Y.; Ko, T. M., Effects of surfactants in an electroless nickel-plating bath on the properties of Ni-P alloy deposits. *Ind Eng Chem Res* **2002**, *41* (11), 2668-2678.
171. Ma, L.; He, X.; Fang, A.; Liang, H., Electrochemical Characterization of a Nickel-Phosphorus Coating on Diamond Grits. *Materials Performance and Characterization* **2018**, *7* (3), 266-280.

172. Uchiyama, H.; Endo, T.; Sone, M., Direct Observation of Nodule Growth on Electroless Ni-P Deposition in Supercritical CO₂ Emulsion. *J Electrochem Soc* **2012**, *159* (2), D114-D118.
173. Hadipour, A.; Monirvaghefi, S. M.; Bahrololoom, M. E., Electroless deposition of graded Ni-P coatings. *Surf Eng* **2015**, *31* (6), 399-405.
174. Zhong, L. L.; Liu, C. C.; Mawla, S. A.; John, J. D. S.; Petrehn, J. L. Nodule-free electroless nip plating. U.S. Patent 6,685,990, 2004.
175. Xi, X.; Miao, H.; Zhang, R.; Cheng, J., Effect of phosphorus content on the properties of Ni-P coated diamond. *Surface and Coatings Technology* **2016**, *297*, 27-33.
176. Ahn, J. G.; Kim, D. J.; Lee, J. R.; Chung, H. S.; Kim, C. O.; Hai, H. T., Improving the adhesion of electroless-nickel coating layer on diamond powder. *Surface and Coatings Technology* **2006**, *201* (6), 3793-3796.
177. Marton, J.; Schlesinger, M., The Nucleation, Growth, and Structure of Thin Ni - P Films. *J Electrochem Soc* **1968**, *115* (1), 16-21.
178. Baldwin, C.; Such, T. E., The Plating Rates and Physical Properties of Electroless Nickel/Phosphorus Alloy Deposits. *Transactions of the IMF* **1968**, *46* (1), 73-80.
179. Schmetterer, C.; Vizdal, J.; Ipsier, H., A new investigation of the system Ni-P. *Intermetallics* **2009**, *17* (10), 826-834.
180. Clark, E.; Yeske, R.; Birnbaum, H., The effect of hydrogen on the surface energy of nickel. *Metallurgical Transactions A* **1980**, *11* (11), 1903-1908.
181. Karthikeyan, S.; Vijayaraghavan, L., Investigation of the surface properties of heat treated electroless Ni-P coating. *Transactions of the IMF* **2016**, *94* (5), 265-273.

182. Krishnan, K. H.; John, S.; Srinivasan, K. N.; Praveen, J.; Ganesan, M.; Kavimani, P. M., An overall aspect of electroless Ni-P depositions—A review article. *Metallurgical and Materials Transactions A* **2006**, *37* (6), 1917-1926.
183. Taheri, R. Evaluation of Electroless Nickel-Phosphorus (EN) Coatings. Ph.D. Thesis, University of Saskatchewan, Saskatoon, 2002.
184. Panagopoulos, C.; Papachristos, V.; Sigalas, C., Tensile behaviour of as deposited and heat-treated electroless Ni-P deposits. *J Mater Sci* **1999**, *34* (11), 2587-2600.

APPENDIX

Python code to generate coating thickness distribution images in Figure V.8.

```
# -*- coding: utf-8 -*-
"""
Created on Sun Jul 14 23:46:37 2019

@author: malian
"""
from PIL import Image
import numpy as np
import os
import matplotlib.pyplot as plt
plt.style.use('classic') # colour from blue to red range
# open and convert images into 3d matrix

foldername = '1t2 10min F1-12/'
for subfolder in os.listdir(foldername):

    mypath=os.path.dirname(foldername+subfolder+'/')

    def load_dataset( ) :
        dimg =[]
        for fname in os.listdir(mypath):
            pathname = os.path.join(mypath, fname)
            im = Image.open(pathname)

            imarr = np.array(im) # Create an array

            dimg.append(imarr)

        return dimg

    dimg= load_dataset()
    dimgarr=np.array(dimg)

    norm = np.ones(dimgarr.shape)
    img=dimgarr-norm*32768

# calculate thickness along h direction for each l layer and w layer

l=img.shape[0] # 2, i, number of images
h=img.shape[1] # 3, j, number of pixels in thickness
w=img.shape[2] # 4, k, number of pixels in width

n=np.zeros((l,w))
t=np.zeros((l,w))
nl=np.zeros((l,w))

print (l,w,h) # picture dimensions

for i in range(l):
```

```

    for k in range(w): # k=0-3 column
        n[i, k]=np.sum(img[l-i-1,:,w-k-1])

        t[i, k]=n[i, k]*0.641 # pixel to um

# calculate coating area if thickness>0 along h direction for each l
layer and w layer
    if n[i,k]>0:
        n1[i,k]=1
    else:
        n1[i,k]=0

area=np.sum(n1[:,:])*0.645**2 #um^2
area=round(area*10)/10
avt=np.sum(n[:,:])/np.sum(n1[:,:])*0.645 #average thickness
avt=round(avt*10)/10
mt=np.max(t) # maximum thickness on the surface
mt=round(mt*10)/10

print (subfolder[10:],'\n', area,'\n', mt,'\n', avt)
print (area,' ','\u03BCm', mt,' ','\u03BCm',)

fig, ax = plt.subplots()

plt.imshow(t,vmin=0,vmax=22.5)

plt.title("Thickness "+subfolder,fontsize=12)

plt.axis('off')

# add a scale bar
from matplotlib_scalebar.scalebar import ScaleBar
#https://pypi.org/project/matplotlib-scalebar/
scalebar = ScaleBar(0.645e-6)
plt.gca().add_artist(scalebar)
plt.show()

fig.savefig(mypath+'.png',dpi=300,bbox_inches="tight")

```